Numerical Investigation of Combustion Noise of Turbulent Flames

Abhishek Lakshman Pillai

Numerical Investigation of Combustion Noise of Turbulent Flames

Abhishek Lakshman Pillai

A thesis submitted to Kyoto University
for the degree of Doctor of Philosophy in Engineering

2018

Acknowledgments

The research described in this thesis was carried out in the Department of Mechanical Engineering and Science at Kyoto University's Graduate School of Engineering, under the supervision of Professor Ryoichi Kurose (Head of the Thermal Science and Engineering Laboratory). The author would like to express his most heartfelt gratitude to Prof. Ryoichi Kurose for all the helpful suggestions, guidance, discussions and constant encouragement during the course of this PhD research.

The author is also very thankful to Prof. Hideo Yoshida and Prof. Kazuyoshi Nakabe for many useful discussions and critical comments which helped to improve this thesis.

The author is also grateful to Prof. Satoru Komori (Former Head of the Environmental Fluids and Thermal Engineering Laboratory) for many valuable and critical comments during the initial stages of this research.

The author is indebted to Prof. Ryoichi Kurose and Prof. Satoru Komori for giving him the opportunity to pursue PhD at the prestigious Kyoto University, Japan.

The author is deeply grateful to Assistant Professor Masaya Muto for many useful discussions, advice, encouragement and help during the course of this PhD program.

The author would also like to thank Dr. Rudra Roy and Dr. Yong Hu from the bottom of his heart for many fruitful discussions and inputs, as well as their help.

The author would also like to express his gratitude to Prof. Nilanjan Chakraborty of Newcastle University, UK for collaborative research, many useful suggestions and comments.

The author expresses his heartfelt gratitude to Dr. Kitano Tomoaki for his help and numerous valuable suggestions.

The author is very thankful to Mr. Kenichiro Takenaka, Mr. Ryo Awane, Mr. Reo Kai, Mr. Akihiro Nakanishi, Mr. Kento Konishi and Mr. Ryohei Ieda for their help and discussions during this research.

The author also expresses his gratitude to the past members of the Environmental Fluids and Thermal Engineering Laboratory.

This research was partially supported by MEXT (Ministry of Education, Culture, Sports, Science and Technology) as "Priority issue on Post-K computer" (Accelerated Development of Innovative Clean Energy Systems), and by MEXT Grant in Aid (No.16H04278). The author is also grateful to MEXT for the financial support provided through the Monbukagakusho Scholarship Program.

Finally, the author would like to express the deepest appreciation to his parents and sister for the infinite support, constant affection and motivation.

Contents

Chapter 1

Introduction

1.1 Background and motivation for this study

In a typical gas turbine engine of an aircraft, the major contributors to engine noise emission are the fan, compressor, combustor, turbine and jet exhaust. Noise from the rotating turbomachinery, i.e. fan, compressor and turbine have been suppressed to the best possible extent, owing to research and development aimed at better designs of blade geometries supplemented by potent acoustic liners. Since the 1960s, considerable amount of research efforts have been invested to study the properties and generation mechanisms of jet noise [1–4]. Then came the turbofan engines with high-bypass ratios, and the more recent ultra-high-bypass ratio turbofan engines. The lower jet-exhaust velocities in such engines drastically attenuated the jet noise. Additionally, improvements in nozzle designs (e.g. Chevron nozzle) lead to further reduction in jet-exhaust noise.

With the reduction in noise emissions from rotating turbomachinery and jet exhaust, combustion noise has emerged as a dominant contributor to engine-core noise and an issue that needs resolution, due to the stringent noise emission norms being imposed by regulatory authorities like the International Civil Aviation Organization (ICAO). To minimize the impact of burning fossil fuels in gas turbine engines on the environment, focus has now shifted towards combustor designs with low-emissions of NOx and greenhouse gases employing advanced combustion technologies, such as lean direct injection

and lean premixed pre-vaporized combustion. However, such lean combustion is known to produce substantially louder noise, because of its inherently unsteady nature [5, 6]. Apart from being a major source of noise pollution which causes adverse effects on health and quality of life upon long-term exposure, combustion noise can also trigger combustion instabilities [7, 8] in the gas turbine combustors, especially the ones using lean combustion strategies. Inside the combustor, pressure perturbations generated by unsteady combustion are reflected at the boundaries of the combustor. Feedback interaction between these reflected pressure waves and the unsteady heat release induces combustion instability inside the combustor, which is characterized by the emission of discrete tones, loud noise and enormous pressure fluctuations. Such strong pressure oscillations can lead to structural damage of engine components [5, 9]. The heat release rate and pressure perturbations occur at a fixed frequency and are coherent during combustion instability, which aggravates the heat flux and thermal stresses at the walls of the combustor. Furthermore, the vibrations induced by the severe pressure oscillations during a combustion instability can cause fatigue cracking of combustor liners [10]. Combustion instability also induces the phenomenon of flashback (transient upstream propagation of a flame usually caused by a combustion instability) in combustors which poses a potential hazard [11–13].

In commercial gas turbine engines as well as auxiliary power units, fuel is introduced inside the combustors in either gaseous form or as liquid spray, which then undergoes subsequent turbulent combustion resulting in heat addition in the combustors. Combustion noise is a by-product of this turbulent combustion and for combustion occurring in confinement, such as combustion inside a gas turbine combustor, the total noise emitted is made up of direct and indirect combustion noise [14]. Direct combustion noise originates from heat release rate fluctuations associated with the interaction between turbulence and chemical reactions [14]. Direct combustion noise is perceived as the unsteady volumetric expansion and contraction of the reacting gas mixture arising from said fluctuations of heat release rate, and is a characteristic feature of open turbulent flames. Indirect combustion noise on the other hand, corresponds to the pressure per-

turbations generated by the acceleration of entropy and vorticity non-uniformities as they get convected through the turbine stages and nozzle beyond the combustor outlet [10, 15–17].

Extensive experimental investigations have been performed for combustion noise generated by open turbulent premixed flames [14, 18–22] and open turbulent non-premixed flames [19, 23–26]. Experimental studies on combustion noise emitted by premixed jet flames revealed that, for a given nozzle diameter and exit velocity, fuel-lean flames are quieter than fuel-rich flames [21, 22]. Also, the combustion noise power of premixed flames increases with turbulence velocity fluctuations, as reported in the findings of Kilham and Kirmani [27]. The increase in acoustic power with turbulent velocity fluctuations was also confirmed by Kotake and Takamoto for lean premixed flames [22]. However, the combustion noise emitted by rich premixed flames is not affected by either burner geometry or turbulence level as reported by Kotake and Takamoto [21, 22].

Price et al. [19] found that, in case of turbulent non-premixed flames that are usually much longer compared to turbulent premixed flames, the effective length of the predominant region of sound generation is less than the total flame length itself. However, some common characteristics can be found in the combustion noise emitted by both premixed [14, 19–22, 27] and non-premixed flames [23, 24, 26, 28, 29], such as: (1) combustion noise has a broadband spectrum with a spectral peak located in the frequency range of about 200-1000 Hz and a peak sound level in the range of 60-80 dB, and (2) increasing the fuel flow rate and the heating value of the fuel will increase the Overall Sound Pressure Level (OASPL).

Numerical techniques have also been used as viable tools for investigation of combustion noise emitted by flames, such as Large-Eddy Simulation (LES), Direct Numerical Simulation (DNS) and the hybrid Computational Fluid Dynamics and Computational Aero-Acoustics (CFD/CAA) framework. For example, Swaminathan et al. [30] and Yu et al. [31] used DNS to investigate the combustion noise generated by turbulent premixed flames. Ihme et al. [29, 32] investigated the direct combustion noise generated by a turbulent non-premixed flame, using a hybrid model combining Large-Eddy Simulation

(LES) for the reactive flow-field and Lighthill's acoustic analogy for the radiated acoustic field. The LES/CAA framework has also been used by Flemming et al. [33] to investigate the noise radiated from turbulent non-premixed flames, by coupling LES with two acoustic methods, viz. the Equivalent Source Method (ESM) and the Boundary Element Method (BEM). In another investigation [28], a hybrid approach combining LES for the reactive flow field with a CAA method employing a wave equation approach (Lighthill's analogy) to solve for the propagation of acoustic waves, was used to study the combustion noise emitted by a turbulent non-premixed flame. There also exist studies using the Random Particle Mesh for Combustion Noise (RPM-CN) method [34, 35], which is a hybrid Reynolds-averaged Navier-Stokes (RANS)/CAA approach for simulation of combustion noise from open turbulent non-premixed flames.

More recently, Bui et al. [36, 37] applied the hybrid LES/APE-RF approach to analyse the combustion generated acoustic field and sound source mechanisms of turbulent non-premixed flames. In this hybrid LES/CAA approach, the acoustic wave propagation is computed by solving the Acoustic Perturbation Equations for Reacting Flows (APE-RF), which is an extension of the original system of Acoustic Perturbation Equations (APE) developed by Ewert and Schröder [38] to multicomponent reacting flows.

It is worth mentioning that, all the above studies focus primarily on the combustion noise phenomena in turbulent premixed and non-premixed flames. There aren't enough numerical or experimental studies in existing scientific literature, that deal with the combustion noise problem in turbulent spray flames/combustion. Spray combustion is an intricate multiphase phenomenon involving the turbulent dispersion of liquid fuel droplets that are convected along with the carrier gas-phase, while undergoing evaporation and subsequent combustion reaction of the evaporated fuel with the oxidizer. The above processes occur simultaneously while influencing one another, and it is this coupling of the various process between different phases that makes the analysis of spray combustion quite complicated.

The method employed for all the numerical investigations carried out in this research is DNS, meaning no turbulence model nor any turbulence-chemistry interaction model

has been used. However, in order to incorporate the combustion reactions into the DNS, simplified reaction mechanisms, such as one- or two-step global reaction models have been employed. The reason for using simplified reaction mechanisms in conjunction with DNS is to achieve realizable computational costs. To perform a three-dimensional DNS of a jet flame with detailed chemistry, the computational cost would be of the order of millions of CPU hours [13], which is not always practical. Furthermore, the use of such simplified chemistry (one- or two-step global reaction mechanisms) for conducting numerical simulations of premixed, non-premixed and spray combustion problems, is not that uncommon and has been used in several studies previously [39–45].

Therefore, in this study the combustion noise characteristics of an open turbulent spray flame have been predicted and investigated using different numerical strategies, namely DNS and hybrid DNS/CAA approach, in addition to investigations of combustion noise in turbulent non-premixed flames. The aim is to attain a better understanding of the combustion noise characteristics in turbulent flames, in order to clarify the underlying mechanism. First, DNS of two open turbulent non-premixed Hydrogen flames are performed to analyze the characteristics of direct combustion noise generated by them. The effect of Reynolds number on the noise emitted from these Hydrogen flames, as well as the mechanism influencing combustion noise generation are also investigated. Second, DNS is used to predict the combustion noise generation from an unconfined turbulent spray flame and the noise radiation behavior is examined. Directivity of noise has been used for the derivations of noise source characteristics. Finally, the relatively new numerical framework of the hybrid CFD/CAA approach is applied to a turbulent spray flame as well as a turbulent non-premixed flame, for simulating their reacting flow-fields along with the respective combustion-induced acoustic fields. The hybrid approach is used for predicting combustion noise of the flames, and the acoustic propagation behavior is investigated.

1.2 Thesis outline

This thesis consists of five chapters.

Chapter 1, the present chapter, describes the background and motivation for the study, and outline of this thesis.

Chapter 2 describes the DNS of combustion noise from open turbulent non-premixed Hydrogen flames. In this study, two turbulent non-premixed Hydrogen jet flames with the same Nitrogen-diluted Hydrogen fuel mixture (H_2/N_2 : 50/50 volume %), and with different Reynolds numbers have been simulated using DNS. A one-step global reaction model is used for describing Hydrogen combustion reaction [46]. The effect of Reynolds number on the direct combustion noise generated by the two turbulent non-premixed Hydrogen flames has been investigated and the mechanism influencing combustion noise behavior due to variation in Reynolds number has been elucidated.

Chapter 3 describes the characteristics of combustion generated noise of an open turbulent spray flame. The investigation of this multiphase reacting flow is performed by means of DNS employing an Eulerian-Lagrangian framework with two-way coupling. The carrier gas-phase's governing equations are solved in an Eulerian framework, while the evaporating liquid fuel droplets are individually tracked in a Lagrangian framework. The fuel used for the spray flame is Ethanol and a two-step global reaction model [47] is used to account for the combustion reaction. The direct combustion noise of this open turbulent spray flame is analyzed in terms of spectral content, directionality and sound pressure levels.

Chapter 4 describes the application of a hybrid CFD/CAA approach to an open turbulent spray flame and an open turbulent non-premixed flame. In this approach, DNS is used to simulate the reacting flow-fields of the flames, while their combustion generated acoustic fields are predicted using CAA simulations in which the Acoustic Perturbation Equations for Reacting Flows (APE-RF) [36, 37] are solved. The source term dominating the excitation of acoustic waves, which is computed from the DNS of the flames' flow-fields is then used as input data for solving the APE-RF. This new numerical framework termed as the hybrid DNS/APE-RF approach, is used to analyze

the characteristics of combustion noise radiated to the far-field.

Chapter 5 summarizes all the investigations carried out in this study and recommendations for possible future extensions of the present research are provided.

References

[1] J. E. Ffowcs Williams. Hydrodynamic noise. *Annu. Rev. Fluid Mech.*, 1:197–222, 1969.

[2] J. E. Ffowcs Williams. Aeroacoustics. *Annu. Rev. Fluid Mech.*, 9:447–468, 1977.

[3] M. E. Goldstein. Aeroacoustics of turbulent shear flows. *Annu. Rev. Fluid Mech.*, 16:263–285, 1984.

[4] C. K. W. Tam. Supersonic jet noise. *Annu. Rev. Fluid Mech.*, 27:17–43, 1995.

[5] A. P. Dowling and S. R. Stow. Acoustic analysis of gas turbine combustors. *J. Propul. Power*, 19:751–764, 2003.

[6] Y. Liu, A. P. Dowling, N. Swaminathan, R. Morvant, M. A. Macquisten, and L. F. Caracciolo. Prediction of combustion noise for an aeroengine combustor. *J. Propul. Power*, 30:114–122, 2013.

[7] S. Candel. Combustion dynamics and control: Progress and challenges. *Proc. Combust. Inst.*, 29:1–28, 2002.

[8] S. Candel, D. Durox, S. Ducruix, A. L. Birbaud, N. Noiray, and T. Schuller. Flame dynamics and combustion noise: Progress and challenges. *Int. J. Aeroacoust.*, 8:1–56, 2009.

[9] T. Lieuwen and V. Yang. Combustion instabilities in gas turbine engines: Operational experience, fundamental mechanisms, and modeling. *Prog. Astronaut. Aeronaut.*, 210, 2005.

[10] A. P. Dowling and Y. Mahmoudi. Combustion noise. *Proc. Combust. Inst.*, 35:65–100, 2015.

[11] C. Eichler, G. Baumgartner, and T. Sattelmayer. Experimental investigation of turbulent boundary layer flashback limits for premixed hydrogen-air flames confined in ducts. *J. Eng. Gas Turbines Power*, 134(1):011502, 2012.

[12] A. Gruber, J. H. Chen, D. Valiev, and C. K. Law. Direct numerical simulation of premixed flame boundary layer flashback in turbulent channel flow. *J. Fluid Mech.*, (709):516–542, 2012.

[13] T. Kitano, T. Tsuji, R. Kurose, and S. Komori. Effect of pressure oscillations on flashback characteristics in a turbulent channel flow. *Energy Fuels*, 29(10):6815–6822, 2015.

[14] W. C. Strahle. Combustion noise. *Prog. Energy Combust. Sci.*, 4:157–176, 1978.

[15] J. E. Ffowcs Williams and M. S. Howe. The generation of sound by density inhomogeneities in low mach number nozzle flows. *J. Fluid Mech.*, 70:605–622, 1975.

[16] F. E. Marble and S. Candel. Acoustic disturbance from gas non-uniformities convected through a nozzle. *J. Sound Vib.*, 55:225–243, 1977.

[17] M. S. Howe. Indirect combustion noise. *J. Fluid Mech.*, 659:267–288, 2010.

[18] T. J. B. Smith and J. K. Kilham. Noise generation by open turbulent flames. *J. Acoust. Soc. Am.*, 35:715–724, 1963.

[19] R. B. Price, I. R. Hurle, and T. M. Sugden. Optical studies of the generation of noise in turbulent flames. *Proc. Combust. Inst.*, 12:1093–1101, 1968.

[20] W. C. Strahle and B. N. Shivashankara. A rational correlation of combustion noise results from open turbulent premixed flames. *Proc. Combust. Inst.*, 15:1379–1385, 1975.

[21] S. Kotake and K. Takamoto. Combustion noise: Effects of the shape and size of burner nozzle. *J. Sound Vib.*, 112:345–354, 1987.

[22] S. Kotake and K. Takamoto. Combustion noise: Effects of velocity turbulence of unburned mixture. *J. Sound Vib.*, 139:9–20, 1990.

[23] N. Ohiwa, K. Tanaka, and S. Yamaguchi. Noise characteristics of turbulent diffusion flames with coherent structure. *Combust. Sci. Tech.*, 90:61–78, 1993.

[24] S. A. Klein and J. B. W. Kok. Sound generation by turbulent non-premixed flames. *Combust. Sci. Tech.*, 149:267–295, 1999.

[25] K. Singh, S. H. Frankel, and J. P. Gore. Effects of combustion on the sound pressure generated by circular jet flows. *AIAA Journal*, 41(2):319–321, 2003.

[26] K. K. Singh, S. H. Frankel, and J. P. Gore. Study of spectral noise emissions from standard turbulent nonpremixed flames. *AIAA Journal*, 42:931–936, 2004.

[27] J. K. Kilham and N. Kirmani. The effect of turbulence on premixed flame noise. *Symp. (Int.) Combust.*, 17(1):327–336, 1979.

[28] F. Flemming, A. Sadiki, and J. Janicka. Investigation of combustion noise using a LES/CAA hybrid approach. *Proc. Combust. Inst.*, 31:3189–3196, 2007.

[29] M. Ihme, H. Pitsch, and D. Bodony. Radiation of noise in turbulent non-premixed flames. *Proc. Combust. Inst.*, 32:1545–1553, 2009.

[30] N. Swaminathan, G. Xu, A. P. Dowling, and R. Balachandran. Heat release rate correlation and combustion noise in premixed flames. *J. Fluid Mech.*, 681:80–115, 2011.

[31] L. Yu, A. P. Dowling, N. Swaminathan, and T. D. Dunstan. Spatial correlation of heat release rate and sound emission from turbulent premixed flames. *Combust. Flame*, 159:2430–2440, 2012.

[32] M. Ihme and H. Pitsch. On the generation of direct combustion noise in turbulent non-premixed flames. *Int. J. Aeroacoust.*, 11:25–78, 2012.

[33] F. Flemming, A. Nauert, A. Sadiki, J. Janicka, H. Brick, R. Piscoya, M. Ochmann, and P. Költzsch. A hybrid approach for the evaluation of the radiated noise from a turbulent non-premixed jet flame based on large eddy simulation and equivalent source and boundary element methods. In *Proc. of the Twelfth International Congress on Sound and Vibration ICSV12*, Lisbon, Portugal, 2005.

[34] B. Mühlbauer, R. Ewert, O. Kornow, and B. Noll. Evaluation of the RPM approach for the simulation of broadband combustion noise. *AIAA Journal*, 48(7):1379–1390, 2010.

[35] B. Mühlbauer, R. Ewert, O. Kornow, and B. Noll. Broadband combustion noise simulation of open non-premixed turbulent jet flames. *Int. J. Aeroacoust.*, 11(1):1–24, 2012.

[36] T. P. Bui, W. Schröder, and M. Meinke. Numerical analysis of the acoustic field of reacting flows via acoustic perturbation equations. *Comput. & Fluids*, 37:1157–1169, 2008.

[37] T. P. Bui, M. Ihme, W. Schröder, and H. Pitsch. Analysis of different sound source formulations to simulate combustion generated noise using a hybrid LES/APE-RF method. *Int. J. Aeroacoustics*, 8:95–124, 2009.

[38] R. Ewert and W. Schröder. Acoustic perturbation equations based on flow decomposition via source filtering. *J. Comput. Physics*, 188:365–398, 2003.

[39] A. P. Wandel, N. Chakraborty, and E. Mastorakos. Direct numerical simulations of turbulent flame expansion in fine sprays. *Proc. Combust. Inst.*, 32:2283–2290, 2009.

[40] S. P. Malkeson and N. Chakraborty. Statistical analysis of scalar dissipation rate transport in turbulent partially premixed flames: A Direct Numerical Simulation study. *Flow Turbul. Combust.*, 86(1):1–44, 2011.

[41] T. P. Dunstan, N. Swaminathan, K. N. C. Bray, and R. S. Cant. Geometrical properties and turbulent flame speed measurements in stationary premixed V-flames using Direct Numerical Simulation. *Flow Turbul. Combust.*, 87(2–3):237–259, 2011.

[42] T. P. Dunstan, N. Swaminathan, and K. N. C. Bray. Influence of flame geometry on turbulent premixed flame propagation: A DNS investigation. *J. Fluid Mech.*, 709:191–222, 2012.

[43] D. H. Wacks, N. Chakraborty, and E. Mastorakos. Statistical analysis of turbulent flame-droplet interaction: A direct numerical simulation study. *Flow Turbul. Combust.*, 96:573–607, 2016.

[44] D. H. Wacks and N. Chakraborty. Flame structure and propagation in turbulent flame-droplet interaction: A Direct Numerical Simulation analysis. *Flow Turbul. Combust.*, 96:1053–1081, 2016.

[45] T. Kitano, K. Kaneko, R. Kurose, and S. Komori. Large-eddy simulations of gas– and liquid–fueled combustion instabilities in back-step flows. *Combust. Flame*, 170:63–78, 2016.

[46] N. M. Marinov, C. K. Westbrook, and W. J. Pitz. Detailed and global chemical kinetics model for hydrogen. San Francisco, CA, 1995. 8^{th} International Symposium on Transport Properties.

[47] C. K. Westbrook and F. L. Dryer. Simplified reaction mechanisms for the oxidation of hydrocarbon fuels in flames. *Combust. Sci. Tech.*, 27:31–43, 1981.

Chapter 2

DNS of combustion noise from open turbulent non-premixed hydrogen flames

2.1 Introduction

In this chapter, noise generated by two open turbulent non-premixed Hydrogen jet flames is investigated using Direct Numerical Simulation (DNS) and the effect of Reynolds number Re on the combustion noise characteristics of both flames is also studied. Both jet flames have the same Nitrogen-diluted Hydrogen fuel mixture (H_2/N_2 : 50/50), but different jet exit velocities which represent changes in their Reynolds number. There are several experimental studies on the noise generation by turbulent premixed flames [1–7], but those on the noise generation by turbulent non-premixed flames are limited. For example, Ohiwa et al. [8] investigated the relationship between flame structure and noise characteristics for co-flow non-premixed turbulent flames in their experiments. Singh et al. [9] measured the Sound Pressure Level (SPL) data for two turbulent non-premixed flames (TNF) designated as DLR-A and DLR-B , which are the standard flames investigated extensively in experiments conducted at the workshop for turbulent non-premixed flames (TNF-workshop) [10]. They compared the noise generated by the turbulent

non-premixed flames with those produced by non-reacting air jets with identical exit Reynolds numbers, and found that the noise generated by the turbulent non-premixed flames were several orders of magnitude louder than that of the corresponding non-reacting air jets with identical exit Re. They also concluded that the combustion noise sources in the turbulent non-premixed flames are distributed over a wider spatial region compared to the turbulence noise sources in the corresponding non-reacting air jets.

Later, Singh et al. [11] conducted experiments of the same two standard turbulent non-premixed flames (DLR-A and DLR-B) and investigated their spectral noise emissions, while also comparing the sound pressure level spectra of these flames with those of corresponding air jets with identical Re. In their findings, they reported that the sound pressure spectra of the noise generated by the turbulent non-premixed flames have a predominantly low frequency characteristic, where the spectral peaks have nearly constant SPL in the frequency range of 400-2000 Hz, implying that most of the acoustic energy produced by the turbulent non-premixed flames is contained in the low-frequencies. These characteristics were found to be completely different from those of non-reacting air jets. Furthermore, the measured noise spectra of the DLR-A and DLR-B flames were found to be qualitatively similar even though they have different Reynolds numbers. However, the amplitude of sound pressure levels were found to differ with variation in exit Reynolds number. Moreover, for a given Re the sound pressure spectra of the turbulent non-premixed flames exhibited higher amplitudes compared to those of corresponding air jets at all frequencies.

Numerical approaches such as Direct Numerical Simulations (DNS), Large Eddy Simulations (LES), and the hybrid Computational Fluid Dynamics and Computational Aero-Acoustics CFD/CAA approaches can be effectively employed for predicting the combustion noise in turbulent non-premixed flames. For example, Flemming et al. [12], and Ihme et al. [13, 14] investigated the combustion noise generation in open non-premixed turbulent flames using the hybrid LES/CAA approach. There also exist studies using the Random Particle Mesh for Combustion Noise (RPM-CN) method [15, 16], which is a hybrid Reynolds-averaged Navier-Stokes (RANS)/CAA approach for simu-

lation of combustion noise from open turbulent non-premixed flames. However, to the best of the author's knowledge there are no numerical studies that employ DNS for the prediction of combustion noise generated by turbulent non-premixed flames.

It is well known that for low Mach number turbulent combustion, the noise produced by the fluctuations in heat release rate (known as direct combustion noise) is the dominant noise source [4, 17] and the influence of turbulent noise sources is inconsequential. The phenomenon of combustion noise from open turbulent non-premixed flames is still not clearly understood, let alone the process of noise generation from confined flames which is even more sophisticated. Furthermore, the effect of Reynolds number on the direct combustion noise from turbulent non-premixed flames and its underlying mechanism has not been investigated in detail in previous experimental or numerical investigations.

The purpose of this chapter is therefore, to investigate the effect of Reynolds number on the noise generated by two open turbulent non-premixed Hydrogen flames using DNS, and to elucidate the mechanism influencing the combustion noise behavior of these two flames which have different Reynolds numbers.

2.2 Numerical Methods

2.2.1 Governing Equations

The governing equations for the conservation of mass, momentum, energy, and mass fraction of chemical species are as follows,

$$\frac{\partial \rho}{\partial t} + \nabla \cdot (\rho \boldsymbol{u}) = 0, \tag{2.1}$$

$$\frac{\partial \rho \boldsymbol{u}}{\partial t} + \nabla \cdot (\rho \boldsymbol{u}\boldsymbol{u}) = -\nabla P + \nabla \cdot \boldsymbol{\tau}, \tag{2.2}$$

$$\frac{\partial \rho h}{\partial t} + \nabla \cdot (\rho h \boldsymbol{u}) = \frac{\partial P}{\partial t} + \boldsymbol{u} \cdot \nabla P + \nabla \cdot (\rho D_h \nabla h) + \boldsymbol{\tau} : \nabla \boldsymbol{u}, \tag{2.3}$$

$$\frac{\partial \rho Y_k}{\partial t} + \nabla \cdot (\rho Y_k \boldsymbol{u}) = \nabla \cdot (\rho D_k \nabla Y_k) + S_{comb,k}. \tag{2.4}$$

along with the equation of state for ideal gas. Here ρ is the density, $\boldsymbol{u}$ the velocity, P the pressure, $\boldsymbol{\tau}$ the viscous stress tensor, h the enthalpy, $S_{comb,k}$ is the reaction source term to account for the combustion reaction of Hydrogen, and D_h the thermal diffusivity given as $\rho D_h = \lambda/c_p$, respectively. Here λ and c_p are the heat conductivity and the specific heat capacity, respectively. Y_k and D_k are the mass fraction and the mass diffusion coefficient of species k, which is given under the unity Lewis number assumption as $\rho D_k = \lambda/c_p$, respectively.

2.2.1.1 Reaction model

The term $S_{comb,k}$, appearing on the right hand side of Eq. (2.4) represents the reaction source term for the k^{th} chemical species. For the non-premixed Hydrogen flames, the combustion reaction of Hydrogen is described using a one-step global reaction model [18] as shown below.

$$\mathrm{H_2} + \frac{1}{2}\mathrm{O_2} \overset{k_{global}}{\rightarrow} \mathrm{H_2O}. \tag{2.5}$$

And, $S_{comb,k}$ is evaluated as

$$S_{comb,k} = -\frac{n_k}{n_F} W_k k_{global}. \tag{2.6}$$

Here, n_k and n_F are the molar stoichiometric coefficients of the k^{th} species and fuel, respectively, and W_k is the molecular weight of the k^{th} species. k_{global} is the reaction rate of the one-step global reaction expressed by an Arrhenius formation as follows.

$$k_{global} = 1.8 \times 10^{13} \exp\left(\frac{-17614}{T}\right) [\mathrm{H_2}]^{1.0} [\mathrm{O_2}]^{0.5}. \tag{2.7}$$

Here [-] represents the molar concentration (moles/m^3) of the chemical species. The species considered in this one-step global reaction mechanism are H_2, O_2, H_2O and N_2. Values of all the thermodynamic properties and transport coefficients (taking temperature dependence into account) are obtained from CHEMKIN [19, 20].

2.2.2 Computational Setup

Both turbulent non-premixed open Hydrogen flames simulated in this study were experimentally investigated at the Technische Universität Darmstadt and are also detailed in the database of the workshop for turbulent non-premixed flames (TNF-workshop) [10]. The parameters of the Hydrogen jet flames designated as H5 flame [21] and H3 flame [22] are summarized in Table 2.1. The exit Mach number of the flames presented in Table 2.1 is based on the speed of sound in ambient air C_∞. The burner configuration for the turbulent non-premixed jet flames consists of a circular nozzle of diameter D through which a mixture of Hydrogen and Nitrogen issues out into a low velocity laminar coflow of dry air. The H_2/N_2 volumetric ratio is same for both flames, but the fuel bulk exit velocities are different, and hence, they have different Reynolds numbers. The DNS for each flame is performed on a staggered Cartesian grid consisting of $1080\times400\times400$ grid points (a total of 172.8 million points) in the $x-$, $y-$ and $z-$directions, respectively. The minimum grid spacing used is $\Delta x = \Delta y = \Delta z = 80\mu$m . The domain size is the same for both flames and is approximately $106D \times 59D \times 59D$ in the $x-$, $y-$ and $z-$directions, respectively. Fig. 2.1 represents the cell distributions in the x-y and y-z planes of the 3-D Cartesian grid used for the DNS of both flames. The simulations were carried out on a CRAY XE6 supercomputer at the Academic Centre for Computing and Media Studies (ACCMS), Kyoto University. The DNS of each turbulent non-premixed flame required roughly 400 hours of real time using 1024 cores, which corresponds to a CPU time of 410000 hours.

2.2.3 Numerical Procedure

The in-house thermal flow analysis code FK^3 [23–29] whose algorithm consists of a fractional-step method, which employs a pressure-based semi-implicit algorithm for compressible flows [30] is used for the DNS. The spatial derivatives of the convective terms in the momentum equation are approximated using a 6^{th} order accurate central difference scheme, while the convective terms in the governing equations of the scalar quantities are

Table 2.1: Flow parameters of turbulent non-premixed flames H5 and H3 at nozzle exit.

Flame designation	H5	H3
Fuel (Vol %)	H_2/N_2 : 50/50	H_2/N_2 : 50/50
Jet diameter, D [mm]	8	8
Bulk jet exit velocity, U_{jet} [m/s]	21.7	34.8
Velocity co-flow stream [m/s]	0.2	0.2
Jet Reynolds number, Re [–]	6200	10000
Eckert number, Ec [–]	6.4×10^{-4}	9.6×10^{-4}
Jet Mach number, M $= U_{jet}/C_\infty$ [–]	0.063	0.1
Ambient temperature [K]	300	300

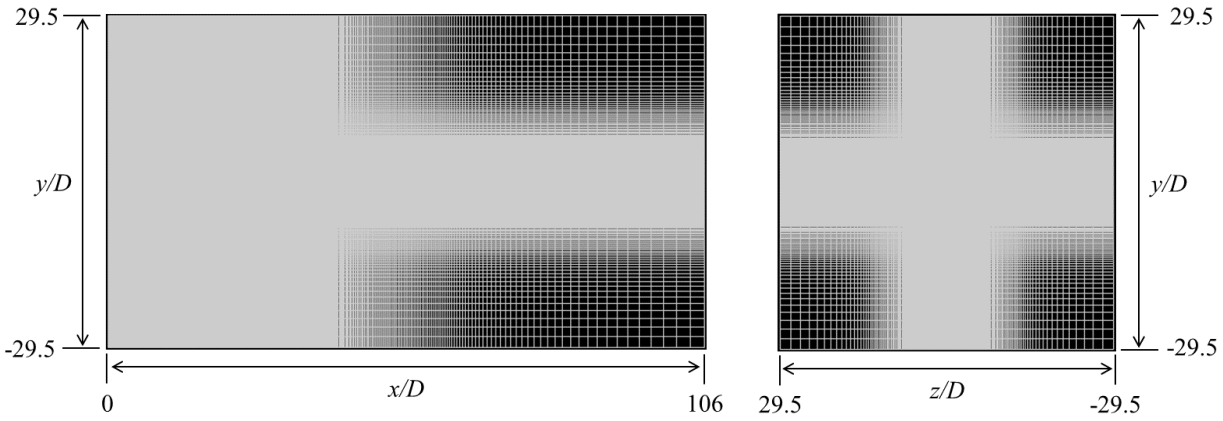

Figure 2.1: Cell distributions in the x-y and y-z planes of the Cartesian grid used for DNS ($D = 8$ mm).

evaluated using the Weighted Essentially Non-Oscillatory (WENO) scheme [31]. The spatial derivatives of the stress tensor terms are evaluated using a 4^{th} order central difference scheme and those of the diffusive terms are discretized by a 2^{nd} order central difference scheme. The time integration of the convective terms is performed using a 3^{rd} order explicit TVD Runge-Kutta method. For the velocity inflow condition, transient turbulent fluctuations generated using a digital filter based technique [32, 33] are superimposed on a fully developed turbulent pipe flow velocity profile at the nozzle exit.

Outside the nozzle region in the inflow plane, the radial and azimuthal velocities are set to zero, the axial coflow velocity of 0.2 m/s is imposed, and Neumann condition is applied for other quantities. At the outflow and lateral boundaries, the Neumann condition is imposed for all quantities. To minimize the amplitude of spurious waves reflected at the boundaries of the computational domain, a sponge zone combining grid stretching and Laplacian filtering [34] is used in the outflow direction (to dissipate the flow fluctuations before they reach the outflow boundary), while absorbing layers consisting of grid stretching and damping terms (artificial dissipation through filtering) are implemented for the lateral boundaries of the computational domain.

2.3 Results and Discussion

2.3.1 Flow-Field Results

The instantaneous temperature distributions presented in Fig. 2.2 show the predicted flame structures of both turbulent non-premixed jet flames. The effect of Reynolds number on the flame structures is evident as the higher Reynolds number H3 flame exhibits a slightly wider spreading compared to the lower Re H5 flame. To validate the DNS, comparison of the computed velocity and temperature statistics with measurements are performed. Fig. 2.3 presents the radial profiles of mean and standard deviation of axial velocity for the H3 flame at various stream-wise locations ($x/D = 5$, 20 and 40). Similar radial statistics of temperature are shown for the H3 flame at the same stream-wise locations in Fig. 2.4. It should be noted that, in these figures any quantity expressed

within triangular parentheses "<>" indicates the time averaging of that quantity. The DNS results show good agreement with the experimental findings for both velocity and temperature statistics. The H3 flame's spreading is accurately captured as is evident from the radial distributions of axial velocity and temperature in Figs. 2.3 and 2.4, respectively. The predicted temperature profiles of the H3 flame are reproduced well and show an overall good agreement with measurements. Axial distributions of the first and second order statistics of axial velocity and temperature are also presented in Fig. 2.5 for the H3 flame, and comparison of the DNS results with measurements yields acceptable agreement.

Additionally, the mean and standard deviation of temperature in the radial direction are presented for the H5 flame in Fig. 2.6 at different stream-wise locations ($x/D = 5$, 20 and 40). The overall agreement between DNS results and experimental data is good. However, minor discrepancies in the predicted temperature statistics can be discerned for both flames. For example, in case of the H3 and H5 flames, the peak mean temperature at $x/D = 5$ is under-predicted (Figs. 2.4 and 2.6), while for the H5 flame, there are small discrepancies in the predicted temperature fluctuations (Fig. 2.6). Such discrepancies could be attributed to the limitations of the one-step global reaction model used for describing Hydrogen combustion.

Another reason for such discrepancies is the lack of adequate information on the inflow boundary conditions in case of both jet flames, such as the radial profiles of mean velocity, corresponding profiles for RMS fluctuations of velocity and the turbulent length scales. In the DNS of both turbulent non-premixed flames, it is assumed that the radial profiles of mean axial velocity at the nozzle exit represent fully developed turbulent pipe flow behavior, i.e. these velocity profiles are evaluated using the power law velocity profile as expressed in Eq. (2.8) below.

$$U(r) = U_c \left(1 - \frac{r}{R}\right)^{\frac{1}{7}}. \tag{2.8}$$

Here, r is the radial distance from the center of the nozzle, $U(r)$ is the mean axial velocity at a radial distance r from the nozzle center, R is the radius of the nozzle and U_c is the centerline velocity of the jet flame.

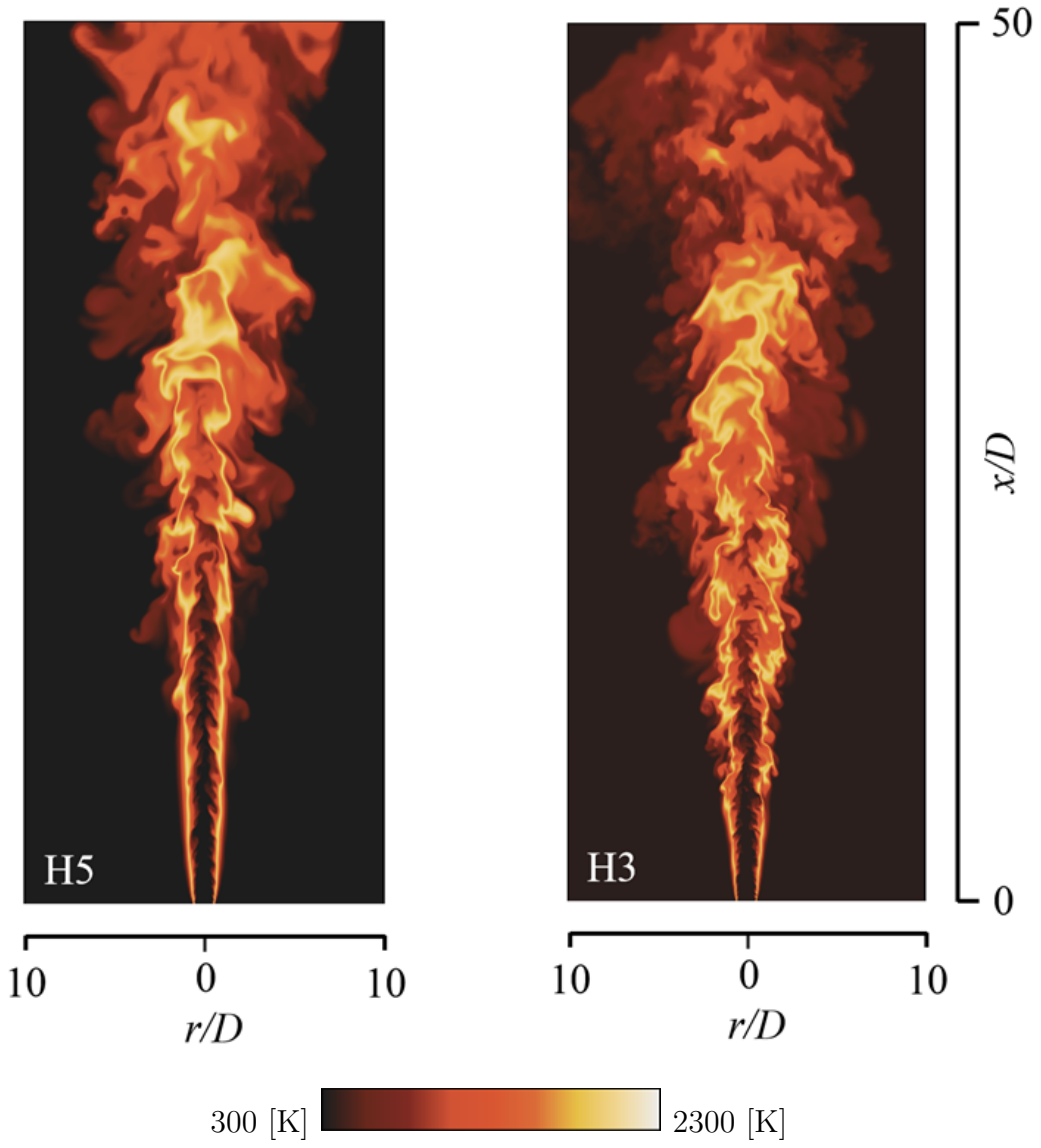

Figure 2.2: Instantaneous snapshots of the DNS predicted temperature fields of H5 flame (left, $Re = 6200$) and H3 flame (right, $Re = 10000$).

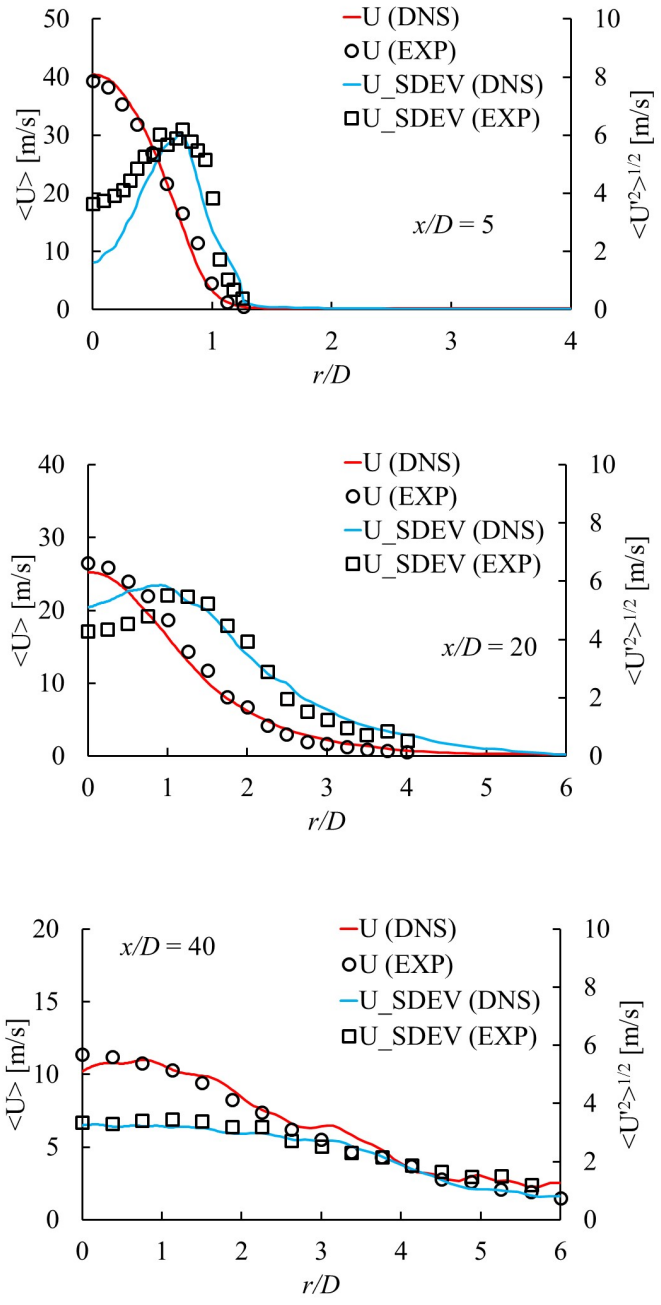

Figure 2.3: Radial profiles of mean axial velocity and its standard deviation (U_SDEV) at stream-wise locations of $x/D = 5$, 20 and 40 for the H3 flame compared with measurements [22].

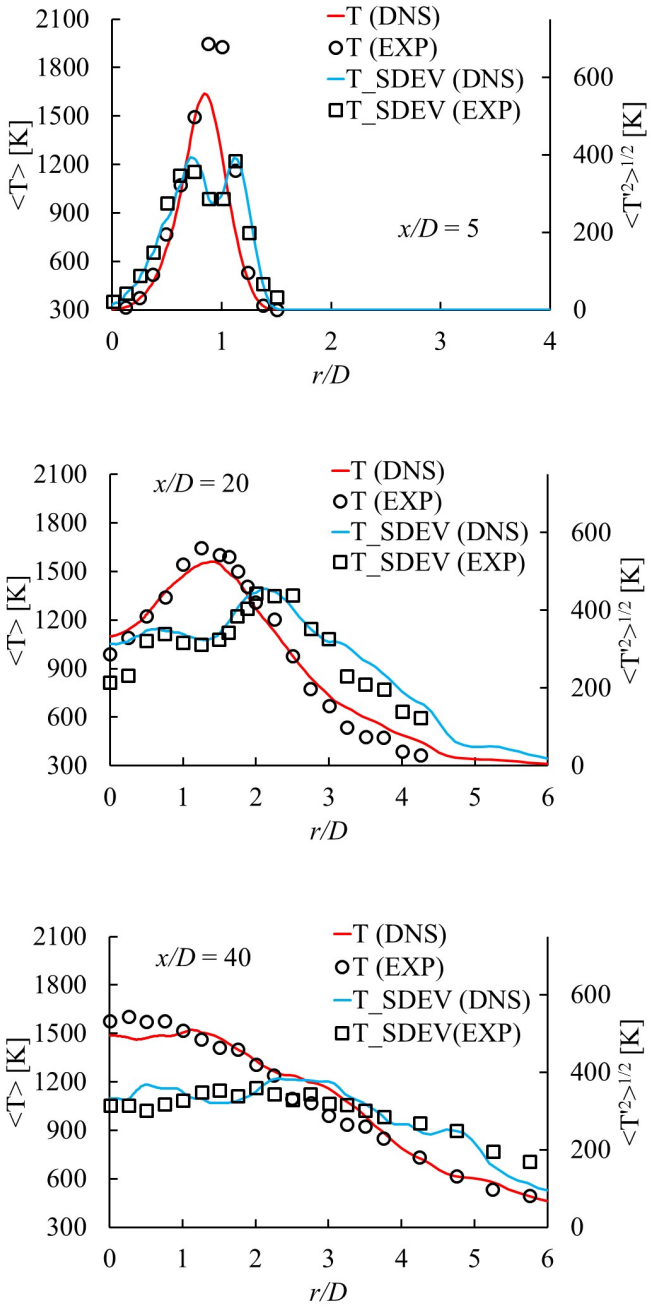

Figure 2.4: Radial profiles of mean and standard deviation of temperature (T_SDEV) at stream-wise locations of $x/D = 5$, 20 and 40 for the H3 flame compared with measurements [22].

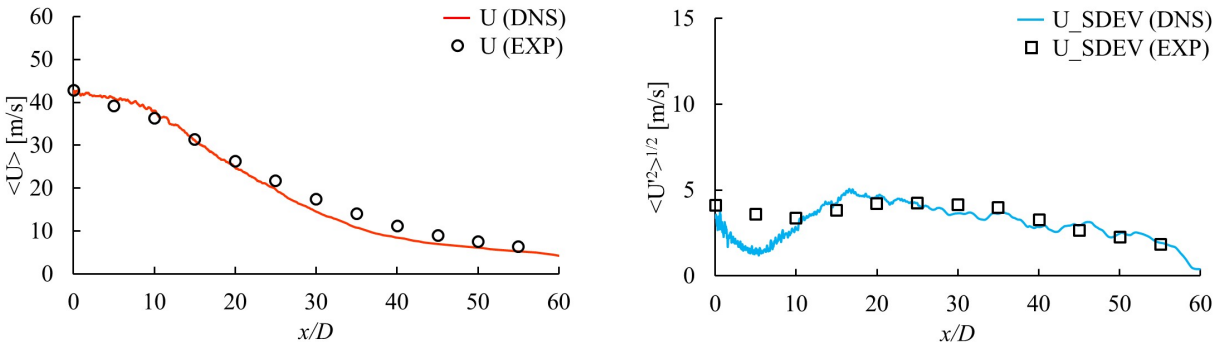

(a) Axial velocity statistics

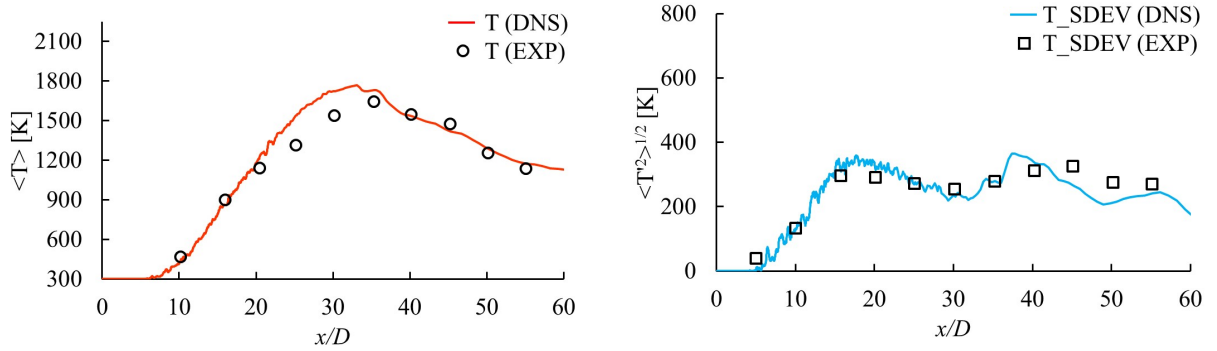

(b) Temperature statistics

Figure 2.5: Axial distributions of (a) mean and standard deviation of axial velocity, and (b) mean and standard deviation of temperature, along the axis of H3 flame compared with measurements [22].

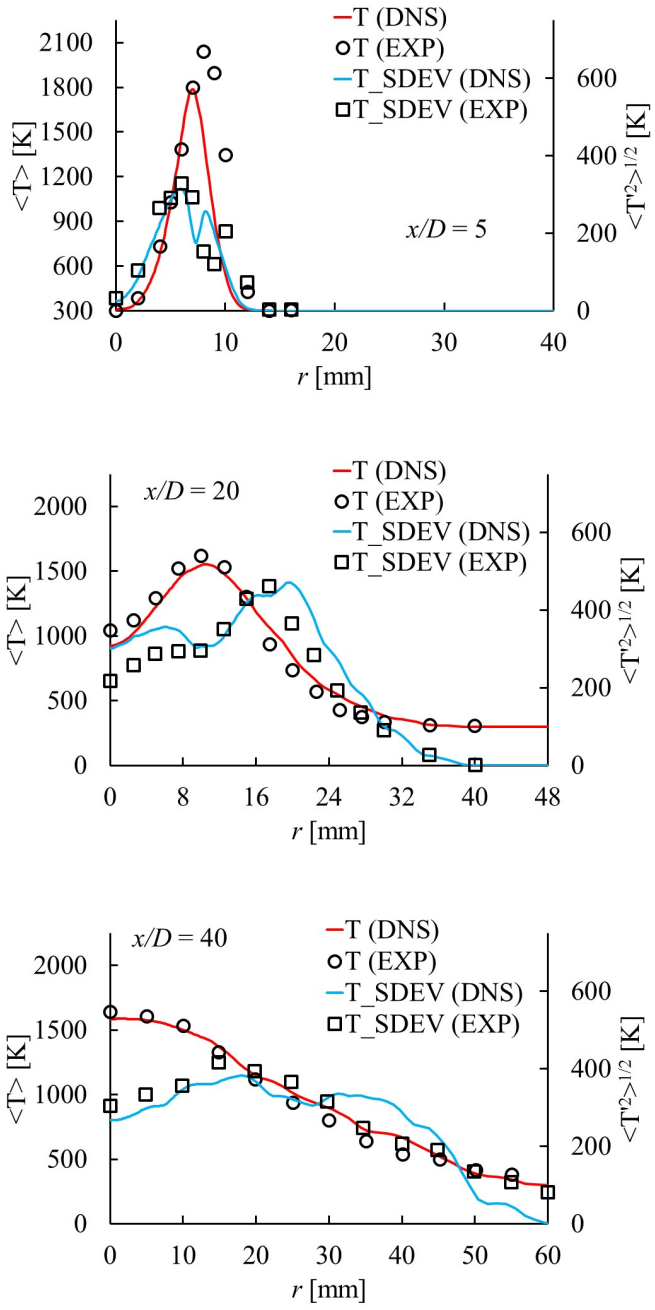

Figure 2.6: Radial profiles of mean and standard deviation of temperature (T_SDEV) at stream-wise locations of $x/D = 5$, 20 and 40 for the H5 flame compared with measurements [21].

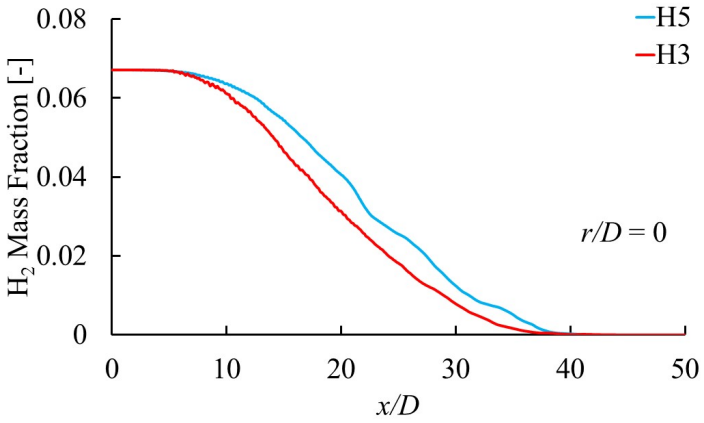

(a)

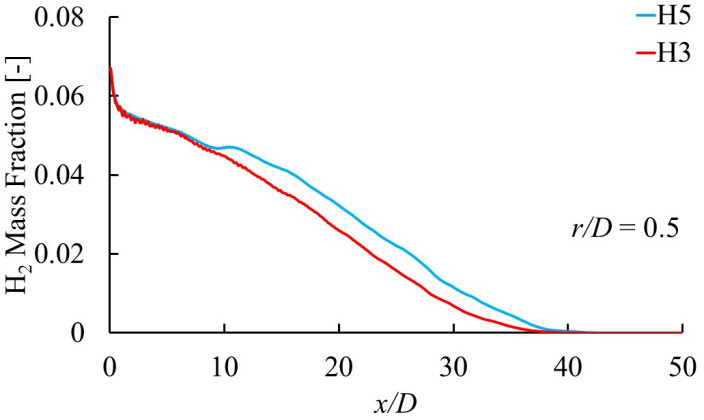

(b)

Figure 2.7: Stream-wise distributions of mean mass fraction of Hydrogen for the H5 and H3 flames (a) along axes of the flames $r/D = 0$, and (b) along the nozzle lip-line $r/D = 0.5$

While, the data on RMS velocity fluctuations and turbulent length scales at the inflow, that are required as inputs for the synthetic turbulence generation algorithm [32, 33] are appropriately adjusted based on known nozzle exit parameters of both flames, so that the DNS results for first and second order flow-field statistics of velocity and temperature give the best possible conformity to the experimental data. However, the flame widths in terms of the radial distributions of mean temperature and the temperature fluctuation trends are well captured for both flames.

In Fig. 2.7, the stream-wise distributions of the mean mass fraction of Hydrogen are shown for both flames along the axes of the flames, and along the nozzle lip-line (i.e. in the mixing layer through which coflow air gets entrained into the jet flame and reaction zones are formed). It is clearly evident that the fuel consumption rate is faster in the higher Re H3 flame compared to the lower Re H5 flame, along the flame axes as well as the nozzle lip-line. As will be shown later in Section 2.3.3, the turbulent velocity fluctuations are larger in the H3 flame compared to the H5 flame at all stream-wise locations, owing to the higher Re of the H3 flame. This leads to better mixing/entrainment of the coflow air into the jet of the H3 flame in comparison to that of the H5 flame. Therefore, in Fig. 2.7 the Hydrogen mass fraction decays at a faster rate along the stream-wise direction (at both $r/D = 0$ and $r/D = 0.5$) for the H3 flame compared to the H5 flame. Moreover, around the stream-wise location of $x/D = 40$, all the Hydrogen has been consumed in the combustion reaction in both flames.

2.3.2 Combustion Noise Results

Analyses of the noise generated by the two turbulent non-premixed jet flames are now presented. First, the sound intensity level spectra of the H3 flame calculated from DNS are compared with the experimental measurements [35] for validation, as shown in Fig. 2.8. For this purpose, different positions namely, $(x/D; r/D) = (18; 63)$, $(x/D; r/D) = (43; 63)$ and $(x/D; r/D) = (68; 63)$ at which microphones were used in the H3 flame's experimental setup [35] to measure the sound intensity spectra, are considered. The computed sound intensities are scaled to the corresponding positions using appropriate

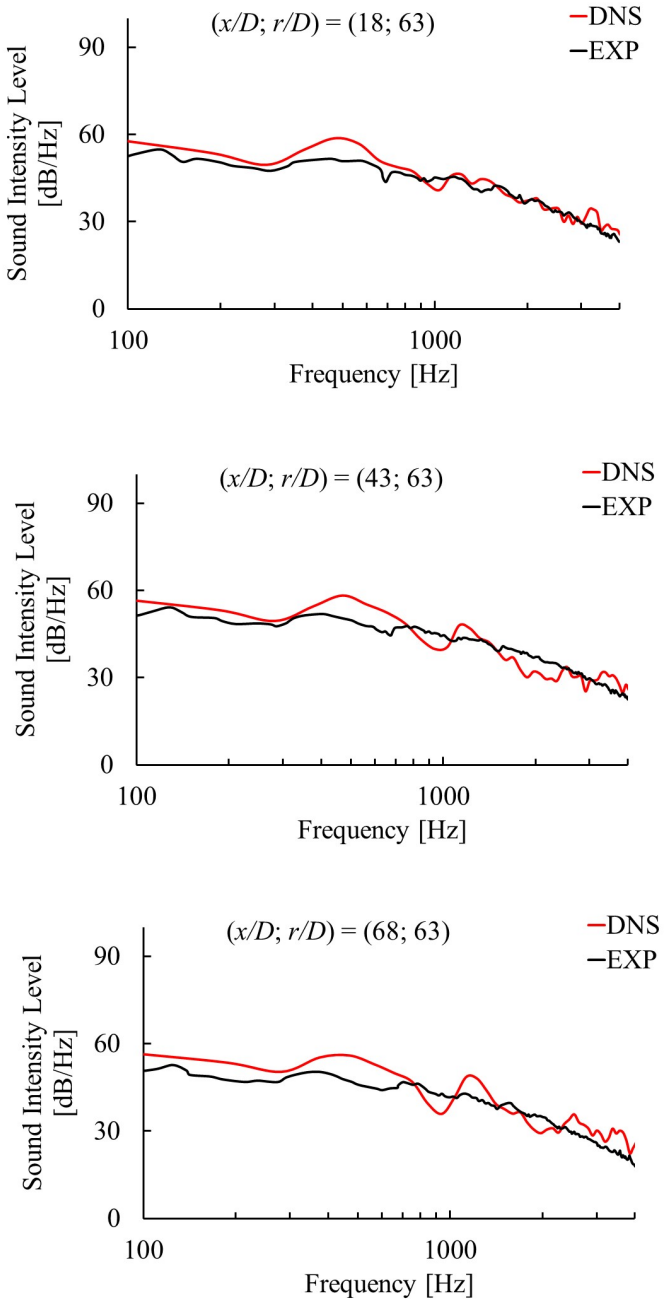

Figure 2.8: Comparison of sound intensity level spectra computed from DNS with experimental measurements [35] for the H3 flame.

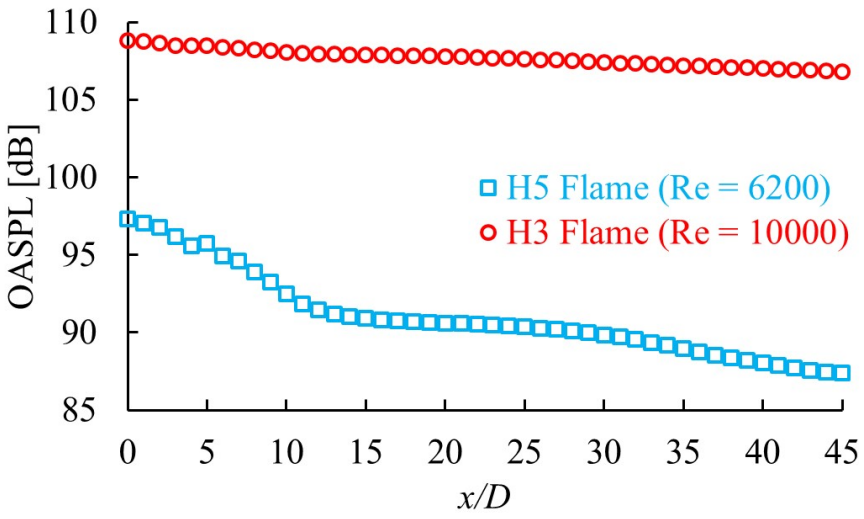

Figure 2.9: Axial distributions of Overall Sound Pressure Level (OASPL) computed at a fixed radial distance $r/D = 10$ from the flame axis.

scaling law [12] and compared with the experimental sound intensity spectra. The computed spectral shapes and sound intensities show overall good agreement with the measured spectra in the frequency range considered. Minor discrepancies at the low frequencies lie in the range 5-10 dB between the computed sound intensity levels and measurements.

The axial distributions of the Overall Sound Pressure Level (OASPL) computed at a fixed radial distance of $r/D = 10$ from the flame axis and at various axial locations from the nozzle exit, are presented in Fig. 2.9 for the two flames. For each flame, the highest OASPL is observed near the nozzle exit and the H3 flame ($Re = 10000$) generates higher sound pressure levels compared to the H5 flame ($Re = 6200$). At the nozzle exit, the H3 flame is 11 dB louder than the H5 flame and the difference in the OASPL of the two flames increases in the downstream direction. Moreover, the axial distribution of OASPL for each flame shows that at a distance of $r/D = 10$ from the flame axis, the OASPL drops by about 2 dB for the H3 flame and 9 dB for the H5 flame from the nozzle exit to $x/D = 40$, indicating a steeper OASPL decay rate for the lower Re H5 flame. The turbulent non-premixed flames investigated in this work belong to the low

Mach number regime as indicated in Table 2.1. Two types of noise sources exist in such turbulent flames, which are due to the heat release rate fluctuations (associated with chemical reaction) and the velocity perturbations. Their corresponding source terms appear on the RHS of a wave equation for low Mach number reacting flows formulated by Kotake [36] as follows.

$$\nabla \cdot \left(\frac{{C_\infty}^2}{\gamma} \nabla \ln(P) \right) - \frac{D}{Dt} \left(\frac{1}{\gamma} \frac{D}{Dt} \ln(P) \right) = - \frac{D}{Dt} \left(\frac{1}{\rho c_p T} \dot{\omega}_T \right) - \nabla \boldsymbol{u} : \nabla \boldsymbol{u}. \tag{2.9}$$

Here, γ is the ratio of specific heat capacities of the reacting gas mixture, T is the gas temperature, and $\dot{\omega}_T$ is the heat release rate due to combustion. The first term on the RHS of Eq. (2.9) is the combustion noise source term S_H arising from the heat release rate fluctuations and the second term is responsible for the turbulent flow noise denoted by S_V. These two source terms are expressed as follows.

$$S_H = - \frac{D}{Dt} \left(\frac{1}{\rho c_p T} \dot{\omega}_T \right) \text{ and } S_V = - \nabla \boldsymbol{u} : \nabla \boldsymbol{u}. \tag{2.10}$$

The instantaneous distributions of S_H and S_V are depicted in Fig. 2.10 and Fig. 2.11, respectively for both H3 and H5 flames. The combustion noise sources S_H are localized within the flames' reaction zones in contrast to the turbulence noise sources S_V which are distributed in the turbulent shear layer and the region beyond the potential core of the flames. The turbulence noise sources S_V decay rapidly with increasing distance from the nozzle exit in the downstream direction and this effect is more pronounced for the lower Re H5 flame. On the other hand, the combustion noise sources S_H extend further in the downstream direction than the turbulent flow noise sources in both flames. Comparing the magnitudes of S_H and S_V in Figs. 2.10 and 2.11, respectively, shows that S_H is an order of magnitude smaller than S_V in both flames. However, the surface density (which represents the ratio of the surface area in which the sources are confined to the volume in which this surface is contained) of the combustion noise sources S_H is higher than that of the turbulence noise sources S_V, which results in an extended acoustic source region for S_H [14].

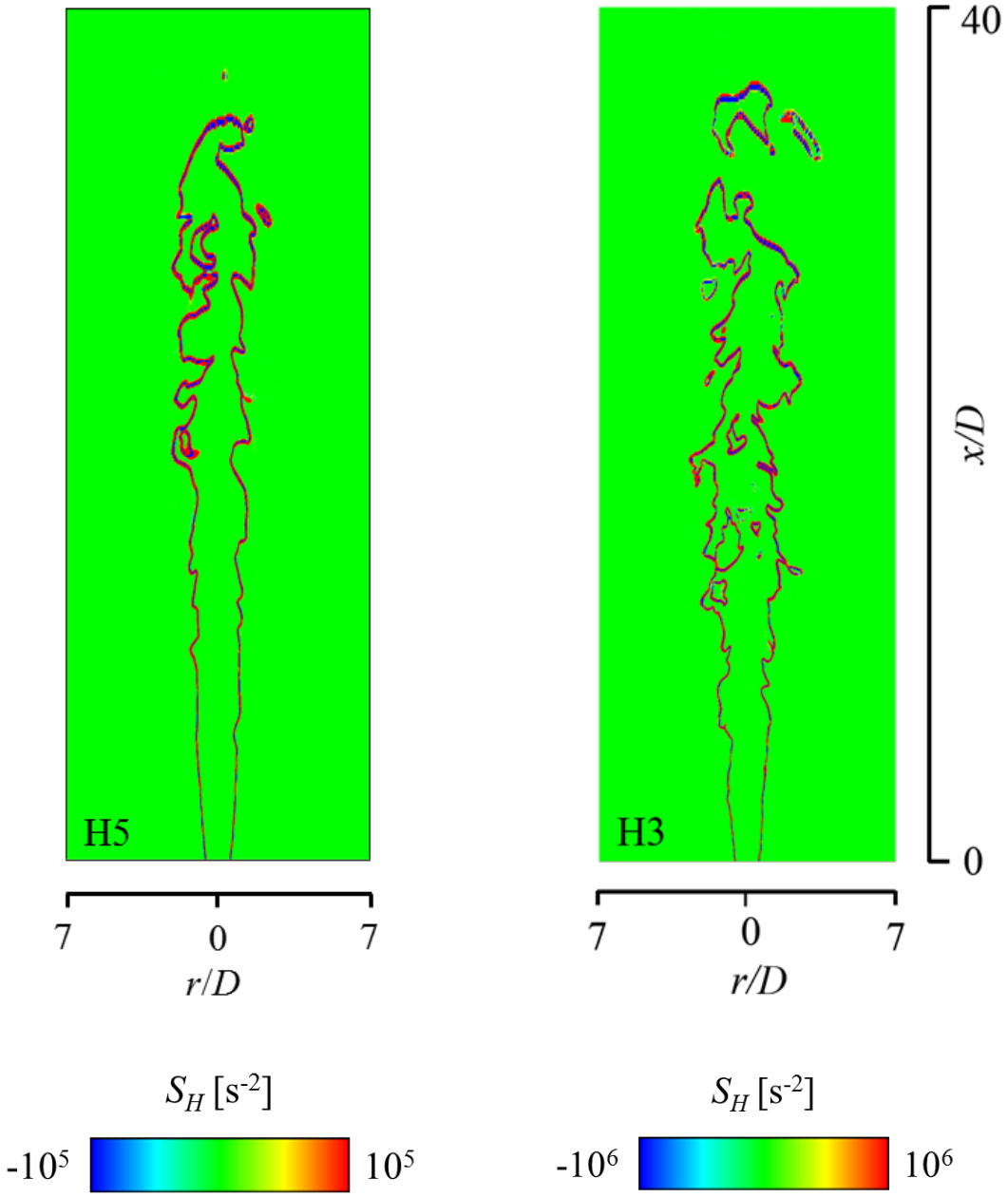

Figure 2.10: Instantaneous distributions of the combustion noise sources S_H in the H5 flame (left, $Re = 6200$) and the H3 flame (right, $Re = 10000$).

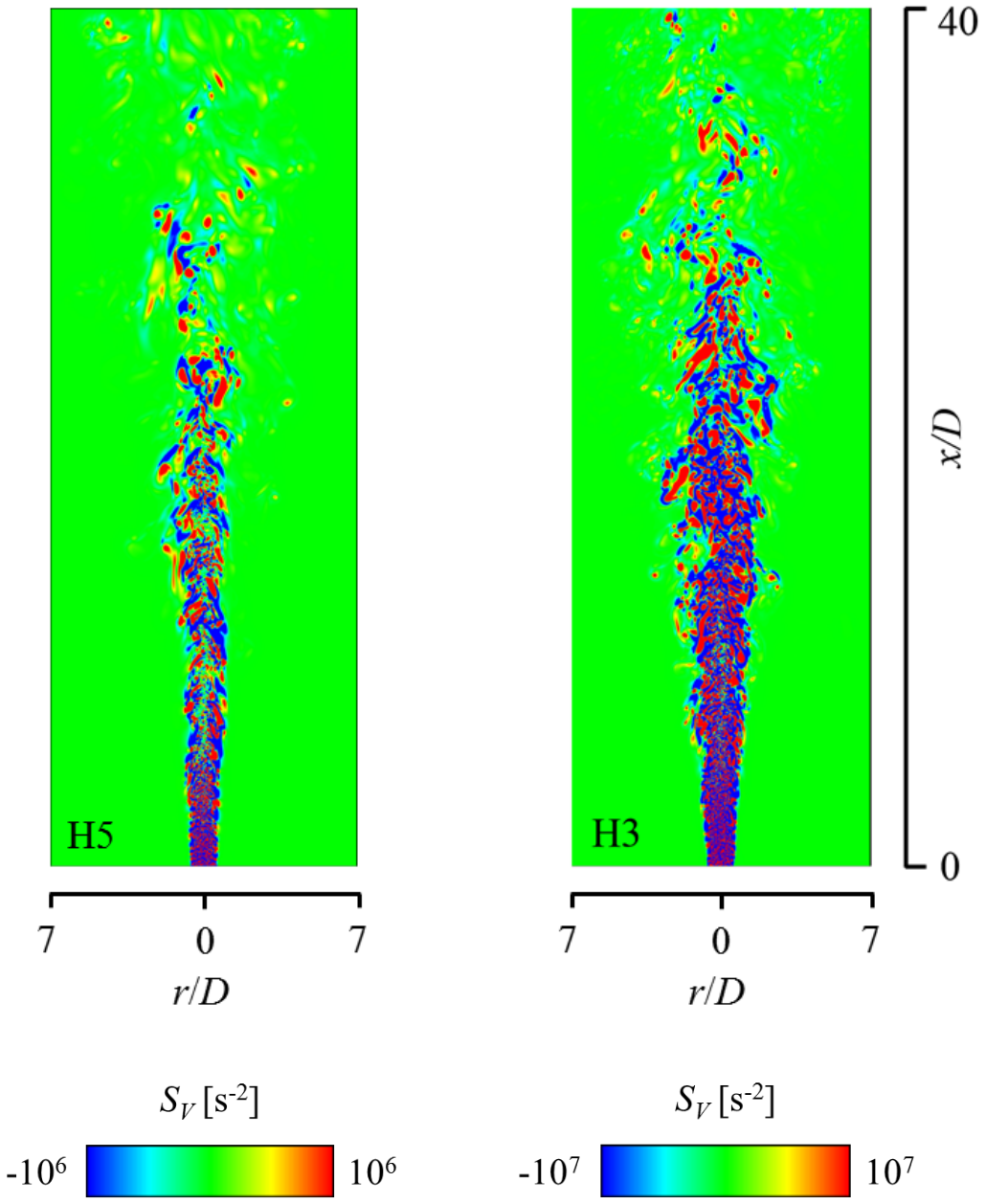

Figure 2.11: Instantaneous distributions of the turbulence noise sources S_V in the H5 flame (left, $Re = 6200$) and the H3 flame (right, $Re = 10000$).

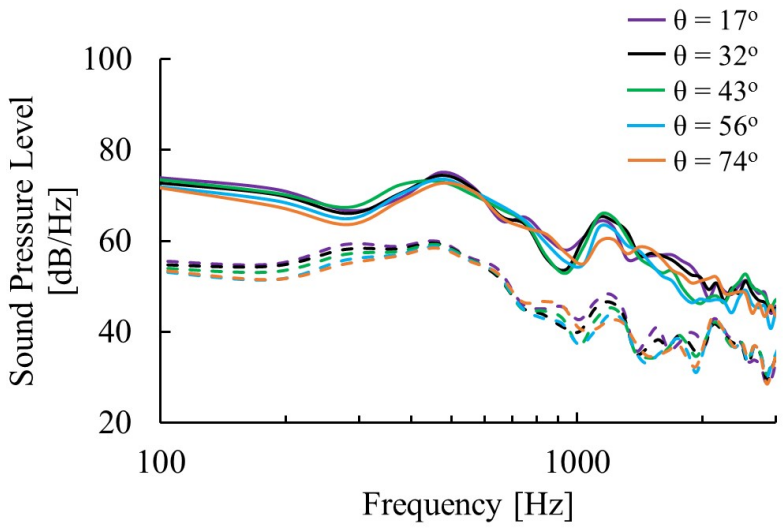

Figure 2.12: Sound pressure level spectra computed at different angles to the flame axis and at a constant radius of $r/D = 13$ centered at the nozzle exit for the H5 and H3 flames. Solid lines represent spectra for H3 Flame ($Re = 10000$), while dotted lines represent spectra for H5 Flame ($Re = 6200$). Color of each spectrum represents the angle to the flame axis at which it is computed, as depicted in the legend.

This effect compensates for the smaller magnitude of S_H. Furthermore, the nature of these noise sources are drastically different, where the combustion noise sources S_H are of monopole type and the turbulence noise sources S_V are of quadrupole type. Therefore, S_H and S_V are characterized by significantly different radial decay, with the quadrupole sources exhibiting strong directivity [37], which makes S_V an inefficient noise source, while S_H, which radiates noise omni-directionally is the dominant noise source in low Mach number turbulent non-premixed flames at the low- and mid-frequency range [2, 11, 14]. This hypothesis is further supported by the noise directivity characteristics of the two flames as illustrated in Figs. 2.12 and 2.13. In Fig. 2.12, the sound pressure level spectra computed at different angles with respect to the flame axis at a constant radius of $r/D = 13$ centered at the nozzle exit are presented for both flames (all positions lie outside the flame). The sound pressure spectra are broadband for both flames, which is a characteristic of direct combustion noise [1, 6, 11, 17, 38].

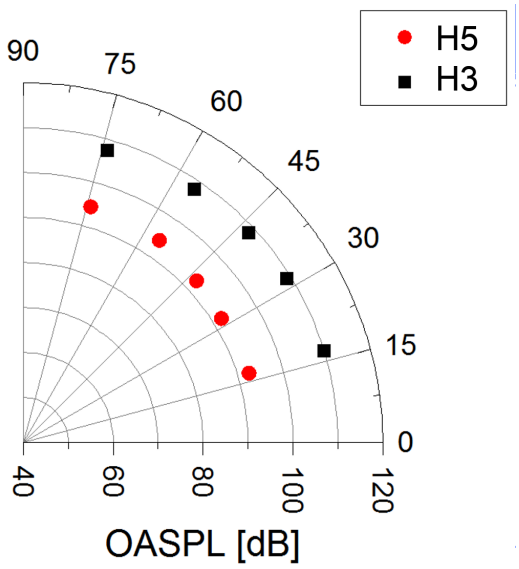

Figure 2.13: Overall Sound Pressure Levels (OASPL) computed at the same positions as those for the sound pressure spectra (shown in Fig. 2.12) for the H5 and H3 flames.

Furthermore, analysis of the noise spectra for each flame indicates similar sound pressure levels at all angles, which suggests the dominance of the combustion noise sources over the turbulence noise sources in the low- and mid-frequency range. The combustion noise spectra of both the flames are qualitatively similar in shape, but different in amplitudes with the higher *Re* H3 flame generating louder sound pressure levels across all frequencies. The differences in the sound pressure levels of the two flames' spectra lie in the range of 10-20 dB approximately. Fig 2.13 shows the OASPL computed at the same angles with respect to the flame axis and at the same radial distance from the nozzle exit for both flames. The noise directivity in terms of OASPL also indicates that the contribution of the combustion noise sources to the total sound pressure level is significantly larger, while that of the turbulence noise sources is minor, since the OASPL generated by both flames remains fairly similar for all angles. Also, the OASPL generated by the H3 flame is about 17 dB louder than that of the H5 flame.

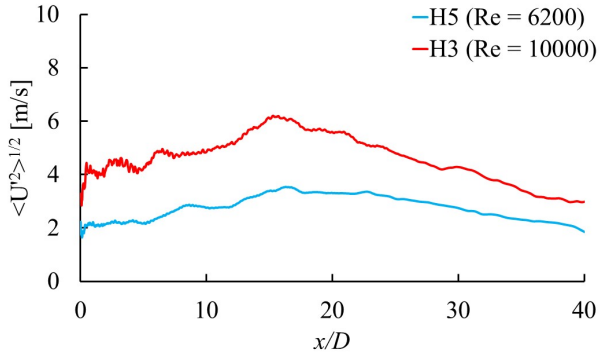

(a)

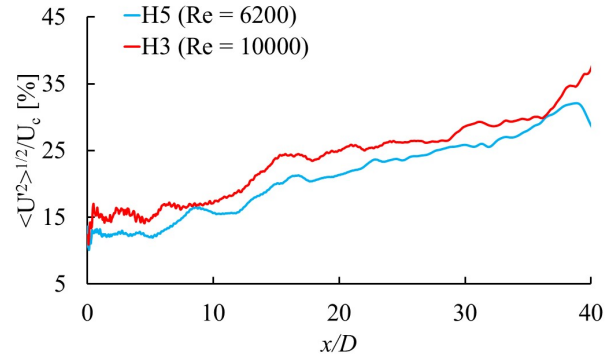

(b)

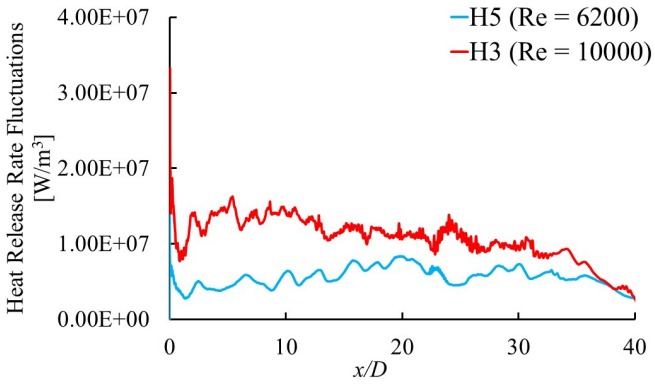

(c)

Figure 2.14: Stream-wise distributions along the nozzle lip-line of **(a)** RMS fluctuations (standard deviation) of axial velocity, **(b)** turbulence intensities (U_c is the local nozzle lip-line axial velocity), and **(c)** RMS fluctuations (standard deviation) of heat release rate.

2.3.3 Effect of Reynolds Number on Combustion Noise

Direct combustion noise originates from the unsteady volumetric expansion and contraction of reacting gases due to fluctuations in the heat release rate associated with chemical reaction [17, 36]. Analysis of the noise directivity characteristics (Figs. 2.12 and 2.13) in both turbulent non-premixed open Hydrogen jet flames suggests that the major contribution to the sound pressures generated in the low- and mid-frequency range is from the monopole combustion noise sources. The combustion noise source term S_H defined in Eq. 2.10 is a function of the fluctuating heat release rate. Therefore, the behavior of heat release rate fluctuations in the turbulent non-premixed flames has a direct consequence on the combustion noise sources. Fig. 2.14(a) shows the stream-wise distributions of the RMS fluctuations of axial velocity along the nozzle lip-line (i.e. in the shear layer where the reaction zones are present, $r/D = 0.5$) and Fig. 2.14(b) shows the stream-wise distributions of turbulence intensities along the nozzle lip-line, for the H3 and H5 flames. Both flames have the same fuel composition ($H_2/N_2 : 50/50$) but, different jet exit velocities and hence different Reynolds numbers. Higher velocity fluctuations and turbulence intensities in the H3 flame compared to the H5 flame are evident across all stream-wise locations due to the higher Reynolds number of the H3 flame. The turbulent velocity fluctuations in these non-premixed flames are responsible for inducing fluctuations in the heat release rate. Fig. 2.14(c) shows the stream-wise distributions of the RMS fluctuations of heat release rate in both flames. The results for heat release rate fluctuations are consistent with those for velocity fluctuations and turbulence intensities in Fig. 2.14(a) and 2.14(b), respectively. The stronger heat release rate fluctuations in the higher Re H3 flame produced by the larger velocity fluctuations and turbulence intensities seem to be responsible for its loudness over the lower Re H5 flame. Stronger combustion noise sources are therefore, present in the H3 flame compared to the H5 flame (see Fig. 2.10) due to the greater heat release rate fluctuations in the former, and this is evident from the results for OASPL and sound pressure level spectra in Figs. 2.9, 2.12 and 2.13.

2.4 Conclusions

In this work, the effect of Reynolds number on the noise generation in two open turbulent non-premixed Hydrogen jet flames was investigated using DNS. The flames designated as H5 ($Re = 6200$) and H3 ($Re = 10000$) have the same Nitrogen-diluted Hydrogen fuel mixture (H_2/N_2 : 50/50 volume %), but different bulk jet exit velocities which result in different Reynolds numbers for the two flames. The DNS results for velocity and temperature statistics agree well with the experimental data. Comparison of the computed sound intensity level spectra with measurements, for the H3 flame also showed acceptable agreement. Analysis of the noise generated by the two flames revealed the following:

1. Strong influence of the monopole combustion noise sources on the sound pressure field was observed in both flames as indicated by the noise directivity in terms of sound intensity level spectra and OASPL at various emission angles to the flame axis, while the influence of the turbulence noise sources was negligible.

2. Higher turbulent velocity fluctuations and turbulence intensities were observed in the H3 flame ($Re = 10000$) in comparison to the H5 flame ($Re = 6200$), which produced greater fluctuations of heat release rate in the H3 flame.

3. Consequently, the combustion noise sources which arise from the heat release rate fluctuations are stronger in the H3 flame compared to the H5 flame. Hence, the combustion noise generated by the higher Re H3 flame was found to be louder than that of the lower Re H5 flame.

References

[1] T. J. B. Smith and J. K. Kilham. Noise generation by open turbulent flames. *J. Acoust. Soc. Am.*, 35:715–724, 1963.

[2] R. B. Price, I. R. Hurle, and T. M. Sugden. Optical studies of the generation of noise in turbulent flames. *Proc. Combust. Inst.*, 12:1093–1101, 1968.

[3] W. C. Strahle and B. N. Shivashankara. A rational correlation of combustion noise results from open turbulent premixed flames. *Proc. Combust. Inst.*, 15:1379–1385, 1975.

[4] W. C. Strahle. Combustion noise. *Prog. Energy Combust. Sci.*, 4:157–176, 1978.

[5] J. K. Kilham and N. Kirmani. The effect of turbulence on premixed flame noise. *Symp. (Int.) Combust.*, 17(1):327–336, 1979.

[6] S. Kotake and K. Takamoto. Combustion noise: Effects of the shape and size of burner nozzle. *J. Sound Vib.*, 112:345–354, 1987.

[7] S. Kotake and K. Takamoto. Combustion noise: Effects of velocity turbulence of unburned mixture. *J. Sound Vib.*, 139:9–20, 1990.

[8] N. Ohiwa, K. Tanaka, and S. Yamaguchi. Noise characteristics of turbulent diffusion flames with coherent structure. *Combust. Sci. Tech.*, 90:61–78, 1993.

[9] K. Singh, S. H. Frankel, and J. P. Gore. Effects of combustion on the sound pressure generated by circular jet flows. *AIAA Journal*, 41(2):319–321, 2003.

[10] R. Barlow. editor, Proceedings of the TNF workshops, Sandia National Laboratories, 1996-2004, Livermore, CA. *available at www.ca.sandia.gov/TNF.*

[11] K. K. Singh, S. H. Frankel, and J. P. Gore. Study of spectral noise emissions from standard turbulent nonpremixed flames. *AIAA Journal*, 42:931–936, 2004.

[12] F. Flemming, A. Sadiki, and J. Janicka. Investigation of combustion noise using a LES/CAA hybrid approach. *Proc. Combust. Inst.*, 31:3189–3196, 2007.

[13] M. Ihme, H. Pitsch, and D. Bodony. Radiation of noise in turbulent non-premixed flames. *Proc. Combust. Inst.*, 32:1545–1553, 2009.

[14] M. Ihme and H. Pitsch. On the generation of direct combustion noise in turbulent non-premixed flames. *Int. J. Aeroacoust.*, 11:25–78, 2012.

[15] B. Mühlbauer, R. Ewert, O. Kornow, and B. Noll. Evaluation of the RPM approach for the simulation of broadband combustion noise. *AIAA Journal*, 48(7):1379–1390, 2010.

[16] B. Mühlbauer, R. Ewert, O. Kornow, and B. Noll. Broadband combustion noise simulation of open non-premixed turbulent jet flames. *Int. J. Aeroacoust.*, 11(1):1–24, 2012.

[17] W. C. Strahle. Some results in combustion generated noise. *J. Sound Vib.*, 23:113–125, 1972.

[18] N. M. Marinov, C. K. Westbrook, and W. J. Pitz. Detailed and global chemical kinetics model for hydrogen. San Francisco, CA, 1995. 8$^{\text{th}}$ International Symposium on Transport Properties.

[19] R. J. Kee, D.-L. Graham, J. Warnatz, M. E. Coltrin, and J. A. Miller. A fortran computer code package for the evaluation of gas-phase, multicomponent transport properties. SANDIA Report No. SAND86-8246, Sandia National Laboratories, Albuquerque NM, Livermore CA, 1986.

[20] R. J. Kee, F. M. Rupley, and J. A. Miller. Chemkin-II: A FORTRAN chemical kinetics package for the analysis of gas-phase chemical kinetics. SANDIA Report No. SAND89-8009B, Sandia National Laboratories, Albuquerque NM, Livermore CA, 1989.

[21] W. Meier, A. O. Vyrodov, V. Bergmann, and W. Stricker. Simultaneous Raman/LIF measurements of major species and no in turbulent H_2/air diffusion flames. *Applied Physics B*, 63:79–90, 1996.

[22] D. G. Pfuderer, A. A. Neuber, G. Früchtel, E. P. Hassel, and J. Janicka. Turbulence modulation in jet diffusion flames: Modeling and experiments. *Combust. Flame*, 106:301–317, 1996.

[23] T. Kitano, R. Kurose, and S. Komori. Effects of internal pressure and inlet velocity disturbances of air and fuel droplets on spray combustion field. *J. Therm. Sci. Technol.*, 8(1):269–280, 2013.

[24] T. Kitano, J. Nishio, R. Kurose, and S. Komori. Effects of ambient pressure, gas temperature and combustion reaction on droplet evaporation. *Combust. Flame*, 161(2):551–564, 2014.

[25] T. Kitano, J. Nishio, R. Kurose, and S. Komori. Evaporation and combustion of multicomponent fuel droplets. *Fuel*, 136:219–225, 2014.

[26] T. Kitano, T. Tsuji, R. Kurose, and S. Komori. Effect of pressure oscillations on flashback characteristics in a turbulent channel flow. *Energy Fuels*, 29(10):6815–6822, 2015.

[27] A. L. Pillai, M. Muto, and R. Kurose. Numerical investigation of effect of Reynolds number on noise from turbulent non-premixed hydrogen jet flames. In *Proc. ACGT2016*, Mumbai, India, 2016. Indian Institute of Technology Bombay.

[28] T. Hara, M. Muto, T. Kitano, R. Kurose, and S. Komori. Direct numerical simulation of a pulverized coal jet flame employing a global volatile matter reaction scheme based on detailed reaction mechanism. *Combust. Flame*, 162:4391–4407, 2015.

[29] T. Kitano, K. Kaneko, R. Kurose, and S. Komori. Large-eddy simulations of gas– and liquid–fueled combustion instabilities in back-step flows. *Combust. Flame*, 170:63–78, 2016.

[30] V. Moureau, C. Bérat, and H. Pitsch. An efficient semi-implicit compressible solver for large-eddy simulations. *J. Comput. Physics*, 226(2):1256–1270, 2007.

[31] G.-S. Jiang and C.-W. Shu. Efficient implementation of weighted ENO schemes. *J. Comput. Physics*, 126:202–228, 1996.

[32] M. Klein, A. Sadiki, and J. Janicka. A digital filter based generation of inflow data for spatially developing direct numerical or large eddy simulations. *J. Comput. Physics*, 186:652–665, 2003.

[33] A. M. Kempf, S. Wysocki, and M. Pettit. An efficient, parallel low-storage implementation of Klein' s turbulence generator for LES and DNS. *Comput. Fluids*, 60:58–60, 2012.

[34] C. Bogey and C. Bailly. Three-dimensional non-reflective boundary conditions for acoustic simulations: Far field formulation and validation test cases. *Acta. Acust. united Ac.*, 88:463–471, 2002.

[35] R. Piscoya, H. Brick, M. Ochmann, and P. Költzsch. Equivalent source method and boundary element method for calculating combustion noise. *Acta Acust. united Ac.*, 94(4):514–527, 2008.

[36] S. Kotake. On the combustion noise related to chemical reactions. *J. Sound Vib.*, 42:399–410, 1975.

[37] M. Ihme, M. Kaltenbacher, and H. Pitsch. Numerical simulation of flow- and combustion-induced sound using a hybrid LES/CAA approach. 497–510. Proceedings of the Summer Program, Center for Turbulence Research, 2006.

[38] B. N. Shivashankara, W. C. Strahle, and J. C. Handley. Combustion noise radiation by open turbulent flames. *AIAA paper*, 1973-1025 (1973), 1973.

Chapter 3

DNS of combustion noise of an open turbulent spray flame

3.1 Introduction

Spray combustion is an intricate multiphase phenomenon involving the turbulent dispersion of liquid fuel droplets that are convected along with the carrier gas-phase, while undergoing evaporation and subsequent combustion reaction of the evaporated fuel with the oxidizer. The above processes occur simultaneously while influencing one another, and it is this coupling of the various process between different phases that makes the analysis of spray combustion quite complicated. Experimental [1–4] and numerical studies (using LES) [5–10] on spray combustion which focus on spray evolution, droplet dispersion, evaporation, inter-phase exchanges of mass, momentum and energy, turbulence-chemistry interactions, assessment of the predictive capabilities of the numerical approaches and models employed, and combustion instability have been conducted. However, investigations (both experimental and numerical) regarding the combustion noise generation in open turbulent spray flames are insufficient in existing literature. Hence, a better understanding of the combustion noise characteristics in turbulent spray flames/combustion is needed to clarify the underlying mechanism, and to address the issue of noise emissions by improving combustor designs and to prevent the

induction of thermo-acoustic instabilities.

In this chapter, the combustion noise generated by an open turbulent spray flame with Ethanol as fuel has been investigated using Direct Numerical Simulation (DNS). This spray flame designated as EtF3 has been experimentally investigated by [3] at the University of Sydney. The multiphase reactive flow is simulated by means of an Eulerian-Lagrangian framework with two-way coupling. The turbulent gas-phase's governing equations are solved in an Eulerian framework, while the evaporating liquid fuel droplets are tracked in a Lagrangian framework. A two-step global reaction model is used for describing Ethanol combustion chemistry. The direct combustion noise generated by the unconfined spray flame is analyzed in terms of the spectral content, directivity and sound pressure levels.

3.2 Mathematical Background for Direct Numerical Simulation

The simulation in this study is DNS in the sense that no turbulence model nor any turbulence-chemistry interaction model has been used. In this investigation, however, a two-step global reaction mechanism is used for modelling combustion chemistry. In the DNS of turbulent spray flame, the carrier gas-phase is treated as an Eulerian continuum, and the dispersed fuel droplets are tracked as Lagrangian mass points. Description of the Eulerian-Lagrangian framework employed in the simulation is now presented.

3.2.1 Governing Equations of Gas-Phase

The gas-phase is solved in an Eulerian framework and its governing equations are the conservation equations for mass, momentum, energy, and species mass fraction expressed as

$$\frac{\partial \rho}{\partial t} + \nabla \cdot (\rho \boldsymbol{u}) = S_{\rho}, \tag{3.1}$$

$$\frac{\partial \rho \boldsymbol{u}}{\partial t} + \nabla \cdot (\rho \boldsymbol{u}\boldsymbol{u}) = -\nabla P + \nabla \cdot \boldsymbol{\tau} + S_{\rho u}, \tag{3.2}$$

$$\frac{\partial \rho h}{\partial t} + \nabla \cdot (\rho h \boldsymbol{u}) = \frac{\partial P}{\partial t} + \boldsymbol{u} \cdot \nabla P + \nabla \cdot (\rho D_h \nabla h) + \boldsymbol{\tau} : \nabla \boldsymbol{u} + S_{rad} + S_{\rho h}, \tag{3.3}$$

$$\frac{\partial \rho Y_k}{\partial t} + \nabla \cdot (\rho Y_k \boldsymbol{u}) = \nabla \cdot (\rho D_k \nabla Y_k) + S_{comb,k} + S_{\rho Y_k}, \tag{3.4}$$

along with the equation of state for ideal gas. In Eqs. (3.1) - (3.4), ρ is the density, $\boldsymbol{u}$ is the gas-phase velocity, P is the pressure, $\boldsymbol{\tau}$ is the stress tensor, h is the specific enthalpy, and Y_k is the mass fraction of k^{th} chemical species. S_{rad} is the source term for radiative heat loss and $S_{comb,k}$ is the source term due to combustion reaction. D_h and D_k are the gaseous thermal diffusivity and mass diffusion coefficient of k^{th} species, respectively and are defined as

$$D_h = \frac{\lambda}{\rho c_p}, \qquad D_k = \frac{\lambda}{\rho c_p}. \tag{3.5}$$

assuming unity Lewis number ($Le = 1$). Here λ is the thermal conductivity and c_p is the specific heat.

Furthermore, phase coupling between the gas-phase and dispersed-phase (fuel droplets) is achieved through the Particle-Source-In-Cell (PSI-Cell) approach [11]. In the concept of PSI-Cell approach, each computational cell is considered as a control volume, and each droplet is regarded as a source of mass, momentum and energy to the gas-phase. As the evaporating fuel droplets pass through a cell, the change in their mass, momentum and energy is treated as a source (or sink) to the gas-phase's mass, momentum and energy, respectively. This is done via. source terms S_ρ, $S_{\rho u}$, $S_{\rho h}$, and $S_{\rho Y_k}$ appearing in Eqs. (3.1) - (3.4), which represent the interactions between gas-phase and dispersed-phase (making two-way coupling possible), and they are evaluated as follows

$$S_\rho = -\frac{1}{\Delta V}\sum_N \frac{dm_d}{dt}, \tag{3.6}$$

$$S_{\rho u} = -\frac{1}{\Delta V}\sum_N \frac{dm_d \boldsymbol{u}_d}{dt}, \tag{3.7}$$

$$S_{\rho h} = -\frac{1}{\Delta V}\sum_N \frac{dm_d h_d}{dt}, \tag{3.8}$$

$$\begin{aligned} S_{\rho Y_k} &= -\frac{1}{\Delta V}\sum_N \frac{dm_d}{dt} \quad \text{for fuel} \quad (k = F), \\ &= 0 \quad \text{for other chemical species} \ (k \neq F). \end{aligned} \tag{3.9}$$

Here ΔV is the volume of each control volume (each computational grid cell) for the gas-phase calculation, m_d the fuel droplet mass, $\boldsymbol{u}_d$ the droplet velocity, h_d the specific enthalpy of a fuel droplet, and N the number of fuel droplets within a control volume.

3.2.2 Governing Equations of Dispersed-Phase

For evaporation of the fuel droplets, a non-equilibrium Langmuir-Knudsen evaporation model [12–15] is employed since, non-equilibrium effects become significant for droplet diameters $d_d < 50\mu$m [14]. The spray flame in this study is dilute as the volumetric loading of droplets is small, and hence, collisions and coalescence of droplets are neglected. The evaporating fuel droplets of the dispersed-phase are tracked individually using a Lagrangian framework [13–17] by solving the equations for droplet position $x_{d,i}$,

velocity $u_{d,i}$, temperature T_d, and mass m_d given by

$$\frac{dx_{d,i}}{dt} = u_{d,i}, \tag{3.10}$$

$$\frac{du_{d,i}}{dt} = \frac{f_1}{\tau_d}(u_i - u_{d,i}) + \mathrm{g}_i, \tag{3.11}$$

$$\frac{dT_d}{dt} = \left(\frac{\mathrm{Nu}}{3\mathrm{Pr}}\right)\left(\frac{c_p}{c_{p,d}}\right)\left(\frac{f_2}{\tau_d}\right)(T - T_d) + \frac{1}{m_d}\left(\frac{dm_d}{dt}\right)\frac{L_V}{c_{p,d}}, \tag{3.12}$$

$$\frac{dm_d}{dt} = -\left(\frac{\mathrm{Sh}}{3\mathrm{Sc}}\right)\frac{m_d}{\tau_d}\ln(1 + B_M). \tag{3.13}$$

Here, T is the gas-phase temperature, c_p is the specific heat of gas mixture, $c_{p,d}$ is the specific heat of fuel droplet, and g_i is the gravitational acceleration. The latent heat of vaporization L_V at droplet temperature T_d is calculated by

$$L_V = L_{V,T_{BL,atm}}\left(\frac{T_{CL} - T_d}{T_{CL} - T_{BL,atm}}\right)^{0.38}, \tag{3.14}$$

where, $L_{V,T_{BL,atm}}$ is the latent heat of vaporization at atmospheric pressure, T_{CL} is the critical temperature of fuel, and $T_{BL,atm}$ is the boiling point of fuel at atmospheric pressure. The droplet response time τ_d is given by

$$\tau_d = \frac{\rho_d {d_d}^2}{18\mu}, \tag{3.15}$$

where, d_d is the droplet diameter, ρ_d is the fuel droplet density and μ is the gas-phase dynamic viscosity. The gas-phase Prandtl and Schmidt numbers are defined as

$$\mathrm{Pr} = \frac{\mu c_p}{\lambda}, \qquad \mathrm{Sc} = \frac{\mu}{\rho D_k}, \tag{3.16}$$

respectively. The Nusselt and Sherwood numbers are given by

$$\mathrm{Nu} = 2 + 0.552{\mathrm{Re}_{\mathrm{sl}}}^{1/2}\mathrm{Pr}^{1/3}, \qquad \mathrm{Sh} = 2 + 0.552{\mathrm{Re}_{\mathrm{sl}}}^{1/2}\mathrm{Sc}^{1/3}, \tag{3.17}$$

respectively. Here, $\mathrm{Re}_{\mathrm{sl}}$ is the droplet Reynolds number based on the slip velocity $U_{sl} = |u_i - u_{d,i}|$ and expressed by

$$\mathrm{Re}_{\mathrm{sl}} = \frac{\rho U_{sl} d_d}{\mu}. \tag{3.18}$$

The Spalding mass transfer number B_M in Eq. (3.13) is calculated as

$$B_M = \frac{Y_{F,s} - Y_F}{1 - Y_{F,s}}. \tag{3.19}$$

Where, Y_F is the mass fraction of fuel vapour on the far-field condition for the droplets (the same condition is used for u_i and T), and $Y_{F,s}$ is the fuel vapour mass fraction on the droplet surface calculated as follows

$$Y_{F,s} = \frac{X_{F,s}}{X_{F,s} + (1 - X_{F,s})W_{avg}/W_F}, \tag{3.20}$$

$$X_{F,s} = \frac{P_{sat}}{P} - \left(\frac{2L_k}{d_d}\right)\beta, \tag{3.21}$$

Here, P_{sat} is the saturated vapour pressure, W_{avg} is the average molecular weight of mixture gas, W_F is the molecular weight of the fuel vapour, and $X_{F,s}$ is the fuel vapour mole fraction at the droplet surface, for which the non-equilibrium effects are accounted for using the Langmuir-Knudsen evaporation law [12–14]. In Eq. (3.21), L_K is the Knudsen layer thickness, and β is the non-dimensional evaporation parameter computed as [13, 14]

$$L_k = \frac{\mu[2\pi T_d(R/W_F)]^{1/2}}{\mathrm{Sc}\ P}, \tag{3.22}$$

$$\beta = -\left(\frac{\rho_d \mathrm{Pr}}{8\mu}\right)\frac{d{d_d}^2}{dt}. \tag{3.23}$$

Here, R is the universal gas constant ($R = 8.314$ J/mol K). In Eqs. (3.11) and (3.12), f_1 and f_2 are the corrections of Stokes drag and heat transfer for an evaporating fuel droplet, respectively and are evaluated as [14, 18–20]

$$f_1 = \frac{1 + 0.0545\mathrm{Re_{sl}} + 0.1{\mathrm{Re_{sl}}}^{1/2}(1 - 0.03\mathrm{Re_{sl}})}{1 + b|\ \mathrm{Re}_b\ |^c}, \tag{3.24}$$

$$b = 0.06 + 0.077\exp(-0.4\mathrm{Re_{sl}}), \tag{3.24a}$$

$$c = 0.4 + 0.77\exp(-0.04\mathrm{Re_{sl}}), \tag{3.24b}$$

$$f_2 = \frac{\beta}{e^\beta - 1}, \tag{3.25}$$

where, Re_b is the droplet Reynolds number based on the blowing velocity U_b given by

$$\mathrm{Re}_b = \frac{\rho U_b d_d}{\mu}. \tag{3.26}$$

3.2.3 Reaction Model

The liquid spray fuel of the turbulent flame under investigation is Ethanol (C_2H_5OH). Using a detailed reaction mechanism for describing the combustion reaction of gaseous Ethanol, in the DNS of this jet flame would be computationally cumbersome and impractical. Hence, a two-step global reaction mechanism [21] with 6 species (C_2H_5OH, O_2, CO_2, H_2O, N_2 and CO) is used to model Ethanol combustion. This simplified reaction mechanism was constructed by modifying the reaction rate parameters and provides good reproducibility of experimentally measured flame speeds in fuel-air mixtures, while also being able to predict rich and lean flammability limits, flame temperature and burned gas composition with reasonable accuracy for a wide range of equivalence ratios [21]. There are several DNS studies on spray combustion that use similar type of global reaction mechanisms (one- or two-step chemistry) [22–24]. Furthermore, to capture the physics of interest in the present investigation, a simplified reaction mechanism would suffice. The two-step global chemistry is as follows

$$C_2H_5OH + 2O_2 \xrightarrow{k_1} 2CO + 3H_2O, \tag{3.27}$$

$$CO + \frac{1}{2}O_2 \underset{k_{-2}}{\overset{k_2}{\rightleftarrows}} CO_2. \tag{3.28}$$

Here, k_1 is the rate of Ethanol oxidation in Eq. (3.27) and k_2 is the rate of forward reaction for CO oxidation in Eq. (3.28). The reaction rates are expressed as modified Arrhenius formulations [21] given below

$$k_1 = 1.8 \times 10^{12} \exp\left(\frac{-30}{RT}\right) [C_2H_5OH]^{0.15}[O_2]^{1.6}, \tag{3.29}$$

$$k_2 = 10^{14.6} \exp\left(\frac{-40}{RT}\right) [CO]^1[H_2O]^{0.5}[O_2]^{0.25}, \tag{3.30}$$

And, the reverse reaction in Eq. (3.28) has a rate k_{-2} that is defined according to [21]

$$k_{-2} = 5 \times 10^8 \exp\left(\frac{-40}{RT}\right) [CO_2]^1. \tag{3.31}$$

In Eqs. (3.29) - (3.31), the terms in square brackets represent the molar concentrations (moles/m^3) of different chemical species. The molar concentration $[X_k]$ of k^{th} species

is, $[X_k] = [\rho Y_k / W_k]$, where W_k is the molecular weight of k^{th} species. The two-step global reaction model used in this study provides a more accurate estimation of the flame parameters as compared to a one-step global reaction model [21].

3.2.4 Radiation Model

The source term S_{rad} in the governing equation for energy conservation, i.e. Eq. (3.3) accounts for the radiative heat loss rate per unit volume. It is modeled using an optically thin approximation [25, 26] of radiative heat transfer between a fluid element in the flame and the cold surroundings. The radiative loss S_{rad} is estimated as

$$S_{rad} = 4\sigma \left(T^4 - {T_b}^4\right) \left[\sum_k p_k a_{p,k}\right]. \tag{3.32}$$

Where $\sigma = 5.669\text{e}-08$ [W/m^{2}K^4] is the Stefan-Boltzmann constant, T is the gas-phase temperature, T_b is the background temperature and is assumed to be 300 K, p_k is the partial pressure of k^{th} chemical species in atmospheres, and $a_{p,k}$ is the Planck mean absorption coefficient of the k^{th} species. The Planck mean absorption coefficients have been evaluated using RADCAL [25] and the curve fits of $a_{p,k}$ for the radiating species considered in this model, viz. CO_2, H_2O and CO, are expressed as polynomial functions of temperature and documented in [25, 26].

3.3 Computational Setup

The open turbulent Ethanol spray flame designated EtF3 has been experimentally investigated using a laboratory scale piloted spray burner by [3] at the University of Sydney. Fuel spray and carrier air issue out of a central jet nozzle which is surrounded by a coaxial pilot annulus and an outer stream of primary co-flowing air. The entire co-flow/burner assembly is mounted in a vertical wind tunnel that supplies a secondary co-flow of air at the same velocity as the primary air co-flow [3]. The exit plane of the burner and primary co-flow are situated 59 mm downstream of the exit plane of the wind tunnel. Parameters of the Ethanol spray flame measured at the burner exit for

Table 3.1: Flow parameters of the central jet of spray flame at burner exit.

Flame designation	EtF3
Fuel	Ethanol
Jet diameter, D [mm]	10.5
Bulk jet velocity, U_{jet} [m/s]	24
Bulk velocity co-flow stream [m/s]	4.5
Carrier air mass flow rate [g/min]	150
Liquid fuel injection rate [g/min]	45
Measured liquid flow at exit [g/min]	30.7
Vapour fuel flow rate at exit [g/min]	14.3
Jet Reynolds number, Re [–]	19,700
Eckert number, Ec [–]	3.7×10^{-4}
Jet Mach number, M $= U_{jet}/C_\infty$ [–]	0.07
Equivalence ratio at jet exit, ϕ_{exit} [–]	0.85
Initial droplet & ambient temperature [K]	293.15

Table 3.2: Parameters of annular pilot at burner exit.

Fuel	Acetylene (C_2H_2) + Hydrogen (H_2) + Air
Pilot diameter [mm]	25
Bulk velocity pilot (burned), U_{pilot} [m/s]	11.6
Pilot temperature [K]	2493
Pilot composition ($Y_{CO_2} : Y_{H_2O} : Y_{N_2}$)	(0.1722 : 0.10575 : 0.722)

the central jet nozzle are listed in Table 3.1, while those for the annular pilot flame are listed in Table 3.2. The same parameters are used for the DNS. The pilot consists of the fully-burned product of the stoichiometric mixture of 5.08% Acetylene (C_2H_2), 10.17% Hydrogen (H_2) and 84.75% air by volume, and its adiabatic flame temperature is 2493 K. Thus, the chemical species constituting the pilot flame at the burner exit are CO_2, H_2O and N_2, whose respective mass fractions have been calculated a priori and listed in Table 3.2. The pilot flame supplies the heat for evaporation of the liquid fuel droplets, ignites the vaporized Ethanol and is essential for stabilizing the main spray flame. In the experiments, the spray was generated using an ultrasonic nebulizer situated inside the burner about 215 mm upstream of the jet exit plane. The ultrasonic nebulizer produces fine dispersed droplets, some of which evaporate inside the central nozzle tube before reaching the exit and hence, the measured liquid flow rate at the nozzle exit is smaller than the actual liquid fuel injection rate (see Table 3.1). The EtF3 spray flame burns in the partially premixed combustion regime. Complete description of the burner setup is available in [3].

A schematic of the computational domain is illustrated in Fig. 3.1(a) showing the domain size and configuration of the piloted spray burner's exit used as inflow boundary condition for the DNS. Cell distributions in the x-y and y-z planes of the computational domain are also presented in Fig. 3.1(b). The DNS is performed on a staggered Cartesian grid consisting of 1160×400×400 grid points (a total of 185.6 million points) in the x-, y- and z-directions, respectively. The domain size is approximately $94D \times 49D \times \times\ 49D$ in the x-, y- and z-directions, respectively. Fuel droplets are randomly injected from the central jet nozzle exit plane in a polydisperse manner, and the maximum droplet size used in the DNS is 80 μm. Size distribution of the injected fuel droplets is prescribed using a log-normal Probability Density Function (PDF) obtained from the best fit curve of experimental droplet size distribution data, as depicted in Fig. 3.2. In DNS of spray combustion, the grid spacing should be capable of resolving the Kolmogorov length scales and the flame reaction zone thickness. However, the grid spacing must be sufficiently larger than the droplets' sizes in order to get accurate estimates of droplet evaporation

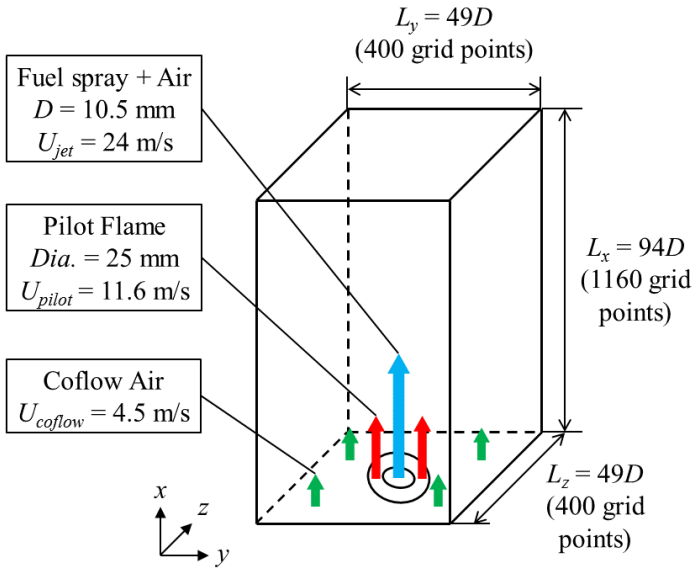

(a) Computational domain size and inflow configuration of the piloted spray flame.

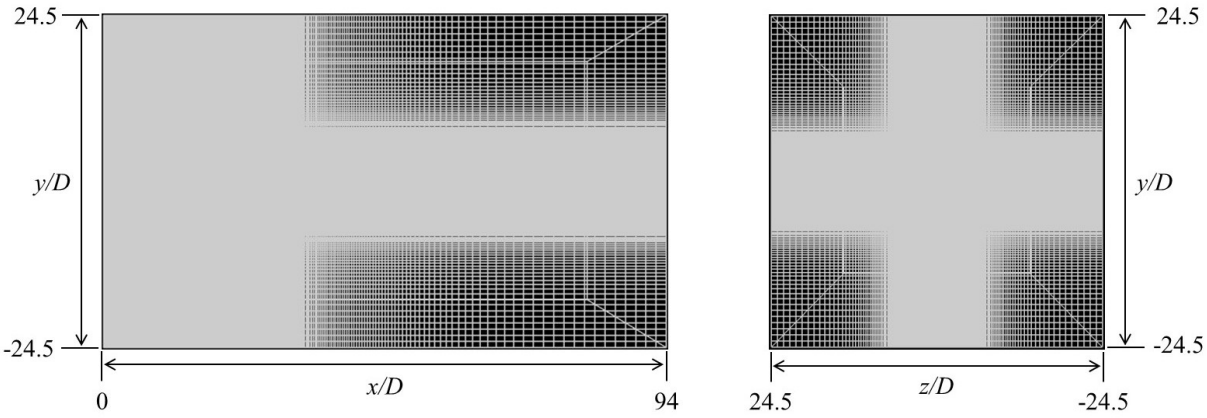

(b) Cell distributions in the x-y and y-z planes of the Cartesian grid.

Figure 3.1: Schematic of the computational domain and cell distribution in the Cartesian grid used for DNS ($D = 10.5$ mm).

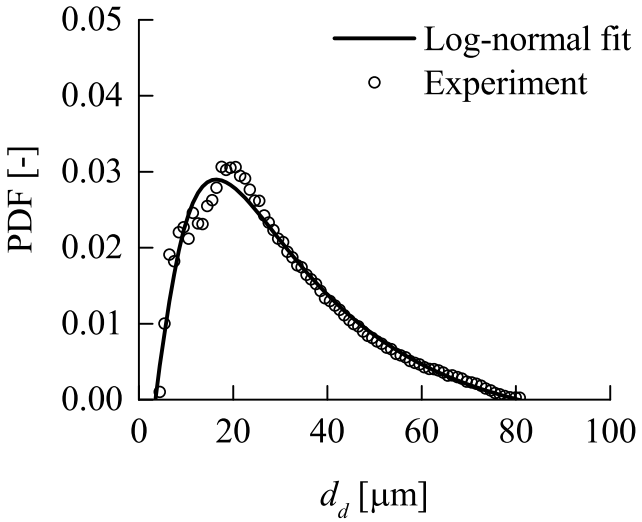

Figure 3.2: Droplet size distribution PDF used for injecting fuel droplets at the central jet nozzle inflow in the DNS (symbols represent experimental data [3]).

dynamics using the PSI-Cell approach [27, 28]. Hence, a minimum grid spacing of $\Delta x = \Delta y = \Delta z = 150\mu$m is used in this study. The mesh is non-uniform, but it is fine in the core region of the jet flame.

3.4 Numerical Procedure

The DNS is performed using an in-house thermal flow analysis code FK^3 [10, 17, 29–31], which employs a pressure-based semi-implicit solver for compressible flows [32], whose algorithm consists of a fractional-step method. The spatial derivatives of the convective terms in the momentum equation are approximated using a 6^{th} order accurate central difference scheme, while the convective terms in the governing equations of the scalar quantities are evaluated using the WENO (Weighted Essentially Non-Oscillatory) scheme [33]. The spatial derivatives of the stress tensor terms are evaluated using a 4^{th} order central difference scheme and those of the diffusive terms are discretized by a 2^{nd} order central difference scheme. The time integration of the convective terms is performed using a 3^{rd} order explicit TVD Runge-Kutta method. Additionally, all the thermodynamic properties and transport coefficients taking temperature dependence

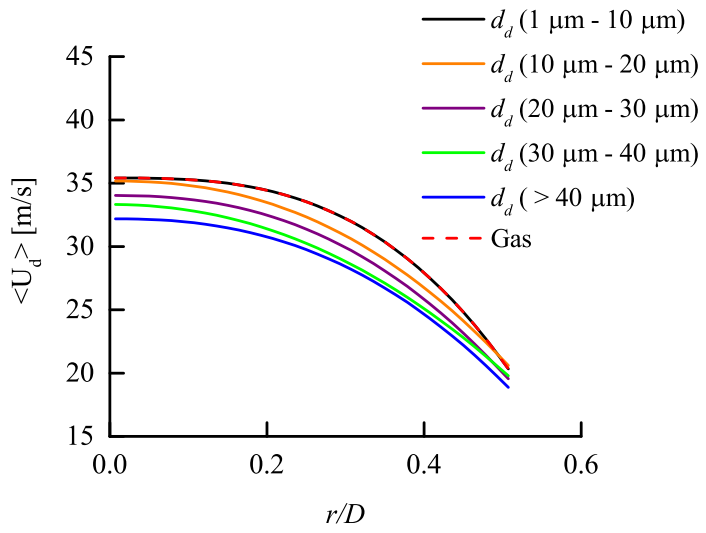

Figure 3.3: Radial profiles of mean axial velocity of gas-phase and droplets in different size ranges obtained from measurements [3].

into consideration are obtained from CHEMKIN [34, 35]. Radial profiles of mean axial velocity for the gas-phase and droplets in different size ranges (e.g., 1-10 μm, 10-20 μm, 20-30 μm, etc.), used as inlet boundary conditions in the DNS are depicted in Fig. 3.3. These mean velocity profiles are obtained from the best fit curves to the experimental data for radial profiles of mean axial velocity for various droplet size ranges, measured close to the central jet nozzle's exit plane at $x/D = 0.3$. It is also assumed that the radial profile of mean axial velocity for gas-phase is the same as that for the smallest droplet size range ($1\mu\text{m} \leq d_d \leq 10\mu\text{m}$), and this assumption is in accordance with the experiment [3]. Furthermore, these mean velocity profiles represent fully developed two phase flow behaviour [3].

The radial profiles of mean axial velocity in Fig. 3.3 reveal an important feature of droplet behaviour. It is evident that near the central jet nozzle exit plane ($x/D = 0.3$), the velocity magnitudes are different for droplets in various size ranges and the mean velocities decrease with increasing droplet sizes. In the experiment, as the fuel droplets are carried by air from the nebulizer to the nozzle exit, the smaller droplets experience higher acceleration from the carrier air compared to the larger droplets. This is because, the smaller droplets have shorter response times compared to larger droplets with longer

response times (smaller τ_d means smaller Stokes number and better responsiveness to the turbulent fluctuations of the carrier gas-phase). Hence, larger droplets experiencing lower acceleration from the carrier air inside the central tube of the burner, have slower mean velocities at the nozzle exit.

Additionally, for the central spray nozzle transient turbulent fluctuations generated using a digital filter based technique [36, 37] are superimposed on the gas-phase mean velocities at the nozzle exit to simulate artificial inflow turbulence. The experimental data for radial profile of RMS fluctuations of gas-phase axial velocity at the nozzle exit is supplied to the artificial turbulence generator. For the region outside pilot annulus exit (i.e. for $r > 12.5$ mm) at the inflow plane, an axial co-flow air velocity of 4.5 m/s is imposed (see Table 3.1) while the other velocity components are set to zero, and Neumann condition is applied to other physical quantities. At the outflow and lateral boundaries, the Neumann condition is imposed for all physical quantities. To minimize the amplitude of acoustic waves reflected at the boundaries of the computational domain, a sponge zone combining grid stretching and Laplacian filtering [38] is used in the far downstream region towards the outflow boundary (last 30 grid points in x-direction), to dissipate the flow fluctuations and acoustic waves before they reach the outflow boundary. Artificial damping provided by the Laplacian filter is applied progressively in the sponge zone. Also, absorbing layers comprising of grid stretching and artificial dissipation which is obtained by applying a sixth order filter [39], are implemented towards the lateral boundaries of the computational domain. This helps to damp out the outgoing acoustic waves, thereby minimizing the reflection of acoustic waves at the lateral boundaries.

The CPU time required for the DNS computation is approximately 516000 hours by parallel computation using 1024 cores on a CRAY-XC40 supercomputer at the Academic Centre for Computing and Media Studies (ACCMS), Kyoto University (the actual time required for the computation is approximately 504 hours of real time).

3.5 Results and Discussion

3.5.1 Flow-Field

The instantaneous gas-phase temperature field along with the dispersed fuel droplets (grey entities) obtained from DNS, representing the spray flame's predicted structure and features are illustrated in Fig. 3.4. As the fuel droplets get convected downstream by the carrier gas-phase, they undergo evaporation which results in droplet size reduction. The vaporized fuel subsequently gets ignited by the surrounding high temperature gas-phase leading to further combustion. As the convecting fuel droplets undergo evaporation by the surrounding hot gases, a steady reduction in droplet count is apparent with increasing downstream distance. Furthermore, mixing occurs between the central jet (Ethanol + air) and the hot pilot stream, between the hot pilot stream and the co-flow, as well as the entrainment of co-flowing air into the central jet. This produces more droplet dispersion with increasing downstream distance from the burner exit plane. Therefore, spray combustion is a complex multiphase process wherein all the above phenomena are occurring simultaneously resulting in the exchange of mass, momentum and energy between the gas-phase and dispersed phase.

The DNS is initially run for 3 flow-through times to allow for flame development. Here, one flow-through time is defined as $40D/U_{jet}$ using velocity U_{jet} = 24 m/s and length in the x-direction equal to $40D$ (D is the central jet diameter) from the nozzle exit. Sampling of the flow field quantities is commenced there onwards by running the simulation for another 4 flow-through times, which roughly corresponds to 70 ms of physical time. The simulation time is found to be long enough for the flow field of the spray flame to attain statistical stationarity. Computed results for the flow field statistical quantities are validated against experimental measurements to assess the fidelity of the DNS. It should be noted that, when quantities are expressed within triangular parentheses "<>" in succeeding figures, it implies time averaging of the respective quantities. Fig. 3.5 shows the radial profiles of droplet averaged (includes droplets of all sizes) axial velocity as well as gas-phase mean axial velocity compared with measurements, at

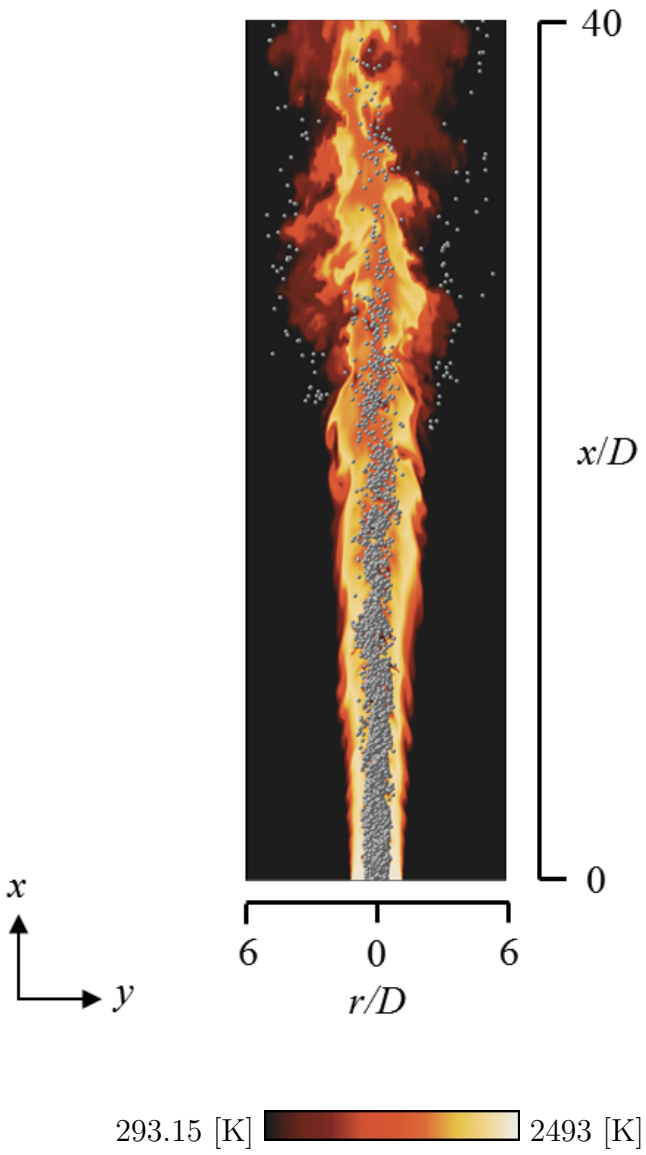

Figure 3.4: Instantaneous gas-phase temperature field of the turbulent spray flame computed with DNS, along with the dispersed Ethanol droplets (droplet sizes are exaggerated) in the central x-y plane.

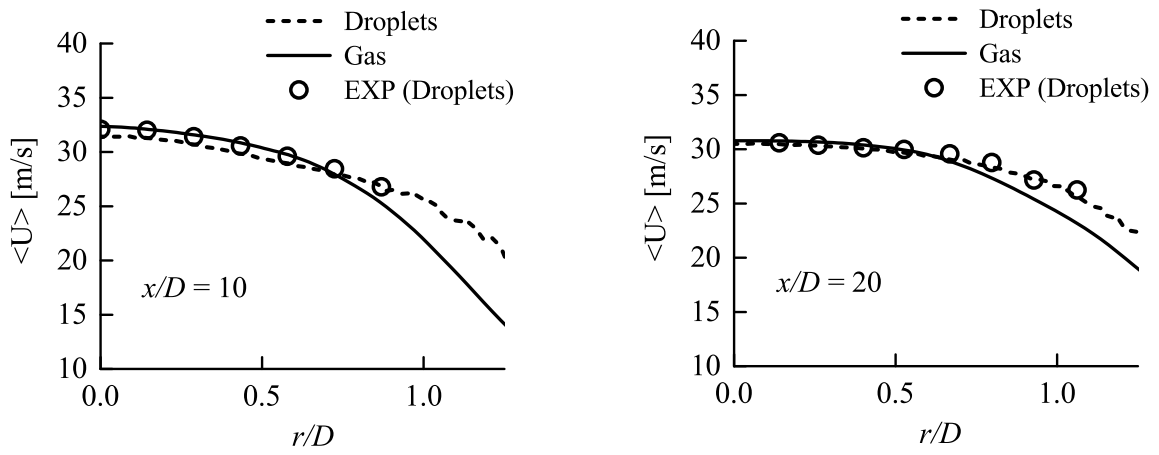

Figure 3.5: Radial profiles of droplet averaged axial velocity and mean gas-phase axial velocity compared with measurements [3] at different stream-wise locations.

different stream-wise locations.

At $x/D = 10$, the gas-phase mean axial velocity is nearly the same as the experimental droplet averaged axial velocity. Computed droplet averaged axial velocity also conforms to the measurements. Once the fuel droplets exit the nozzle, they are initially accelerated by the thermal expansion of the gas-phase caused by heat release. Hence, both the gas-phase and fuel droplets retain much of their momentum around $x/D = 10$ due to the thermal expansion process. However, at the further downstream location of $x/D = 20$, the gas-phase mean axial velocity seems to be slowing down compared to the droplet averaged axial velocity for radial locations $r/D > 0.5$. This deviation happens because, with increasing downstream distance and especially for the far downstream location of $x/D = 20$, there will be a general shift towards larger droplets among the existing ones, as the smaller droplets evaporate faster. The larger droplets have longer relaxation times (higher Stokes numbers) due to their higher inertia and hence, are less responsive to the turbulent fluctuations in the gas-phase. As a result, the velocities of the larger droplets have not decelerated to the same extent as that of the gas-phase. Therefore, the larger droplets travel faster than the gas-phase while prescribing trajectories different from the gas-phase streamlines. Similar behaviour has been observed in the experiment for the EtF3 spray flame [3], where velocities of larger droplets are lower

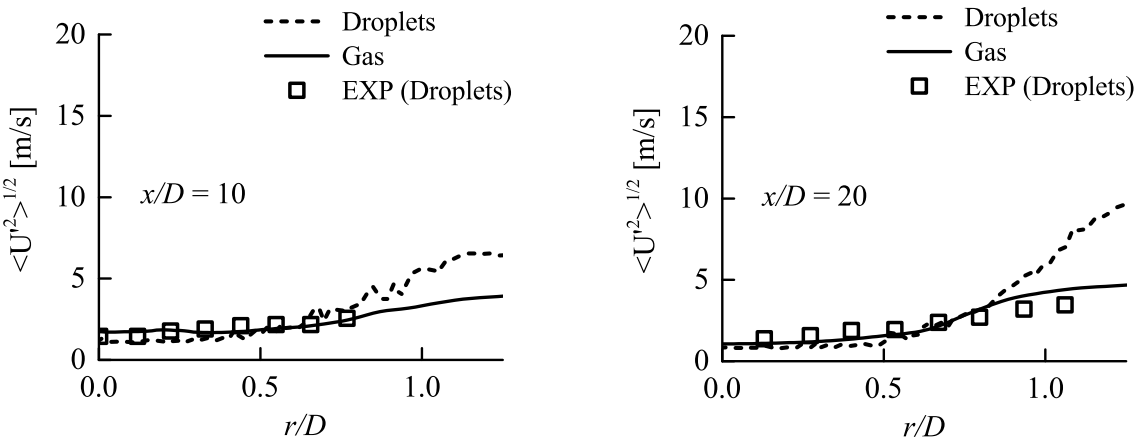

Figure 3.6: Radial profiles of RMS fluctuations of axial velocity of droplets and gas-phase compared with measurements [3] at different stream-wise locations.

than the gas-phase velocity (assumed to correspond to the smallest droplet sizes $d_d < 10$ μm) close to the jet nozzle exit, while at the far downstream locations larger droplets are faster than the gas-phase.

Similarly, Fig. 3.6 shows the radial profiles of RMS fluctuations of axial velocity for droplets (includes droplets of all sizes) and gas-phase compared with measurements. The DNS results show good agreement with experimental data with the flame spreading and trends being well predicted. However, the DNS predictions overestimate the RMS fluctuations of axial velocity of droplets near the outer edge of the jet ($r/D > 0.8$). This is probably the effect of decreased sampling rate at radial locations farther away from the flame axis, i.e. $r/D > 0.8$ where the temperatures are high (see Fig. 3.8). Due to high surrounding gas-phase temperatures, the droplets in the outer layers near the edge of the jet evaporate at a faster rate leading to smaller droplet counts and hence, reduced sampling rate. Sampling rate is also diminished by the fact that, the radial dispersion of droplets with higher Stokes number (larger droplets with longer relaxation times) is lower, owing to the reduced responsiveness of large droplets to the turbulent fluctuations in the gas-phase. DNS predictions for the radial profiles of droplet averaged (includes droplets of all sizes) radial velocity and corresponding RMS fluctuations are depicted in Fig. 3.7, and good agreement with experimental measurements is found. Velocity

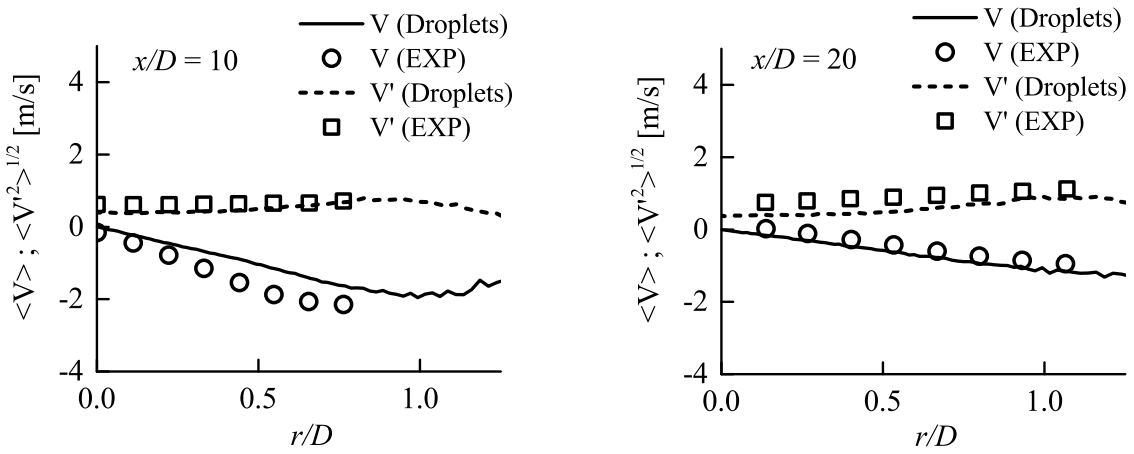

Figure 3.7: Radial profiles of droplet averaged radial velocity and corresponding RMS fluctuations compared with measurements [3] at different stream-wise locations.

statistics for the EtF3 spray flame are generally well captured by the DNS.

Furthermore, radial profiles of gas-phase excess temperature at various stream-wise locations are presented in Fig. 3.8. Some discrepancies in these DNS results, like the over-prediction of temperature at certain radial locations, and under-predicted temperature near the flame axis especially at the stream-wise location of $x/D = 10$, are attributed to the shortcomings of the two-step global reaction model for Ethanol combustion employed in this study. This reaction model has a known tendency to overestimate flame temperatures [21]. However, it is worth mentioning that in the experiments, temperature measurements were performed using thermocouples which could have introduced potential errors in the measured gas-phase temperature data. For stream-wise locations closer to the nozzle exit (e.g. $x/D = 10$) the droplet count is high, due to which the error in the temperature measured by the thermocouple is likely to be larger [6]. Hence, the discrepancies introduced in the measurement technique should be taken into consideration while comparing with the present DNS predictions for temperature. Similar discrepancies in temperature predictions have been observed in the LES by Chrigui et al. [6] and Ukai et al. [7]. However, the overall agreement between DNS and experimental results is reasonable with the temperature trends and flame width (in terms of the radial profiles of gas-phase excess temperature) being well reproduced.

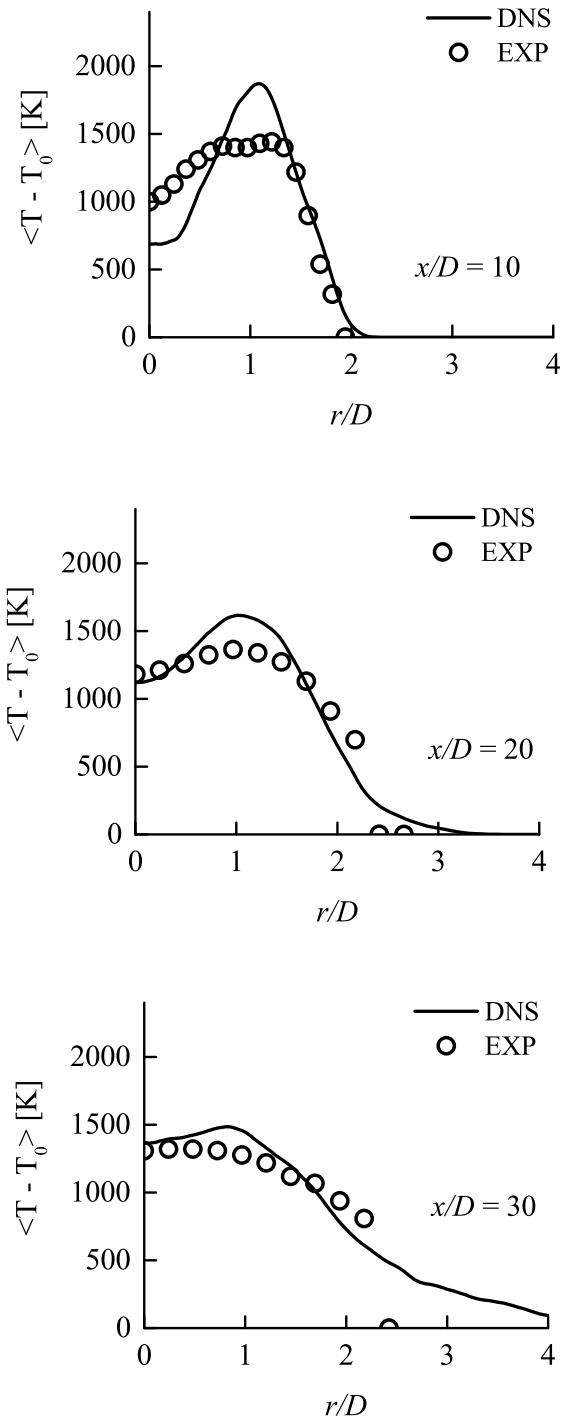

Figure 3.8: Radial profiles of gas-phase excess temperature at various stream-wise locations compared with measurements [3], T_0 is the ambient temperature (T_0 = 293.15 K).

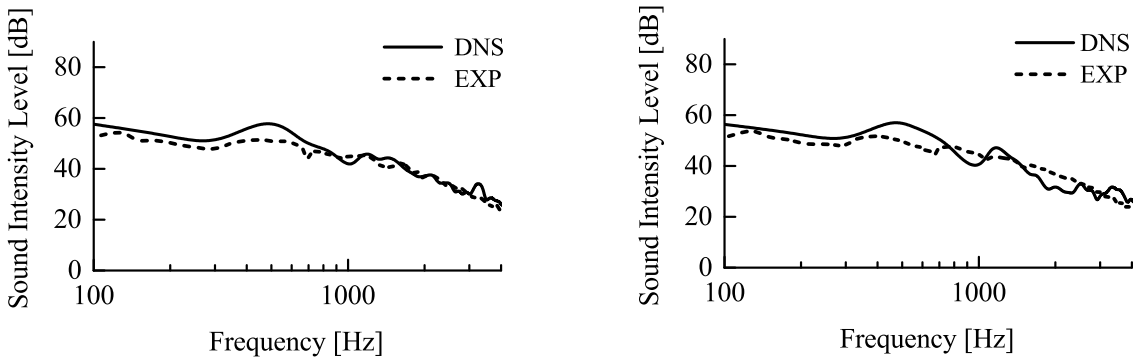

(a) $(x/D;\ r/D) = (18;\ 63)$ (b) $(x/D;\ r/D) = (43;\ 63)$

Figure 3.9: Sound intensity level spectra computed from the DNS of a turbulent non-premixed Hydrogen flame H3 [31] compared with experimental measurements [40].

3.5.2 Combustion Noise

For the EtF3 spray flame, experimental data regarding noise emissions are currently unavailable in literature, however in order to validate the ability of the employed solver to predict flame generated acoustics, the results for combustion noise from an open turbulent non-premixed Hydrogen flame [40], have been validated with measurements in Chapter 2 (Section 2.3.2) by performing DNS with the same in-house code FK^3 and similar numerical procedure. This non-premixed Hydrogen flame designated as H3 is a benchmark flame of the workshop for turbulent non-premixed flames [41, 42]. The sound intensity level spectra of the H3 flame computed from DNS in the far-field, are scaled to the same locations as those in the experiment where microphone measurements were conducted, using appropriate scaling law [43] and the comparisons are shown in Fig. 3.9. The DNS results showed acceptable agreement with the measured sound intensity level spectra in the resolved frequency range. Based on this validation, analyses of the combustion noise characteristics generated by the EtF3 spray flame have been performed.

The computational grid used in this investigation is capable of resolving a maximum frequency of 5700 Hz in the acoustic field (i.e. the region outside the flame under ambient conditions where the flow is irrotational), assuming speed of sound in ambient air with a conservative estimate of 24 points per wavelength. The DNS is executed with a constant

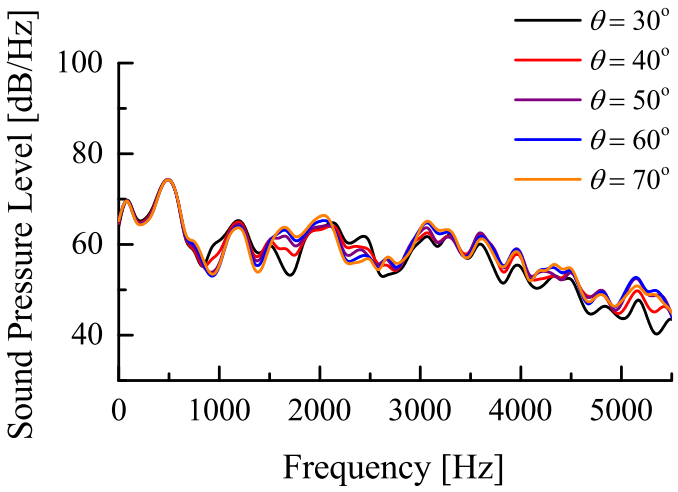

Figure 3.10: Sound pressure level spectra computed for locations at a constant radius of $r/D = 11$ centered at the nozzle exit of the EtF3 spray flame, each location corresponds to a different emission angle (θ) to the flame axis.

time increment of $\Delta t = 6 \times 10^{-7}$ s during the period of signal recording, which yields a Nyquist frequency of temporal resolution of approximately 833.333 kHz, which is much larger than the spatial resolution. For the computation of combustion noise results, fluctuating pressure signals are extracted at various locations in the acoustic field over a physical sampling time period of 61 ms. This sampling time period corresponds to roughly 3.5 flow-through times or 50 acoustic propagation times. Here, one acoustic propagation time is defined as the time required for an acoustic wave to traverse $40D$ distance from the nozzle exit in the x-direction and is calculated as $40D/C_\infty$, where C_∞ is the speed of sound in ambient air. The time period of signal extraction is divided into sections with a 50% overlap which are then used for averaging (noise spectrum evaluated for a given position in the acoustic field is also averaged over points in the azimuthal direction). The computed temporal signals are converted to the frequency domain using Fast Fourier Transform (FFT), giving a frequency resolution of 83 Hz based on Nyquist-Shannon sampling theorem. For the DNS performed in this study using a pressure-based semi-implicit compressible solver [32], the mean convective Courant number is $\mathrm{CFL}_{\mathrm{conv}} = 0.13$, while the mean acoustic Courant number is $\mathrm{CFL}_{\mathrm{acoust}} = 2.5$.

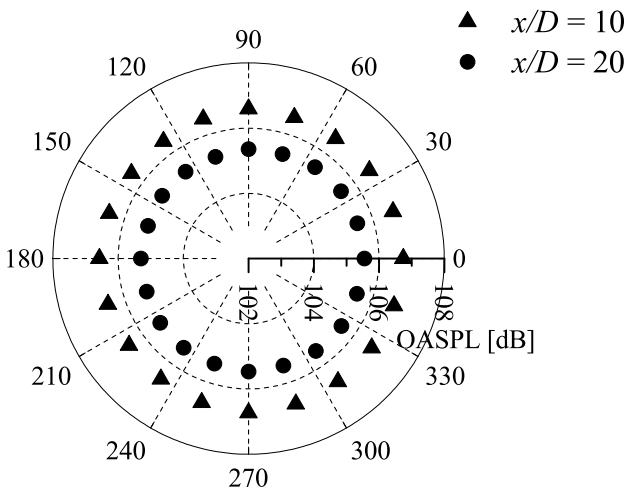

Figure 3.11: OASPL distribution with azimuthal angle (in the y-z plane) at a constant radius of $r/D = 11$, centered on the flame axis for different stream-wise locations.

The sound pressure level spectra computed for positions at a constant distance of $r/D = 11$ centered at the nozzle exit, that correspond to different emission angles θ with respect to the flame axis are shown in Fig. 3.10, in order to analyze the spectral content of noise. The spectra reveal broadband nature of the noise emitted by the turbulent spray flame, which is a characteristic of direct combustion noise [44–48]. Moreover, the spectral shapes and sound pressure levels are practically similar for all emission angles, indicating dominance of the distributed monopole-type combustion noise sources.

Fig. 3.11 shows the distribution of Overall Sound Pressure Level (OASPL) in the azimuthal plane (y-z plane) at different stream-wise locations. Here, the OASPL is computed at various azimuthal angles at a constant distance of $r/D = 11$, centered on the flame axis. The OASPL represents the total energy contained in the sound pressure spectrum and signifies the loudness of noise. The OASPL is calculated by integrating the sound pressure spectrum in the frequency domain over the entire range of frequencies resolved by the computational grid. The OASPL distribution is symmetric and the omni-directionality of combustion noise radiation with respect to the flame axis in the azimuthal plane is evident. Moreover, the OASPL drops by approximately 1.2 dB from

the stream-wise location of $x/D = 10$ to $x/D = 20$.

The sound pressure spectra computed for the positions at a constant radial distance of $r/D = 11$ from the flame axis and at different stream-wise locations from the nozzle exit are depicted in Fig. 3.12. These positions are, $(x/D; r/D) = (19.05; 11)$, $(13.11; 11)$, $(9.23; 11)$, $(6.35; 11)$ and $(4; 11)$, corresponding to emission angles of $\theta = 30°$, $40°$, $50°$, $60°$ and $70°$, respectively to the flame axis. The spectra are broadband as expected, and the sound pressure levels are virtually similar at all emission angles for the low-frequencies (i.e. for frequencies up to 1000 Hz). This is due to the dominant contribution of the monopole combustion noise sources to the sound pressure at low-frequencies. This qualitatively confirms the findings that have been reported in previous investigations for low Mach number turbulent premixed [44, 46] and non-premixed [48, 49] flames, regarding the low-frequency characteristic of noise generated by turbulent combustion.

However, note that for the high-frequency noise emissions (frequencies beyond 1000 Hz), suppression of sound pressure levels with decreasing emission angle θ which corresponds to increasing distance from nozzle exit, is apparent. The reduction in sound pressure levels of the high-frequency noise emissions is more pronounced for the downstream position corresponding to $\theta = 30°$. The green dashed-dotted lines in Fig. 3.12 qualitatively indicate the decrease in sound pressure levels of the high-frequency components between the emission angles of $\theta = 70°$ and $\theta = 30°$. The average difference in the high-frequency sound pressure levels between emission angles of $\theta = 70°$ and $\theta = 30°$, calculated using linear regression analysis is found to be approximately 6.5 dB. The downstream suppression of high-frequency noise emissions is caused by refraction effects due to temperature non-uniformities within the flame, and such weak directivity in the high-frequency noise emissions has been confirmed in previous investigations of turbulent non-premixed flames [48, 50]. The temperature gradients existing in the flame lead to non-uniform speed of sound, and the high-frequency acoustic waves propagating in the downstream direction get refracted away from the flame axis, upon interaction with said sound speed inhomogeneities. Such acoustic refractions due to temperature-dependent variations in the speed of sound become increasingly significant with increasing down-

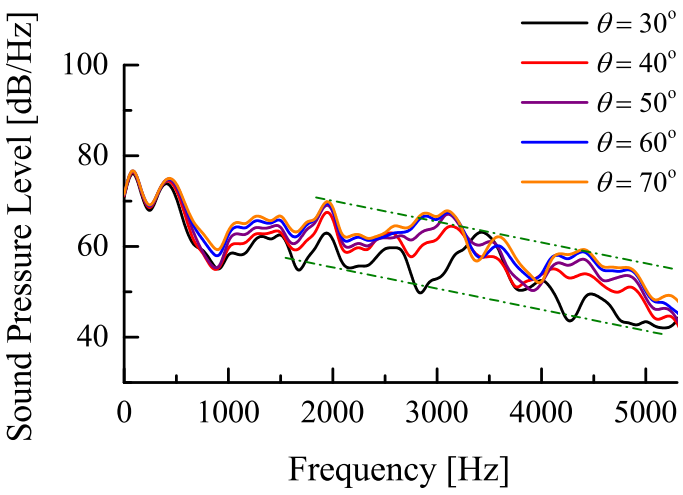

Figure 3.12: Sound pressure spectra computed at different stream-wise locations and at a constant distance of $r/D = 11$ from the flame axis, corresponding to different emission angles θ to the flame axis. The green dashed-dotted lines qualitatively indicate the decrease in sound pressure levels of the high-frequency emissions between $\theta = 70°$ and $\theta = 30°$.

stream distance (decreasing emission angle to the flame axis) [51].

The axial distributions of frequency-filtered and total OASPL computed at a fixed radial distance of $r/D = 11$ from the flame axis and at various stream-wise locations from the nozzle exit are presented in Fig. 3.13. Axial distributions of frequency-filtered OASPL are shown for two frequency regimes, namely the low-frequencies (f $\leq$ 1000 Hz) in Fig. 3.13(a) and the high-frequencies (f $>$ 1000 Hz) in Fig. 3.13(b). The total and frequency-filtered OASPL decrease from the nozzle exit $x/D = 0$ to the downstream location of $x/D = 30$. However, for the low-frequency emissions, OASPL reduces roughly by 1 dB only, while for the high-frequencies, OASPL decreases by almost 11 dB over a distance of $x/D = 0 - 30$. Hence, the high-frequency noise emissions are subjected to much stronger attenuation in the downstream direction, compared to the low-frequency emissions which are only slightly affected. This is likely caused by the refraction of high-frequency noise away from the flame axis in the downstream direction, which is induced by the variation in speed of sound associated with temperature gradients [45,

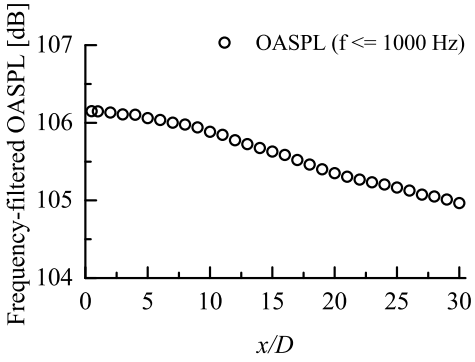

(a) Frequency-filtered OASPL for low-frequencies (f $\leq$ 1000 Hz).

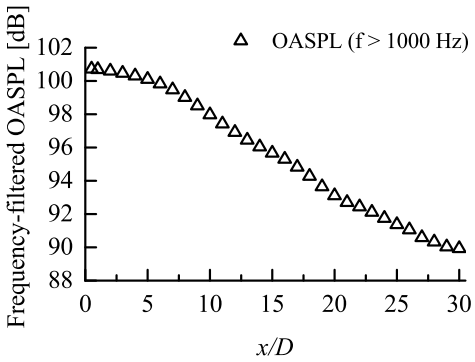

(b) Frequency-filtered OASPL for high-frequencies (f $>$ 1000 Hz).

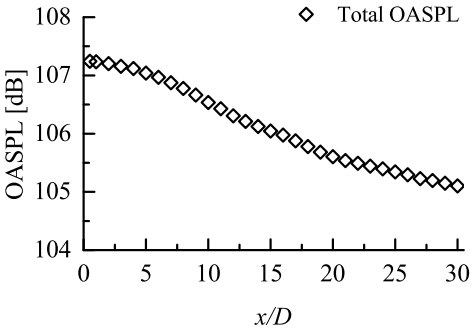

(c) Total OASPL for entire frequency range resolved by computational grid.

Figure 3.13: Axial variations of frequency-filtered and total OASPL computed at $r/D =$ 11 from the flame axis.

48, 50] in the turbulent spray flame (shear-induced refraction effects are negligible for this spray flame, owing to the very low Mach numbers in the flow field). Therefore, the existence of a zone of silence (region in the acoustic field subjected to diminished noise irradiation) for the high-frequency noise emissions in the downstream direction is apparent. Furthermore, this observation is consistent with the results in Fig. 3.12, where the suppression of sound pressure levels of the high-frequency noise emissions with decreasing emission angle to the flame axis (increasing distance from the nozzle exit) is observed.

Moreover, the axial variation of the total OASPL (computed for the entire frequency range resolved by the computational grid) shown in Fig. 3.13(c), indicates a 2.2 dB reduction in the OASPL over the distance of $x/D = 0 - 30$. The reduction in the total OASPL is just 1.2 dB greater than that of the frequency-filtered OASPL for the low-frequency regime (f $\leq$ 1000 Hz). This implies that most of the acoustic energy of combustion generated noise is concentrated in the low-frequency emissions, indicating that the major contribution of the combustion noise sources to the sound pressure lies in the low-frequencies. This again confirms the low-frequency characteristic of combustion induced noise in the turbulent spray flame.

Next, the computed sound pressure spectra of the spray flame are compared to the combustion noise similarity spectrum suggested by Tam et al. [52], as shown in Fig. 3.14. In the experimental investigation conducted by Tam et al. [52], extensive measurements showed that combustion noise has a unique spectral shape. This spectral shape was demonstrated to be the same as the similarity spectrum for large scale turbulence noise of high-speed jets, discovered by Tam, Golebiowski and Seiner [53]. The spectral shape's analytical formula is described in [52, 53]. Moreover, this spectral shape of combustion noise was found to be unaltered with variation in direction of emission, including the spectral peak which exhibited uniform directivity [52].

The noise spectra depicted in Fig. 3.14 and the positions at which they are computed, are the same as in Fig. 3.12. In the figure, the combustion noise similarity spectrum is represented by the dotted curve and has been displaced vertically for com-

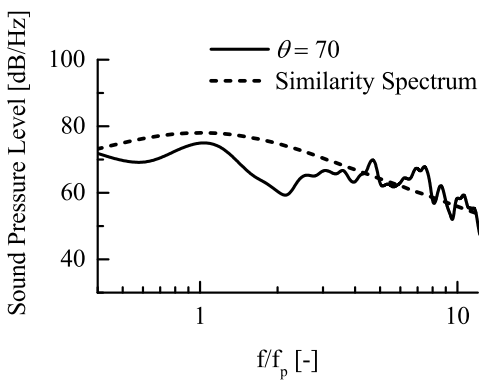

(a) $(x/D, r/D) = (4, 11)$; $\theta = 70^o$

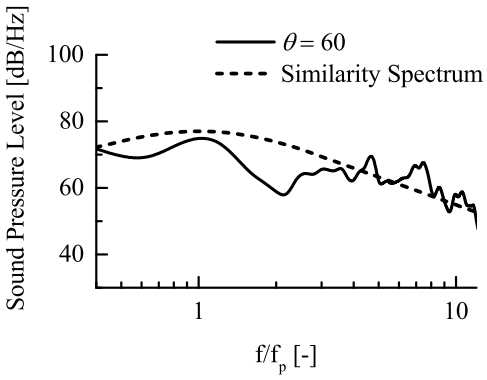

(b) $(x/D, r/D) = (6.35, 11)$; $\theta = 60^o$

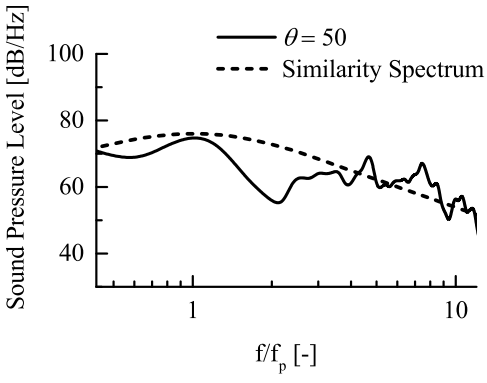

(c) $(x/D, r/D) = (9.23, 11)$; $\theta = 50^o$

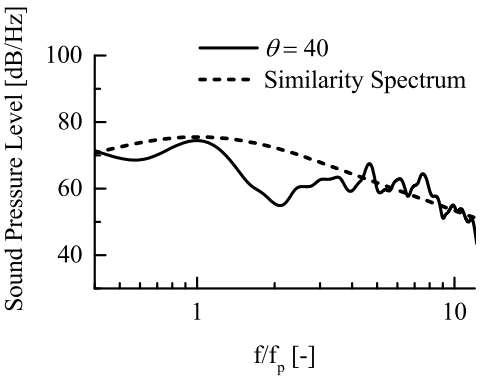

(d) $(x/D, r/D) = (13.11, 11)$; $\theta = 40^o$

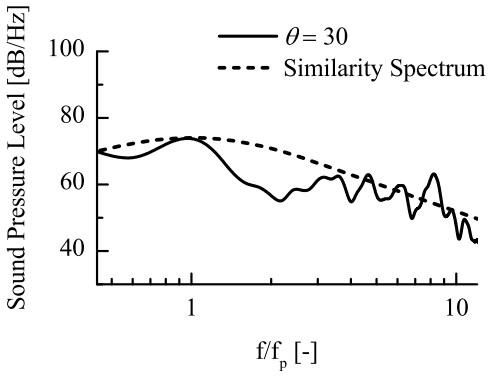

(e) $(x/D, r/D) = (19.05, 11)$; $\theta = 30^o$

Figure 3.14: Comparison between combustion noise similarity spectrum proposed by Tam et al. [52] and computed sound pressure level spectra of the spray flame, at the same positions as in Fig. 3.12 corresponding to different emission angles θ with respect to the flame axis.

parison with the computed sound pressure spectra. The abscissa in these plots represent the normalized frequency, where f is the spectral frequency and f_p is the frequency corresponding to the peak of the spectrum, known as peak frequency. The sound pressure spectra of combustion noise emitted by the open turbulent spray flame obtained from DNS, bear resemblance to the combustion noise similarity spectrum proposed by Tam et al. [52]. Moreover, shapes of the computed noise spectra are virtually similar to that of the suggested similarity spectrum of open flame combustion noise, for all emission angles. The peak frequency for the spray flame under investigation is approximately $f_p \approx 417$ Hz for all emission angles. And, the sound pressure levels at the spectral peaks are also nearly the same, irrespective of the emission angle. These combustion noise characteristics of the open turbulent spray flame are therefore, similar to those reported in the experimental findings of Tam et al. [52] for combustion noise measurements.

3.6 Conclusions

In this study, DNS was used to investigate the combustion noise generation from an open turbulent spray flame with Ethanol as the fuel. The DNS predictions for flow field statistical quantities like droplet velocities and corresponding fluctuations, and gas-phase excess temperature showed an overall good agreement with experimental data. The noise generated by the spray flame was found to be broadband. The turbulent spray flame exhibits combustion noise characteristics similar to those of turbulent premixed and non-premixed flames in terms of spectral content and directivity. Analysis of the noise directivity characteristics of the spray flame showed fairly similar spectral shapes and sound pressures at the low-frequencies, for various emission angles to the flame axis (corresponding to various stream-wise locations from the nozzle exit), suggesting dominance of the distributed monopole combustion noise sources arising from unsteady heat release rate fluctuations. However, suppression of sound pressure levels for the high-frequency noise emissions with increasing distance from the nozzle exit, corresponding to decreasing emission angle to the flame axis was observed. This weak directivity is attributed to the refraction effects arising from temperature-dependent gradients in the sound speed within the flame. Furthermore, the DNS computed sound pressure spectra of combustion noise from the open turbulent spray flame, were comparable to the similarity spectrum of open flame combustion noise regardless of the direction of emission.

References

[1] S. H. Stårner, J. D. Gounder, and A. R. Masri. Effects of turbulence and carrier fluid on simple, turbulent spray jet flames. *Combust. Flame*, 143:420–432, 2005.

[2] A. R. Masri and J. D. Gounder. Turbulent spray flames of acetone and ethanol approaching extinction. *Combust. Sci. Tech.*, 182(4-6):702–715, 2010.

[3] J. D. Gounder, A. Kourmatzis, and A. R. Masri. Turbulent piloted dilute spray flames: Flow fields and droplet dynamics. *Combust. Flame*, 159:3372–3397, 2012.

[4] S. Tachibana, K. Saito, T. Yamamoto, M. Makida, T. Kitano, and R. Kurose. Experimental and numerical investigation of thermo-acoustic instability in a liquid-fuel aero-engine combustor at elevated pressure: Validity of large-eddy simulation of spray combustion. *Combust. Flame*, 162(6):2621–2637, 2015.

[5] H. Moriai, R. Kurose, H. Watanabe, Y. Yano, F. Akamatsu, and S. Komori. Large-eddy simulation of turbulent spray combustion in a subscale aircraft jet engine combustor–predictions of NO and soot concentrations. *J. Eng. Gas Turbines Power*, 135(9):091503, 2013.

[6] M. Chrigui, A. R. Masri, A. Sadiki, and J. Janicka. Large eddy simulation of a polydisperse ethanol spray flame. *Flow Turbul. Combust.*, 90:813–832, 2013.

[7] S. Ukai, A. Kronenburg, and O. T. Stein. LES-CMC of a dilute acetone spray flame. *Proc. Combust. Inst.*, 34:1643–1650, 2013.

[8] W. P. Jones, A. J. Marquis, and D. Noh. Les of a methanol spray flame with a stochastic sub-grid model. *Proc. Combust. Inst.*, 35:1685–1691, 2015.

[9] A. Rittler, F. Proch, and A. M. Kempf. LES of the sydney piloted spray flame series with the PFGM/ATF approach and different sub-filter models. *Combust. Flame*, 162:1575–1598, 2015.

[10] T. Kitano, K. Kaneko, R. Kurose, and S. Komori. Large-eddy simulations of gas– and liquid–fueled combustion instabilities in back-step flows. *Combust. Flame*, 170:63–78, 2016.

[11] C. T. Crowe, M. P. Sharma, and D. E. Stock. The Particle-Source-In Cell (PSI-CELL) model for gas-droplet flows. *J. Fluids Eng.*, 99:325–332, 1977.

[12] J. Bellan and M. Summerfield. Theoretical examination of assumptions commonly used for the gas phase surrounding a burning droplet. *Combust. Flame*, 33:107–122, 1978.

[13] J. Bellan and K. Harstad. Analysis of the convective evaporation of nondilute clusters of drops. *Int. J. Heat Mass Transfer*, 30(1):125–136, 1987.

[14] R. S. Miller, K. Harstad, and J. Bellan. Evaluation of equilibrium and non-equilibrium evaporation models for many-droplet gas-liquid flow simulations. *Int. J. Multiphase Flow*, 24(6):1025–1055, 1998.

[15] R. S. Miller and J. Bellan. Direct numerical simulation of a confined three-dimensional gas mixing layer with one evaporating hydrocarbon-droplet laden stream. *J. Fluid Mech.*, 384:293–338, 1999.

[16] T. Kitano, J. Nishio, R. Kurose, and S. Komori. Effects of ambient pressure, gas temperature and combustion reaction on droplet evaporation. *Combust. Flame*, 161(2):551–564, 2014.

[17] T. Kitano, J. Nishio, R. Kurose, and S. Komori. Evaporation and combustion of multicomponent fuel droplets. *Fuel*, 136:219–225, 2014.

[18] M. Nakamura, F. Akamatsu, R. Kurose, and M. Katsuki. Combustion mechanism of liquid fuel spray in a gaseous flame. *Phys. Fluids*, 17(12):123301, 2005.

[19] R. Kurose, H. Makino, S. Komori, M. Nakamura, F. Akamatsu, and M. Katsuki. Effects of outflow from the surface of a sphere on drag, shear lift, and scalar diffusion. *Phys. Fluids*, 15(8):2338–2351, 2003.

[20] H. Watanabe, R. Kurose, S.-M. Hwang, and F. Akamatsu. Characteristics of flamelets in spray flames formed in a laminar counterflow. *Combust. Flame*, 148(4):234–248, 2007.

[21] C. K. Westbrook and F. L. Dryer. Simplified reaction mechanisms for the oxidation of hydrocarbon fuels in flames. *Combust. Sci. Tech.*, 27:31–43, 1981.

[22] A. P. Wandel, N. Chakraborty, and E. Mastorakos. Direct numerical simulations of turbulent flame expansion in fine sprays. *Proc. Combust. Inst.*, 32:2283–2290, 2009.

[23] D. H. Wacks, N. Chakraborty, and E. Mastorakos. Statistical analysis of turbulent flame-droplet interaction: A direct numerical simulation study. *Flow Turbul. Combust.*, 96:573–607, 2016.

[24] D. H. Wacks and N. Chakraborty. Flame structure and propagation in turbulent flame-droplet interaction: A Direct Numerical Simulation analysis. *Flow Turbul. Combust.*, 96:1053–1081, 2016.

[25] W. L. Grosshandler. RADCAL: A narrow-band model for radiation calculations in a combustion environment. NIST Technical Note 1402, 1993.

[26] R. S. Barlow, A. N. Karpetis, J. H. Frank, and J.-Y. Chen. Scalar profiles and NO formation in laminar opposed-flow partially premixed methane/air flames. *Combust. Flame*, 127:2102–2118, 2001.

[27] K. Luo, O. Desjardins, and H. Pitsch. DNS of droplet evaporation and combustion in a swirling combustor. In *Annual Research Briefs*. Center for Turbulence Research, NASA Ames/Stanford University, 2008.

[28] K. Luo, H. Pitsch, M. G. Pai, and O. Desjardins. Direct numerical simulations and analysis of three-dimensional n-heptane spray flames in a model swirl combustor. *Proc. Combust. Inst.*, 33:2143–2152, 2011.

[29] T. Kitano, R. Kurose, and S. Komori. Effects of internal pressure and inlet velocity disturbances of air and fuel droplets on spray combustion field. *J. Therm. Sci. Technol.*, 8(1):269–280, 2013.

[30] T. Kitano, T. Tsuji, R. Kurose, and S. Komori. Effect of pressure oscillations on flashback characteristics in a turbulent channel flow. *Energy Fuels*, 29(10):6815–6822, 2015.

[31] A. L. Pillai, M. Muto, and R. Kurose. Numerical investigation of effect of Reynolds number on noise from turbulent non-premixed hydrogen jet flames. In *Proc. ACGT2016*, Mumbai, India, 2016. Indian Institute of Technology Bombay.

[32] V. Moureau, C. Bérat, and H. Pitsch. An efficient semi-implicit compressible solver for large-eddy simulations. *J. Comput. Physics*, 226(2):1256–1270, 2007.

[33] G.-S. Jiang and C.-W. Shu. Efficient implementation of weighted ENO schemes. *J. Comput. Physics*, 126:202–228, 1996.

[34] R. J. Kee, D.-L. Graham, J. Warnatz, M. E. Coltrin, and J. A. Miller. A fortran computer code package for the evaluation of gas-phase, multicomponent transport properties. SANDIA Report No. SAND86-8246, Sandia National Laboratories, Albuquerque NM, Livermore CA, 1986.

[35] R. J. Kee, F. M. Rupley, and J. A. Miller. Chemkin-II: A FORTRAN chemical kinetics package for the analysis of gas-phase chemical kinetics. SANDIA Report No. SAND89-8009B, Sandia National Laboratories, Albuquerque NM, Livermore CA, 1989.

[36] M. Klein, A. Sadiki, and J. Janicka. A digital filter based generation of inflow data for spatially developing direct numerical or large eddy simulations. *J. Comput. Physics*, 186:652–665, 2003.

[37] A. M. Kempf, S. Wysocki, and M. Pettit. An efficient, parallel low-storage implementation of Klein' s turbulence generator for LES and DNS. *Comput. Fluids*, 60:58–60, 2012.

[38] C. Bogey and C. Bailly. Three-dimensional non-reflective boundary conditions for acoustic simulations: Far field formulation and validation test cases. *Acta. Acust. united Ac.*, 88:463–471, 2002.

[39] C. A. Kennedy and M. H. Carpenter. Several new numerical methods for compressible shear-layer simulations. *Appl. Numer. Math.*, 14:397–433, 1994.

[40] R. Piscoya, H. Brick, M. Ochmann, and P. Költzsch. Equivalent source method and boundary element method for calculating combustion noise. *Acta Acust. united Ac.*, 94(4):514–527, 2008.

[41] R. Barlow. editor, Proceedings of the TNF workshops, Sandia National Laboratories, 1996-2004, Livermore, CA. *available at www.ca.sandia.gov/TNF.*

[42] D. G. Pfuderer, A. A. Neuber, G. Früchtel, E. P. Hassel, and J. Janicka. Turbulence modulation in jet diffusion flames: Modeling and experiments. *Combust. Flame*, 106:301–317, 1996.

[43] F. Flemming, A. Sadiki, and J. Janicka. Investigation of combustion noise using a LES/CAA hybrid approach. *Proc. Combust. Inst.*, 31:3189–3196, 2007.

[44] T. J. B. Smith and J. K. Kilham. Noise generation by open turbulent flames. *J. Acoust. Soc. Am.*, 35:715–724, 1963.

[45] W. C. Strahle. Some results in combustion generated noise. *J. Sound Vib.*, 23:113–125, 1972.

[46] B. N. Shivashankara, W. C. Strahle, and J. C. Handley. Combustion noise radiation by open turbulent flames. *AIAA paper*, 1973-1025 (1973), 1973.

[47] S. Kotake and K. Takamoto. Combustion noise: Effects of the shape and size of burner nozzle. *J. Sound Vib.*, 112:345–354, 1987.

[48] K. K. Singh, S. H. Frankel, and J. P. Gore. Study of spectral noise emissions from standard turbulent nonpremixed flames. *AIAA Journal*, 42:931–936, 2004.

[49] M. Ihme and H. Pitsch. On the generation of direct combustion noise in turbulent non-premixed flames. *Int. J. Aeroacoust.*, 11:25–78, 2012.

[50] M. Ihme, H. Pitsch, and D. Bodony. Radiation of noise in turbulent non-premixed flames. *Proc. Combust. Inst.*, 32:1545–1553, 2009.

[51] M. Ihme, M. Kaltenbacher, and H. Pitsch. Numerical simulation of flow- and combustion-induced sound using a hybrid LES/CAA approach. 497–510. Proceedings of the Summer Program, Center for Turbulence Research, 2006.

[52] C. K. W. Tam, N. N. Pastouchenko, J. Mendoza, and D. Brown. Combustion noise of auxiliary power units. *AIAA paper*, 2005-2829 (2005), 2005.

[53] C. K. W. Tam, M. Golebiowski, and J. M. Seiner. On the two components of turbulent mixing noise from supersonic jets. *AIAA paper*, 96-1716 (1996), 1996.

Chapter 4

Prediction of combustion noise in turbulent spray and non-premixed flames using a hybrid DNS/APE-RF approach

4.1 Introduction

In this chapter, the acoustic field of combustion induced noise of an open turbulent spray flame and an open turbulent non-premixed flame have been predicted using a hybrid Computational Fluid Dynamics and Computational Aero-Acoustics (CFD/CAA) framework. In this two-step framework, the first step involves DNS of the reactive flow-field of a turbulent flame. The DNS is restricted to the source region only, which implies that the physical size of its computational domain is sufficiently large enough to capture the near-field of the turbulent flame, within which the sources exciting acoustic waves are expected to be present. The second step involves the CAA simulation in which, the system of Acoustic Perturbation Equations extended for Reacting Flows (APE-RF) [1, 2] is solved, and the acoustic wave propagation is captured all the way into the far-field. The dominant source term exciting acoustic waves, which is computed

in the DNS step is used as input data for solving the APE-RF system in the CAA step. The physical size of the computational domain of CAA simulation is much larger than that of the DNS, and has a coarser grid than that of the DNS. This application of separate computational techniques specifically tailored for each simulation, is made possible by the large disparity in the characteristic fluid dynamic and acoustic length scales. Because, for low Mach number reacting flows, the acoustic length scales are more than an order of magnitude larger than the fluid dynamic length scales. Hence, the hybrid approach is a computationally more efficient and much cheaper alternative to performing a compressible DNS of a turbulent flame, on a large computational domain that extends up to the acoustic far-field. The numerical approach used in this study is termed as the hybrid DNS/APE-RF approach.

The main objective of this work is to analyze the combustion noise characteristics of an open turbulent spray flame using a hybrid DNS/APE-RF approach. For this purpose, the source term appearing on the RHS of the pressure-density relation in the APE-RF system (that was originally formulated for premixed and non-premixed flames by Bui et al. [1, 2]), which dominates the excitation of acoustic waves has been reformulated for the spray flame, in order to incorporate the additional effect of density variations caused by fuel droplet evaporation. In this study, the hybrid DNS/APE-RF approach is first applied to a benchmark open turbulent non-premixed Hydrogen flame of the workshop for turbulent non-premixed flames (TNF-workshop) [3], called the H3 flame [4]. The results for its flow-field statistical quantities obtained from the DNS as well as the combustion noise results obtained from the CAA simulation, have been extensively validated against measurements. Based on this validation of the numerical framework, the hybrid DNS/APE-RF approach is used for simulating the two-phase reacting flow-field and the combustion generated acoustic field of an experimental open turbulent spray flame designated as EtF3 [5]. The DNS results of the spray flame are validated against measurements in terms of droplet velocity statistics and gas-phase temperatures. The combustion generated acoustic field of the open turbulent spray flame is predicted and characteristics of the radiated noise are investigated.

4.2 Direct Numerical Simulation

4.2.1 Governing equations

The governing equations for the conservation of mass, momentum, energy, and mass fraction of chemical species in case of the turbulent non-premixed Hydrogen flame H3 are detailed in Section 2.2.1 of Chapter 2. For the turbulent spray flame EtF3, the governing equations of the gas-phase (solved in an Eulerian framework) are described in Section 3.2.1 and the governing equations for the dispersed-phase (solved in a Lagrangian framework) are detailed in Section 3.2.2 of Chapter 3.

4.2.2 Reaction models

For the non-premixed Hydrogen flame H3, the combustion reaction of Hydrogen is described using a one-step global reaction model [6] as explained in Section 2.2.1.1 of Chapter 2, while for the spray flame EtF3, the combustion reaction of gaseous Ethanol is taken into account using a two-step global reaction mechanism [7] as described in Section 3.2.3 of Chapter 3.

4.3 Acoustic Perturbation Equations for Reacting Flows

Ewert and Schröder [8] formulated the homogeneous Acoustic Perturbation Equations (APE) system and simulated the trailing edge noise from an airfoil using the hybrid LES/APE approach [9]. Later on, Bui et al. [1, 2] extended the APE system to multicomponent reacting flows (APE-RF) to simulate combustion generated noise due to its ability to capture wave propagation in non-uniform mean flows, while preventing excitations of instabilities. The APE-RF system is expressed as

$$\frac{\partial \rho'}{\partial t} + \nabla \cdot (\rho' \overline{\boldsymbol{u}} + \overline{\rho} \boldsymbol{u'}) = q_{c,rf} \tag{4.1}$$

$$\frac{\partial \boldsymbol{u'}}{\partial t} + \nabla(\overline{\boldsymbol{u}} \cdot \boldsymbol{u'}) + \nabla\left(\frac{p'}{\overline{\rho}}\right) = \boldsymbol{q}_{m,rf} \tag{4.2}$$

$$\frac{\partial p'}{\partial t} - \overline{c}^2 \frac{\partial \rho'}{\partial t} = q_{e,rf} \tag{4.3}$$

In Eqs. (4.1) - (4.3) the density ρ, velocity $\boldsymbol{u}$ and pressure p have been decomposed into time averaged mean ($\overline{\rho}$, $\overline{\boldsymbol{u}}$ and $\overline{p}$, denoted by an overbar) and fluctuating (ρ', $\boldsymbol{u'}$ and p', denoted by a prime) parts as $\rho = \overline{\rho} + \rho'$, $\boldsymbol{u} = \overline{\boldsymbol{u}} + \boldsymbol{u'}$, and $p = \overline{p} + p'$. While, $\overline{c}$ is the mean speed of sound, and $q_{c,rf}$, $\boldsymbol{q}_{m,rf}$ and $q_{e,rf}$ are the acoustic source terms for the equations governing perturbation density, velocity and the pressure-density relation, respectively. These source terms are computed from the DNS and given by

$$q_{c,rf} = -\nabla \cdot (\rho' \boldsymbol{u'})' \tag{4.4}$$

$$\begin{aligned} \boldsymbol{q}_{m,rf} = {} & \nabla p \left(\frac{1}{\overline{\rho}} - \frac{1}{\rho}\right) - \frac{1}{\overline{\rho}} \left[\nabla \overline{p} + \left(\frac{\rho}{\overline{\rho}} c^2 - \overline{c}^2\right) \nabla \overline{\rho}\right] \\ & + \left[\frac{\nabla \cdot \boldsymbol{\tau}}{\rho} + \sum_n Y_k f_k - (\overline{\boldsymbol{u}} \cdot \nabla)\overline{\boldsymbol{u}} - (\boldsymbol{u'} \cdot \nabla)\boldsymbol{u'} - (\boldsymbol{\omega'} \times \overline{\boldsymbol{u}}) - (\overline{\boldsymbol{\omega}} \times \boldsymbol{u'})\right] \end{aligned} \tag{4.5}$$

$$\begin{aligned} q_{e,rf} = -\overline{c}^2 \Bigg[& \left(\frac{\overline{\rho}}{\rho} + \frac{p - \overline{p}}{\rho \overline{c}^2}\right) \frac{D\rho}{Dt} - \frac{1}{\overline{c}^2} \frac{Dp}{Dt} - \nabla \cdot (\boldsymbol{u} \rho_e) \\ & \underbrace{- \frac{\gamma - 1}{\gamma} \boldsymbol{u} \cdot \nabla \overline{\rho} - \frac{p}{\overline{c}^2} \boldsymbol{u} \cdot \left(\frac{\nabla \overline{p}}{\overline{p}} - \frac{\nabla \overline{\rho}}{\overline{\rho}}\right)}_{\chi} \Bigg] \end{aligned} \tag{4.6}$$

In Eq. (4.5), which defines the source term $\boldsymbol{q}_{m,rf}$ of the perturbation velocity Eq. (4.2), Y_k and f_k are the mass fraction of species k and the volume force acting on species k, respectively, while $\boldsymbol{\omega'} = \nabla \times \boldsymbol{u'}$ and $\overline{\boldsymbol{\omega}} = \nabla \times \overline{\boldsymbol{u}}$.

In Eq. (4.6) for the source term $q_{e,rf}$ of the pressure-density relation in Eq. (4.3), γ is the ratio of specific heats, ρ_e is the excess density [10] defined as

$$\rho_e = (\rho - \overline{\rho}) - \frac{p - \overline{p}}{\overline{c}^2} \tag{4.7}$$

The term $q_{e,rf}$ contains various source mechanisms that excite acoustic waves in combustion generated noise. The first term of $q_{e,rf}$ i.e., the one with substantial time derivative

of density $D\rho/Dt$ implicitly takes into account the effects of heat release rate per unit volume, volumetric expansion due to non-isomolar combustion, species diffusion, heat diffusion as well as viscous effects. Complete description of these source mechanisms is provided in [1, 2].

Apart from the substantial time derivative of density term $D\rho/Dt$ which includes the dominant source mechanism of combustion noise (i.e. the effect of unsteady heat release rate), there are additional source mechanisms in Eq. (4.6) that excite acoustic waves. Such as, χ which accounts for the effects of non-uniform mean flow, Dp/Dt term which describes excitation of acoustic waves due to combustion at non-constant pressure, and the $\nabla \cdot (\boldsymbol{u}\rho_e)$ term which describes the effect of acceleration of density inhomogeneties on the radiated acoustic field in regions where the density and speed of sound differ from ambient values [11]. The APE-RF system was derived from the conservation equations of mass, momentum and energy for multicomponent reacting flows and the detailed derivation is available in [11].

During the initial simulation runs for both the spray and non-premixed flames, it was found that $q_{c,rf}$ and $\boldsymbol{q}_{m,rf}$ are approximately four and two orders of magnitude smaller than $q_{e,rf}$, respectively. Now, the source term $\boldsymbol{q}_{m,rf}$ would be the dominant acoustic source in case of non-reacting flows as pointed out by Ewert and Schröder [8, 9, 12]. In their investigations on vortex sound problems in non-reacting flows [8, 9], the quantity $(\boldsymbol{\omega'} \times \overline{\boldsymbol{u}} + \overline{\boldsymbol{\omega}} \times \boldsymbol{u'})$ appearing in Eq. (4.5) which represents a perturbed form of the Lamb vector $\boldsymbol{L} = (\boldsymbol{\omega} \times \boldsymbol{u})'$, was found to be the major acoustic source. However, when low Mach number reacting flows (such as both the flames in this investigations) are considered, the effect of chemical reactions and hence, unsteady heat release dominates over vortex generated noise [1, 11, 13–16]. Therefore, the assumption that $q_{c,rf}$ and $\boldsymbol{q}_{m,rf}$ are negligible in comparison to $q_{e,rf}$ is valid. The expression for source term $q_{e,rf}$ on the RHS of pressure-density relation Eq. (4.3) is slightly different for a two-phase reacting

flow like the spray flame, and is given by

$$q_{e,rf} = -\overline{c}^2 \left[\left(\frac{\overline{\rho}}{\rho} + \frac{p - \overline{p}}{\rho \overline{c}^2} \right) \frac{D\rho}{Dt} - \frac{1}{\overline{c}^2} \frac{Dp}{Dt} - \nabla \cdot (\boldsymbol{u} \rho_e) - \frac{\gamma - 1}{\gamma} \boldsymbol{u} \cdot \nabla \overline{\rho} \right.$$
$$\left. - \frac{p}{\overline{c}^2} \boldsymbol{u} \cdot \left(\frac{\nabla \overline{p}}{\overline{p}} - \frac{\nabla \overline{\rho}}{\overline{\rho}} \right) + \underbrace{\frac{\rho_e}{\rho} S_\rho} \right] \tag{4.8}$$

with the additional term $(\rho_e/\rho)S_\rho$ (in underbrace) which accounts for the contribution of evaporation source term S_ρ appearing in Eq. (3.1). $q_{e,rf}$ is evaluated using the variables that are obtained from the solution of DNS. As mentioned previously, the substantial time rate of change of density term in $q_{e,rf}$ implicitly takes into account the dominant combustion noise mechanism i.e. the unsteady heat release rate along with additional source mechanisms, and for the spray combustion case the effect of energy exchange between gas-phase and dispersed-phase, i.e. the contribution of $S_{\rho h}$ term in Eq. (3.3) is also included in the substantial time derivative of density. This is because, the $D\rho/Dt$ term can be expressed using the energy equation for reacting flows [11, 17]. Derivation of the expression for $q_{e,rf}$ in Eq. (4.8) for two-phase reacting flows is described later.

In the simulations conducted by Bui et al. [1, 2] for combustion noise in open turbulent non-premixed flames, the source terms $q_{c,rf}$ and $\boldsymbol{q}_{m,rf}$ in Eqs. (4.1) and (4.2), respectively were neglected, and simplified formulations of the source term $q_{e,rf}$ were used for solving the APE-RF system. One of the reasons for this is that, it is quite cumbersome and computationally expensive to compute all the acoustic source mechanisms in the APE-RF system. The simplified formulations of $q_{e,rf}$ retained the major source mechanism i.e., the $D\rho/Dt$ term which contains the unsteady heat release rate effect. And it was found that this simplified formulation of $q_{e,rf}$ was sufficient to obtain good predictions of the combustion generated acoustic fields as the impact of neglected terms on the acoustic fields was insignificant.

However, in this study the full expressions of $q_{e,rf}$ as given in Eqs. (4.6) and (4.8) for the non-premixed and spray flames, respectively are employed. This is necessary because, unlike the LES of Bui et al. [1] which was performed using an incompressible code, the DNS of the flames in this investigation are performed using a compressible

solver. So, if $q_{e,rf}$ is evaluated using input data from a compressible CFD simulation, it is imperative that the full expression of $q_{e,rf}$ be used. Otherwise, using the simplified version of $q_{e,rf}$ can lead to the generation spurious acoustic-acoustic excitations [18] in the CAA simulation. A general proof justifying the use of the complete mathematical expression for the source term $q_{e,rf}$ (when it is evaluated from the solution of a compressible CFD simulation) to avoid unphysical acoustic-acoustic excitations in the CAA solution is provided later. It is worth mentioning that in case of the spray flame EtF3, for the source term $q_{e,rf}$ which is computed in the DNS step using the full expression as given by Eq. (4.8), the term $(\rho_e/\rho)S_\rho$ which incorporates the effect of density variations caused by fuel droplet evaporation, is approximately two orders of magnitude smaller than the dominant acoustic source mechanism represented by the substantial time derivative of density term $\left(\frac{\overline{\rho}}{\rho} + \frac{p-\overline{p}}{\rho\overline{c}^2}\right)\frac{D\rho}{Dt}$.

4.3.1 Derivation of source term $q_{e,rf}$ for two-phase reacting flows

The derivation for source term $q_{e,rf}$ in the pressure-density relation of the two-phase reacting flow (spray flame case) is now presented. Starting with the definition of excess density ρ_e as introduced by Crighton et al. [10]

$$\rho_e = (\rho - \overline{\rho}) - \frac{p - \overline{p}}{\overline{c}^2} \tag{4.9}$$

Taking the total time derivative of ρ_e

$$\begin{aligned} \frac{D\rho_e}{Dt} &= \frac{\partial \rho_e}{\partial t} + \boldsymbol{u} \cdot \nabla \rho_e \\ &= \frac{\partial \rho_e}{\partial t} + \nabla \cdot (\boldsymbol{u}\rho_e) - \rho_e \nabla \cdot \boldsymbol{u} \end{aligned} \tag{4.10}$$

The continuity equation (3.1) can be rewritten as

$$\frac{D\rho}{Dt} + \rho \nabla \cdot \boldsymbol{u} = S_\rho \tag{4.11}$$

Substituting for the divergence of velocity field using the above equation

$$\frac{D\rho_e}{Dt} = \frac{\partial \rho_e}{\partial t} + \nabla \cdot (\boldsymbol{u}\rho_e) - \frac{\rho_e}{\rho}\left(S_\rho - \frac{D\rho}{Dt}\right) \tag{4.12}$$

$$\begin{aligned}\frac{\partial \rho_e}{\partial t} &= \frac{D\rho_e}{Dt} - \nabla\cdot(\boldsymbol{u}\rho_e) + \frac{\rho_e}{\rho}\left(S_\rho - \frac{D\rho}{Dt}\right) \\ &= \frac{D\rho_e}{Dt} - \nabla\cdot(\boldsymbol{u}\rho_e) - \frac{\rho_e}{\rho}\frac{D\rho}{Dt} + \frac{\rho_e}{\rho}S_\rho\end{aligned} \tag{4.13}$$

Substituting the definition of ρ_e in the above equation

$$\begin{aligned}\frac{\partial \rho_e}{\partial t} &= \frac{D}{Dt}(\rho - \overline{\rho}) - \frac{D}{Dt}\left(\frac{p-\overline{p}}{\overline{c}^2}\right) - \nabla\cdot(\boldsymbol{u}\rho_e) + \frac{\rho_e}{\rho}S_\rho \\ &- \frac{1}{\rho}\left(\rho - \overline{\rho} - \frac{p-\overline{p}}{\overline{c}^2}\right)\frac{D\rho}{Dt} \\ &= \left(\frac{\overline{\rho}}{\rho} + \frac{p-\overline{p}}{\rho\overline{c}^2}\right)\frac{D\rho}{Dt} - \frac{D\overline{\rho}}{Dt} - \nabla\cdot(\boldsymbol{u}\rho_e) - \frac{D}{Dt}\left(\frac{p-\overline{p}}{\overline{c}^2}\right) + \frac{\rho_e}{\rho}S_\rho\end{aligned} \tag{4.14}$$

In the above equation, local time derivatives of mean quantities will vanish (e.g. $\partial\overline{\rho}/\partial t = 0$), hence by expanding the $(D\overline{\rho}/Dt)$ term we get

$$\frac{\partial \rho_e}{\partial t} = \left(\frac{\overline{\rho}}{\rho} + \frac{p-\overline{p}}{\rho\overline{c}^2}\right)\frac{D\rho}{Dt} - \boldsymbol{u}\cdot\nabla\overline{\rho} - \nabla\cdot(\boldsymbol{u}\rho_e) - \frac{D}{Dt}\left(\frac{p-\overline{p}}{\overline{c}^2}\right) + \frac{\rho_e}{\rho}S_\rho \tag{4.15}$$

Therefore, using Eq. (4.15) the pressure-density relation of the APE-RF system for two-phase reacting flows reads

$$\frac{\partial p'}{\partial t} - \overline{c}^2\frac{\partial \rho'}{\partial t} = -\overline{c}^2\frac{\partial \rho_e}{\partial t} \tag{4.16}$$

$$\begin{aligned}\frac{\partial p'}{\partial t} - \overline{c}^2\frac{\partial \rho'}{\partial t} = -\overline{c}^2\Bigg[&\left(\frac{\overline{\rho}}{\rho} + \frac{p-\overline{p}}{\rho\overline{c}^2}\right)\frac{D\rho}{Dt} - \boldsymbol{u}\cdot\nabla\overline{\rho} - \nabla\cdot(\boldsymbol{u}\rho_e) \\ &- \frac{D}{Dt}\left(\frac{p-\overline{p}}{\overline{c}^2}\right) + \frac{\rho_e}{\rho}S_\rho\Bigg]\end{aligned} \tag{4.17}$$

With the source term $q_{e,rf}$ for two-phase reacting flow as

$$\begin{aligned}q_{e,rf} = -\overline{c}^2\Bigg[&\left(\frac{\overline{\rho}}{\rho} + \frac{p-\overline{p}}{\rho\overline{c}^2}\right)\frac{D\rho}{Dt} - \boldsymbol{u}\cdot\nabla\overline{\rho} - \nabla\cdot(\boldsymbol{u}\rho_e) \\ &- \frac{D}{Dt}\left(\frac{p-\overline{p}}{\overline{c}^2}\right) + \frac{\rho_e}{\rho}S_\rho\Bigg]\end{aligned} \tag{4.18}$$

Upon expanding the penultimate term on the right-hand side of the above equation, the complete formulation of $q_{e,rf}$ similar to the one derived by Bui et al. [11] can be obtained

$$\begin{aligned} q_{e,rf} &= -\overline{c}^2 \left[\left(\frac{\overline{\rho}}{\rho} + \frac{p-\overline{p}}{\rho \overline{c}^2} \right) \frac{D\rho}{Dt} - \boldsymbol{u} \cdot \nabla \overline{\rho} - \nabla \cdot (\boldsymbol{u} \rho_e) \right. \\ &\quad \left. - \frac{D}{Dt} \left(\frac{p}{\overline{c}^2} \right) + \frac{D}{Dt} \left(\frac{\overline{p}}{\overline{c}^2} \right) + \frac{\rho_e}{\rho} S_\rho \right] \\ &= -\overline{c}^2 \left[\left(\frac{\overline{\rho}}{\rho} + \frac{p-\overline{p}}{\rho \overline{c}^2} \right) \frac{D\rho}{Dt} - \boldsymbol{u} \cdot \nabla \overline{\rho} - \nabla \cdot (\boldsymbol{u} \rho_e) \right. \\ &\quad \left. - \frac{1}{\overline{c}^2} \frac{Dp}{Dt} - \frac{p}{\overline{c}^2} \boldsymbol{u} \cdot \left(\frac{\nabla \overline{p}}{\overline{p}} - \frac{\nabla \overline{\rho}}{\overline{\rho}} \right) + \frac{D}{Dt} \left(\frac{\overline{p}}{\gamma \overline{p}/\overline{\rho}} \right) + \frac{\rho_e}{\rho} S_\rho \right] \end{aligned} \tag{4.19}$$

Since, the local time derivatives of time averaged mean variables are zero

$$\begin{aligned} q_{e,rf} = -\overline{c}^2 \left[\left(\frac{\overline{\rho}}{\rho} + \frac{p-\overline{p}}{\rho \overline{c}^2} \right) \frac{D\rho}{Dt} - \nabla \cdot (\boldsymbol{u} \rho_e) - \boldsymbol{u} \cdot \nabla \overline{\rho} - \frac{1}{\overline{c}^2} \frac{Dp}{Dt} \right. \\ \left. - \frac{p}{\overline{c}^2} \boldsymbol{u} \cdot \left(\frac{\nabla \overline{p}}{\overline{p}} - \frac{\nabla \overline{\rho}}{\overline{\rho}} \right) + \frac{1}{\gamma} \boldsymbol{u} \cdot \nabla \overline{\rho} + \frac{\rho_e}{\rho} S_\rho \right] \end{aligned} \tag{4.20}$$

Therefore, the complete expression of source term $q_{e,rf}$ for two-phase reacting flow is

$$\begin{aligned} q_{e,rf} = -\overline{c}^2 \left[\left(\frac{\overline{\rho}}{\rho} + \frac{p-\overline{p}}{\rho \overline{c}^2} \right) \frac{D\rho}{Dt} - \nabla \cdot (\boldsymbol{u} \rho_e) - \frac{\gamma - 1}{\gamma} \boldsymbol{u} \cdot \nabla \overline{\rho} - \frac{1}{\overline{c}^2} \frac{Dp}{Dt} \right. \\ \left. - \frac{p}{\overline{c}^2} \boldsymbol{u} \cdot \left(\frac{\nabla \overline{p}}{\overline{p}} - \frac{\nabla \overline{\rho}}{\overline{\rho}} \right) + \frac{\rho_e}{\rho} S_\rho \right] \end{aligned} \tag{4.21}$$

4.3.2 Use of complete expression of $q_{e,rf}$ to avoid spurious excitations

Proof that when the source term $q_{e,rf}$ is evaluated from compressible CFD (DNS or LES) data using the complete expression for $q_{e,rf}$ in Eq. (4.6) or Eq. (4.18), the source mechanisms are governed solely by hydrodynamic fluctuations, is provided here. This way, acoustic waves are excited only by hydrodynamic fluctuations in the source term $q_{e,rf}$ and non-physical acoustic-acoustic excitations are avoided in the CAA simulations. Starting with the expression for $q_{e,rf}$ from Eq. (4.18)

$$\begin{aligned} q_{e,rf} = -\overline{c}^2 \left[\left(\frac{\overline{\rho}}{\rho} + \frac{p-\overline{p}}{\rho \overline{c}^2} \right) \frac{D\rho}{Dt} - \nabla \cdot (\boldsymbol{u} \rho_e) - \boldsymbol{u} \cdot \nabla \overline{\rho} \right. \\ \left. - \frac{D}{Dt} \left(\frac{p-\overline{p}}{\overline{c}^2} \right) + \frac{\rho_e}{\rho} S_\rho \right] \end{aligned} \tag{4.22}$$

Using the definition of excess density ρ_e in Eq. (4.7) and substituting in Eq. (4.22), we have

$$\begin{aligned} q_{e,rf} = -\overline{c}^2 \Bigg[& \left(\frac{\overline{\rho}}{\rho} + \frac{p-\overline{p}}{\rho \overline{c}^2} \right) \frac{D\rho}{Dt} - \nabla \cdot \left(\boldsymbol{u}(\rho - \overline{\rho}) - \boldsymbol{u} \left(\frac{p-\overline{p}}{\overline{c}^2} \right) \right) - \boldsymbol{u} \cdot \nabla \overline{\rho} \\ & - \frac{D}{Dt} \left(\frac{p-\overline{p}}{\overline{c}^2} \right) + \frac{\rho_e}{\rho} S_\rho \Bigg] \end{aligned} \tag{4.23}$$

$$\begin{aligned} q_{e,rf} &= -\overline{c}^2 \Bigg[\left(\frac{\overline{\rho}}{\rho} + \frac{p-\overline{p}}{\rho \overline{c}^2} \right) \frac{D\rho}{Dt} - \nabla \cdot (\boldsymbol{u}\rho) + \nabla \cdot (\boldsymbol{u}\overline{\rho}) + \nabla \cdot \left(\boldsymbol{u} \left(\frac{p-\overline{p}}{\overline{c}^2} \right) \right) \\ & - \boldsymbol{u} \cdot \nabla \overline{\rho} - \frac{D}{Dt} \left(\frac{p-\overline{p}}{\overline{c}^2} \right) + \frac{\rho_e}{\rho} S_\rho \Bigg] \\ &= -\overline{c}^2 \Bigg[\left(\frac{\overline{\rho}}{\rho} + \frac{p-\overline{p}}{\rho \overline{c}^2} \right) \frac{D\rho}{Dt} - \nabla \cdot (\boldsymbol{u}\rho) + \overline{\rho} \nabla \cdot \boldsymbol{u} + \boldsymbol{u} \cdot \nabla \overline{\rho} - \boldsymbol{u} \cdot \nabla \overline{\rho} \\ & + \nabla \cdot \left(\boldsymbol{u} \left(\frac{p-\overline{p}}{\overline{c}^2} \right) \right) - \frac{D}{Dt} \left(\frac{p-\overline{p}}{\overline{c}^2} \right) + \frac{\rho_e}{\rho} S_\rho \Bigg] \end{aligned} \tag{4.24}$$

Substituting for the divergence of velocity field using the continuity equation (4.11) we have

$$\begin{aligned} q_{e,rf} &= -\overline{c}^2 \Bigg[\left(\frac{\overline{\rho}}{\rho} + \frac{p-\overline{p}}{\rho \overline{c}^2} \right) \frac{D\rho}{Dt} - \nabla \cdot (\boldsymbol{u}\rho) + \frac{\overline{\rho}}{\rho} S_\rho - \frac{\overline{\rho}}{\rho} \frac{D\rho}{Dt} + \left(\frac{p-\overline{p}}{\overline{c}^2} \right) \nabla \cdot \boldsymbol{u} \\ & + \boldsymbol{u} \cdot \nabla \left(\frac{p-\overline{p}}{\overline{c}^2} \right) - \frac{\partial}{\partial t} \left(\frac{p-\overline{p}}{\overline{c}^2} \right) - \boldsymbol{u} \cdot \nabla \left(\frac{p-\overline{p}}{\overline{c}^2} \right) + \frac{\rho_e}{\rho} S_\rho \Bigg] \\ &= -\overline{c}^2 \Bigg[\left(\frac{p-\overline{p}}{\rho \overline{c}^2} \right) \frac{D\rho}{Dt} - \nabla \cdot (\boldsymbol{u}\rho) + \frac{\overline{\rho}}{\rho} S_\rho + \left(\frac{p-\overline{p}}{\overline{c}^2} \right) \nabla \cdot \boldsymbol{u} \\ & - \frac{\partial}{\partial t} \left(\frac{p-\overline{p}}{\overline{c}^2} \right) + \frac{\rho_e}{\rho} S_\rho \Bigg] \end{aligned} \tag{4.25}$$

Using the definition of ρ_e from Eq. (4.7), and substituting for $\nabla \cdot (\boldsymbol{u}\rho)$ using continuity equation (3.1), and for $\nabla \cdot \boldsymbol{u}$ using Eq. (4.11)

$$\begin{aligned} q_{e,rf} = -\overline{c}^2 \Bigg[& \left(\frac{p-\overline{p}}{\rho \overline{c}^2} \right) \frac{D\rho}{Dt} + \frac{\partial \rho}{\partial t} - S_\rho + \frac{\overline{\rho}}{\rho} S_\rho + \left(\frac{p-\overline{p}}{\overline{c}^2} \right) \left(\frac{S_\rho}{\rho} - \frac{1}{\rho} \frac{D\rho}{Dt} \right) \\ & - \frac{1}{\overline{c}^2} \frac{\partial p}{\partial t} + \frac{1}{\rho} \left(\rho - \overline{\rho} - \frac{p-\overline{p}}{\overline{c}^2} \right) S_\rho \Bigg] \end{aligned} \tag{4.26}$$

In the above equation, all terms but the $\partial\rho/\partial t$ and $\partial p/\partial t$ terms will cancel out each other and the expression for $q_{e,rf}$ simplifies to

$$q_{e,rf} = -\overline{c}^2 \left[\frac{\partial \rho}{\partial t} - \frac{1}{\overline{c}^2} \frac{\partial p}{\partial t} \right] \tag{4.27}$$

Now, assuming that the flow variables ρ, $\boldsymbol{u}$ and p can be uniquely decomposed into time averaged mean, fluctuating hydrodynamic (ρ^h, $\boldsymbol{u}^h$ and p^h) and fluctuating acoustic (ρ^a, $\boldsymbol{u}^a$ and p^a) components as

$$\begin{aligned} \rho &= \overline{\rho} + \rho^h + \rho^a \\ \boldsymbol{u} &= \overline{\boldsymbol{u}} + \boldsymbol{u}^h + \boldsymbol{u}^a \\ p &= \overline{p} + p^h + p^a \end{aligned} \tag{4.28}$$

Substituting the above decomposition for ρ and p in Eq. (4.27)

$$\begin{aligned} q_{e,rf} &= -\overline{c}^2 \left[\frac{\partial(\rho^h + \rho^a)}{\partial t} - \frac{1}{\overline{c}^2} \frac{\partial(p^h + p^a)}{\partial t} \right] \\ &= \frac{\partial p^h}{\partial t} - \overline{c}^2 \frac{\partial \rho^h}{\partial t} + \underbrace{\left(\frac{\partial p^a}{\partial t} - \overline{c}^2 \frac{\partial \rho^a}{\partial t} \right)}_{=0} \end{aligned} \tag{4.29}$$

The last two terms on the right-hand side of the above equation nullify each other since, acoustic waves are isentropic in nature. This proves that when the source term $q_{e,rf}$ is evaluated with quantities obtained from the solution of a compressible DNS/LES, its complete expression as given by Eq. (4.18) or Eq. (4.21) must be used. This is necessary in order to ensure that the entropy fluctuations are governed solely by the hydrodynamic fluctuations of the CFD data, while the acoustic components nullify each other, thereby preventing spurious acoustic-acoustic excitations in the solution of the APE-RF system.

4.4 Computational Setup

4.4.1 Turbulent non-premixed flame (H3)

The turbulent non-premixed flame simulated in this study is a benchmark flame of the workshop for turbulent non-premixed flames [3] which was investigated in an experiment [4] with the designation H3. The burner configuration for this experiment consists of a 35 cm long circular stainless steel tube of diameter $D_{H3} = 8$ mm with a thinned rim at the exit. Through this tube a mixture Hydrogen and Nitrogen gas issues out into a low velocity laminar coflow of dry air. The DNS of H3 flame is performed on

Table 4.1: Parameters of turbulent non-premixed flame (H3).

Flame designation	H3
Fuel (Vol %)	H_2/N_2 : 50/50
Jet diameter, D_{H3} [mm]	8
Bulk jet velocity, U_{jet} [m/s]	34.8
Coflow velocity, U_{coflow} [m/s]	0.2
Jet Reynolds number, Re [–]	10000
Eckert number, Ec [–]	9.6×10^{-4}
Jet Mach number, $M = U_{jet}/c_\infty$ [–]	0.1

a non-uniform staggered Cartesian grid consisting of $1080 \times 400 \times 400$ grid points (a total of 172.8 million points) in the x-, y- and z- directions, respectively. The minimum grid spacing used is $\Delta x = \Delta y = \Delta z = 80\mu$m. The computational domain has physical size of $106D_{H3} \times 59D_{H3} \times 59D_{H3}$ in the x-, y- and z- directions, respectively. H3 flame parameters are summarized in Table 4.1, here the jet exit Mach number is defined with respect to speed of sound in ambient air c_∞. A schematic of the computational domain used for the DNS of the non-premixed Hydrogen flame H3 is illustrated in Fig. 4.1(a), showing the domain size and configuration of the burner's exit used as inflow boundary conditions in the DNS.

4.4.2 Turbulent spray flame (EtF3)

The open turbulent Ethanol spray flame examined in this study is designated as EtF3, and belongs to the series of Ethanol spray flames which were experimentally investigated at the University of Sydney by Gounder et al. [5], using a laboratory scale piloted spray burner. The burner configuration for this flame consists of a central jet nozzle through which fuel spray and carrier air issue out. The central jet nozzle is surrounded by a coaxial pilot annulus and an outer stream of primary co-flowing air, and the entire co-flow/burner assembly is mounted in a vertical wind tunnel that supplies a secondary

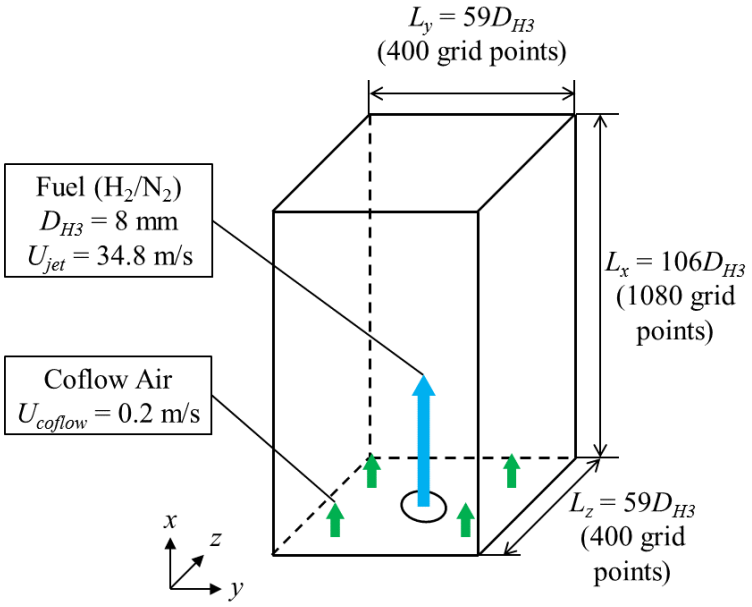

(a)

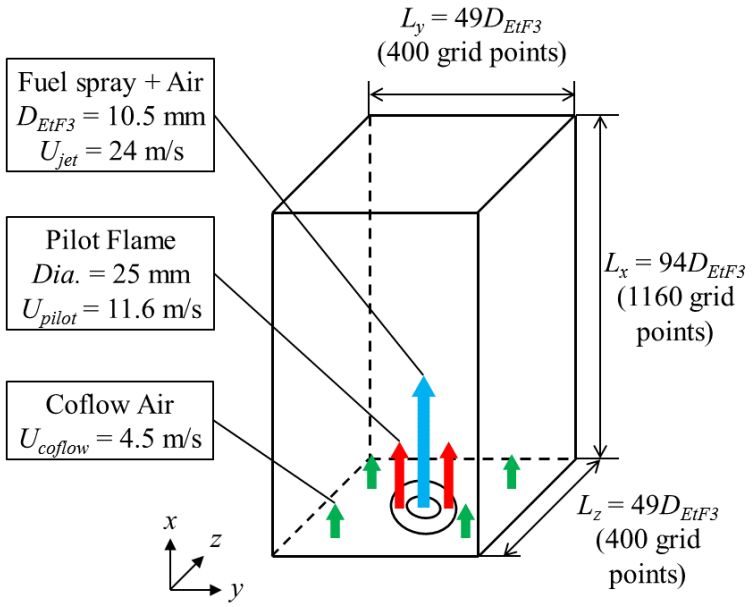

(b)

Figure 4.1: Schematics of the computational domains used for the DNS of (a) turbulent non-premixed Hydrogen flame H3 and (b) turbulent spray flame EtF3.

co-flow of air at the same velocity as the primary air co-flow [5]. The burner and primary co-flow's exit plane is situated 59 mm downstream of the exit plane of the wind tunnel. Ethanol spray flame's parameters measured at the burner exit for the central jet nozzle are listed in Table 4.2, while those for the annular pilot flame are listed in Table 4.3. At the burner exit, the pilot consists of fully-burned product of the stoichiometric mixture of 5.08% Acetylene (C_2H_2), 10.17% Hydrogen (H_2) and 84.75% air by volume, with an adiabatic flame temperature of 2493 K. This implies that pilot flame solely consists of the chemical species CO_2, H_2O and N_2 at the burner exit, whose respective mass fractions have been calculated a priori and listed in Table 4.3. The pilot flame supplies the heat for evaporation of the liquid fuel droplets, ignites the vaporized Ethanol and stabilizes the main spray flame. The spray was generated using an ultrasonic nebulizer situated inside the burner about 215 mm upstream of the jet exit plane in the experiment. Among the polydisperse droplets formed by the ultrasonic nebulizer inside the central nozzle tube, some evaporate prior to reaching the nozzle exit and that is why the measured liquid flow rate at the nozzle exit is smaller than the actual liquid fuel injection rate (see Table 4.2). The EtF3 spray flame burns in the partially premixed combustion regime, and more description on the burner setup is available in [5].

A schematic of the computational domain used for the DNS of the spray flame EtF3 is illustrated in Fig. 4.1(b) showing the domain size and configuration of the piloted spray burner's exit used as inflow boundary conditions. The DNS is performed on a staggered Cartesian grid consisting of 1160×400×400 grid points (a total of 185.6 million points) in the x-, y- and z-directions, respectively. The domain size is approximately $94D_{EtF3}\times49D_{EtF3}\times49D_{EtF3}$ in the x-, y- and z-directions, respectively. Fuel droplets are injected randomly in a polydisperse fashion from the central jet nozzle exit plane, with the maximum droplet size used in the DNS being 80 μm. Fuel droplet size distribution produced by the ultrasonic nebulizer in the experiment follows an approximate log-normal Probability Density Function (PDF) and hence, the best fit log-normal PDF curve to the experimental droplet size distribution data as depicted in Fig. 3.2, is used in the present DNS. In DNS of spray combustion, the grid spacing should be

Table 4.2: Flow parameters of the central jet of spray flame at burner exit.

Flame designation	EtF3
Fuel	Ethanol
Jet diameter, D_{EtF3} [mm]	10.5
Bulk jet velocity, U_{jet} [m/s]	24
Bulk velocity co-flow stream, U_{coflow} [m/s]	4.5
Carrier air mass flow rate [g/min]	150
Liquid fuel injection rate [g/min]	45
Measured liquid flow at exit [g/min]	30.7
Vapour fuel flow rate at exit [g/min]	14.3
Jet Reynolds number, Re [–]	19,700
Eckert number, Ec [–]	3.7×10^{-4}
Jet Mach number, M $= U_{jet}/C_{\infty}$ [–]	0.07
Equivalence ratio at jet exit, ϕ_{exit} [–]	0.85
Initial droplet & ambient temperature [K]	293.15

Table 4.3: Parameters of annular pilot at burner exit.

Fuel	Acetylene (C_2H_2) + Hydrogen (H_2) + Air
Pilot diameter [mm]	25
Bulk velocity pilot (burned), U_{pilot} [m/s]	11.6
Pilot temperature [K]	2493
Pilot composition ($Y_{CO_2} : Y_{H_2O} : Y_{N_2}$)	(0.1722 : 0.10575 : 0.722)

capable of resolving the Kolmogorov length scales and the flame reaction zone thickness. But, at the same time, due to the two-way coupling strategy between the gas and dispersed phases using the PSI-Cell approach [19], the grid spacing must ideally be 10 times larger than the droplet size in order to accurately capture the droplet evaporation dynamics [20, 21]. However, a two-step global chemistry is used as the reaction model in this study, which requires much less spatial resolution in comparison to detailed chemistry, since the thin reaction layers do not need to be resolved. Hence, a minimum grid spacing of $\Delta x = \Delta y = \Delta z = 150\mu$m is used in this study. The mesh is non-uniform, but it is fine in the core region of the jet flame.

4.5 Numerical Procedures

4.5.1 Numerical procedure for DNS

The flow-fields of the flames are simulated by performing DNS using the in-house hybrid CFD/CAA code called FK^3-CAA, which is a new extension of the previous in-house thermal flow analysis code FK^3 [22–26]. The CFD solver of this code, employs a pressure-based semi-implicit solver for compressible flows [27], whose algorithm consists of a fractional-step method. The spatial derivatives of the convective terms in the momentum equation are approximated using a 6^{th} order accurate central difference scheme, while the convective terms in the governing equations of the scalar quantities are evaluated using the WENO (Weighted Essentially Non-Oscillatory) scheme [28]. The spatial derivatives of the stress tensor terms are evaluated using a 4^{th} order central difference scheme and those of the diffusive terms are discretized by a 2^{nd} order central difference scheme. The time integration of the convective terms is performed using a 3^{rd} order explicit TVD Runge-Kutta method. Additionally, all the thermodynamic properties and transport coefficients taking temperature dependence into consideration are obtained from CHEMKIN [29, 30].

4.5.1.1 Boundary conditions for non-premixed flame (H3)

For the velocity inflow condition in case of the turbulent non-premixed Hydrogen flame H3, transient turbulent fluctuations generated using a digital filter based technique [31, 32] are superimposed on a fully developed turbulent pipe flow velocity profile at the nozzle exit. Outside the nozzle region in the inflow plane, the radial and azimuthal velocities are set to zero, the axial coflow velocity of 0.2 m/s is imposed, and Neumann condition is applied for other quantities. At the outflow and lateral boundaries, the Neumann condition is imposed for all quantities. To minimize the amplitude of spurious waves reflected at the boundaries of the computational domain, a sponge zone combining grid stretching and Laplacian filtering [33] is used in the outflow direction (to dissipate the flow fluctuations before they reach the outflow boundary), while absorbing layers consisting of grid stretching and damping terms (artificial dissipation through filtering) are implemented for the lateral boundaries of the computational domain.

4.5.1.2 Boundary conditions for spray flame (EtF3)

In case of the turbulent spray flame EtF3, radial profiles of mean axial velocity for the gas-phase and droplets in different size ranges (e.g., 1-10 μm, 10-20 μm, 20-30 μm, etc.), are used as inflow boundary conditions in the DNS and are depicted in Fig. 3.3. These mean velocity profiles are obtained from the best fit curves to the experimental data for radial profiles of mean axial velocity for various droplet size ranges, measured close to the central jet nozzle's exit plane at $x/D = 0.3$. It is also assumed that the radial profile of mean axial velocity for the smallest droplet size range ($1\mu\text{m} \leq d_d \leq 10\mu\text{m}$) corresponds to that of the gas-phase, and this assumption is in accordance with the experiment [5]. Furthermore, these mean velocity profiles represent fully developed two-phase flow behaviour [5].

Additionally, for the central spray nozzle transient turbulent fluctuations generated using a digital filter based technique [31, 32] are superimposed on the gas-phase mean velocities at the nozzle exit to simulate artificial inflow turbulence. The experimental data for radial profile of RMS fluctuations of gas-phase axial velocity at the nozzle exit

is supplied to the artificial turbulence generator. For the region outside pilot annulus exit (i.e. for $r > 12.5$ mm) at the inflow plane, an axial co-flow air velocity of 4.5 m/s is imposed (see Table 4.2) while the other velocity components are set to zero, and Neumann condition is applied to other physical quantities. At the outflow and lateral boundaries, the Neumann condition is imposed for all physical quantities.

To minimize the amplitude of acoustic waves reflected at the boundaries of the computational domain, a sponge zone combining grid stretching and Laplacian filtering [33] is used in the far downstream region towards the outflow boundary (last 30 grid points in x-direction), to dissipate the flow fluctuations and acoustic waves before they reach the outflow boundary. Artificial damping provided by the Laplacian filter is applied progressively in the sponge zone. Also, absorbing layers comprising of grid stretching and artificial dissipation which is obtained by applying a sixth order filter [34], are implemented towards the lateral boundaries of the computational domain. This helps to damp out the outgoing acoustic waves, thereby minimizing the reflection of acoustic waves at the lateral boundaries.

4.5.2 Numerical procedure for CAA

For simulating the propagation of acoustic waves produced by the noise sources, the CAA solver of the FK^3-CAA code solves the system of APE-RF in Eqs. (4.1) - (4.3). The CAA solver uses the 4^{th} order Dispersion-Relation Preserving (DRP) scheme of Tam and Shen [35, 36] for discretization of the spatial derivatives, and a 4^{th} order 6-stage Low Dissipation and Dispersion Runge-Kutta (LDDRK) scheme [37] for temporal integration to capture the acoustic wave propagation. To suppress spurious high-frequency waves, the low-pass filtering method of Artificial Selective Damping (ASD) proposed by Tam and Shen [35, 36] is applied.

The CAA computations for the non-premixed flame H3 are performed on a 3-D non-uniform Cartesian grid with $440 \times 340 \times 188$ grid points (a total of over 28 million grid points) in the x-, y- and z-directions, respectively. The domain size of the CAA grid for the H3 flame, in the respective Cartesian coordinate directions is $-12 \leq x/D_{H3} \leq 85$,

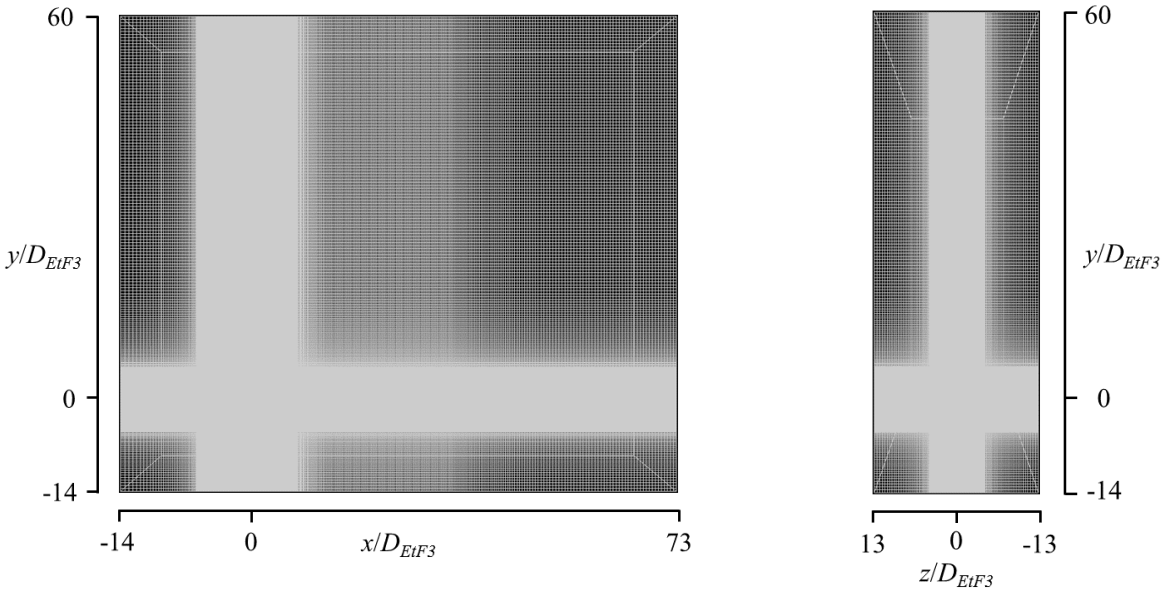

Figure 4.2: Cell distributions in the x-y and y-z planes of the Cartesian grid used in the CAA simulation of the spray flame EtF3 ($D_{EtF3} = 10.5$ mm).

$-12 \leq y/D_{H3} \leq 77$ and $-12 \leq z/D_{H3} \leq 12$.

While, for the CAA simulation of the spray flame EtF3, the 3-D non-uniform Cartesian grid consists of $510 \times 335 \times 198$ grid points (a total of 33.83 million grid points approximately) in the x-, y- and z-directions, respectively. And, the physical size of the CAA computational domain for the spray flame is $-10 \leq x/D_{EtF3} \leq 73$, $-14 \leq y/D_{EtF3} \leq 60$ and $-13 \leq z/D_{H3} \leq 13$, respectively in each of the three Cartesian coordinate directions. Cell distributions in the x-y and y-z planes of the Cartesian mesh grid used in the CAA simulation of the spray flame, are illustrated in Fig. 4.2 for visualization.

The quantities required for computing the propagation of acoustic waves in the CAA simulation, namely the mean speed of sound $\overline{c}$, the mean density $\overline{\rho}$, the mean flow velocities $\overline{\boldsymbol{u}}$, and the source term $q_{e,rf}$, are obtained from the solution of the DNS of the reacting flow-fields of the turbulent flames in the first step. These quantities are then mapped onto the CAA grid from the DNS grid using a trilinear algorithm. The CAA grids for both the flames (H3 and EtF3) are capable of resolving frequencies up to $f_{max} = 12000$ Hz, assuming a minimum resolution of seven points per wavelength

for the DRP scheme [35, 36] used in the CAA simulations. For the CAA computations of the non-premixed flame H3, the time increment is $\Delta t = 5.25 \times 10^{-7}$ s, while in case of the spray flame EtF3 $\Delta t = 5 \times 10^{-7}$ s. The same time increment values are used for the time integration of the respective DNS computations of these flames. The value of Δt chosen for each flame ensures that the CFL criterion is not violated, and in order to enable a constant sampling frequency of the results, Δt values are kept constant in both flames' simulations. The acoustic Courant number lies in the range of $\mathrm{CFL}_{\mathrm{acoust}} = 0.75 - 0.8$ for the CAA simulations of both the flames, while the convective Courant numbers of the DNS are approximately $\mathrm{CFL}_{\mathrm{conv}} = 0.33$ for the non-premixed flame H3 and $\mathrm{CFL}_{\mathrm{conv}} = 0.14$ for the spray flame EtF3.

At the artificial boundaries between the inner DNS domain (source region) and the outer CAA domain a damping zone treatment called silent embedded boundaries is introduced. Schröder and Ewert [12] derived the original formulation of the silent embedded boundaries to suppress the spurious noise generated by the sudden appearance of convecting vortical disturbances due to the truncated source region (i.e. CFD domain). Later Bui et al. [1] reformulated the silent embedded boundaries to be applicable to the pressure-density relation in the APE-RF system. Hence, in the present CAA simulations, silent embedded boundaries are used to suppress the spurious noise generated by the discontinuity in the distribution of entropy sources across the artificial boundary, and to avoid contamination of the acoustic solution. At the far-field boundaries of the CAA domain, the non-reflective radiation boundary conditions applicable to 3-D non-uniform mean flows formulated by Bogey and Bailly [33] have been used to avoid unphysical reflections into the computational domains. A sponge layer technique [33] has also been implemented at the left and right boundaries (in the x-direction of the grid) of the CAA domain.

The DNS of the turbulent flames are initially run for tens of thousands of iterations to allow for flame development and computation of mean flow-field quantities. Then the CAA simulations are switched on in case of both flames, and there onwards in every iteration the DNS step is performed first followed by the CAA step. The source term

$q_{e,rf}$ obtained from the DNS solution is interpolated onto the CAA grid at the end of every DNS step, to solve the APE-RF system in the CAA step. Sampling of the flow-field quantities (from DNS) as well as the fluctuating pressure and velocity signals (from CAA) are commenced there onwards by running the simulations for a physical time of 74 ms for the H3 flame and 99 ms for the EtF3 flame. For computation of the combustion noise results, the computed temporal signals are converted to the frequency domain using Fast Fourier Transform (FFT). The time period of signal extraction is divided into sections with a 50% overlap, and these sections are used for subsequent averaging of the noise spectra.

The complete CPU time required for the DNS/APE-RF computations (i.e. time for initial DNS plus time for combined DNS/CAA computations) is approximately 639000 hours for the H3 flame and 1105920 hours for the EtF3 flame, by parallel computation using 1024 cores on a CRAY-XC40 supercomputer at the Academic Centre for Computing and Media Studies (ACCMS), Kyoto University (the actual time required for the computations is approximately 624 hours of real time for the H3 flame and 1080 hours of real time for the EtF3 flame).

4.6 Results and discussion

4.6.1 Flow-field results

The instantaneous temperature fields computed from the DNS are depicted in Fig. 4.3, showing the predicted flame structures of both the turbulent non-premixed jet flame H3 (left) and the turbulent spray flame EtF3 (right) in their respective central x-y planes. The lengths in the axial and radial directions for both flames depicted in Fig. 4.3 are the same, with the dimensions being in mm. The non-premixed flame H3 which is a purely gaseous flame has a jet exit Reynolds number $Re = 10000$, while the spray flame EtF3 has a jet exit Reynolds number $Re = 19700$. However, the lower Re H3 flame exhibits slightly wider spreading in the radial direction compared to the higher Re spray flame EtF3. This is caused by the inflow velocity boundary conditions of the flames.

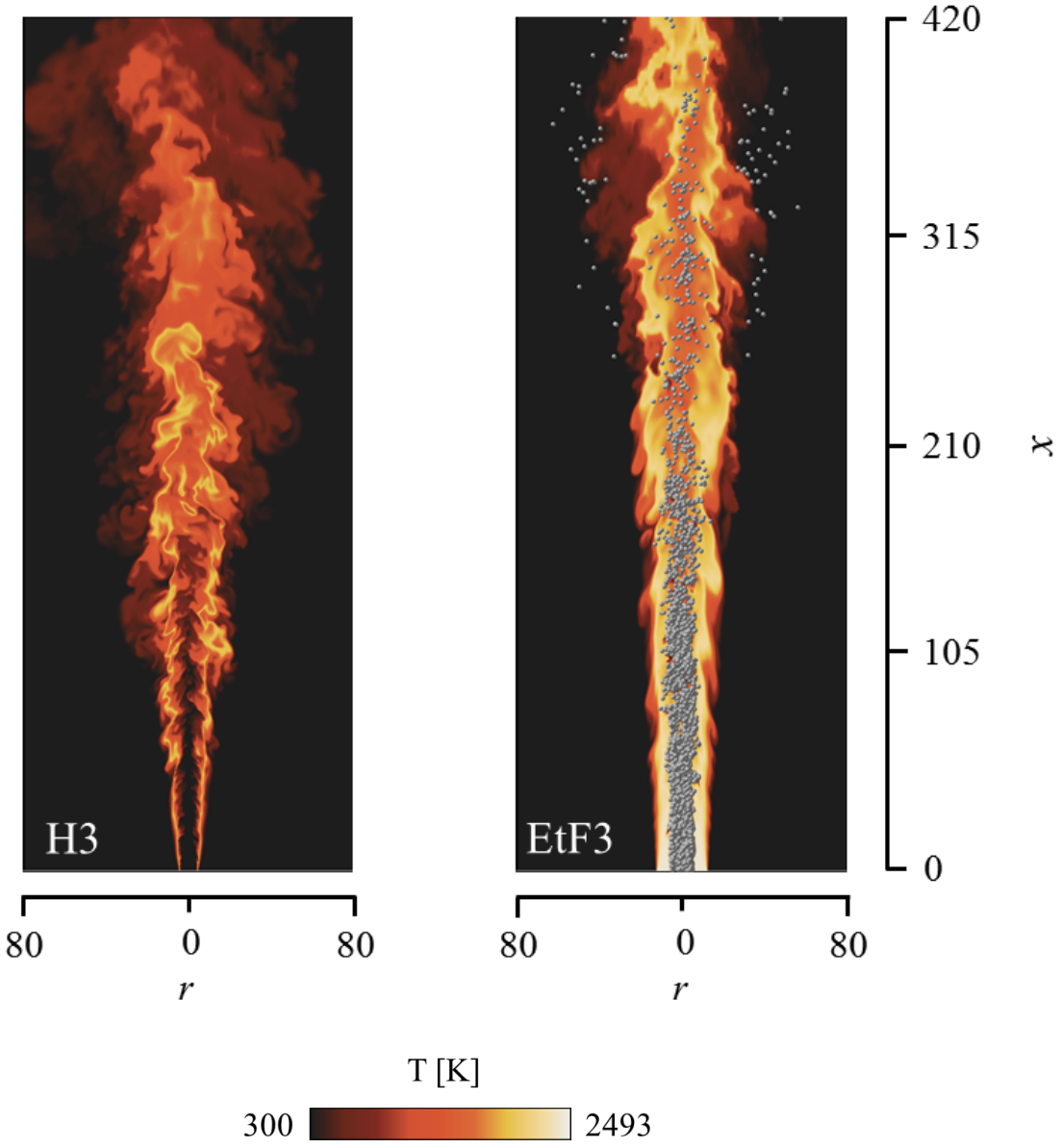

Figure 4.3: Instantaneous snapshots of the DNS computed temperature fields of the turbulent non-premixed flame H3 (left) and spray flame EtF3 (right). Lengths shown in the axial (x) and radial (r) directions are the same for both flames, with all dimensions being in mm.

The non-premixed flame H3 is a simple jet flame with bulk jet velocity at nozzle exit U_{jet} = 34.8 m/s and co-flow velocity U_{coflow} = 0.2 m/s. Whereas, the turbulent spray flame EtF3 is a piloted flame with bulk jet velocity at central nozzle exit U_{jet} = 24 m/s. The velocity of its coaxial pilot flame that surrounds the central jet nozzle is U_{pilot} = 11.6 m/s and the co-flow velocity is U_{coflow} = 4.5 m/s. The H3 flame which has a velocity ratio $U_{jet}/U_{coflow} = 174$, while the spray flame EtF3 has a velocity ratio $U_{jet}/U_{coflow} = 5.33$. This velocity ratio U_{jet}/U_{coflow} strongly influences the mixing layer growth and mass entrainment [38]. Therefore, the H3 flame which has a larger velocity ratio exhibits slightly more radial spread compared to spray flame EtF3. Moreover, the inflow configuration of the spray flame EtF3 is a bit more complex than that of the non-premixed flame H3, due to the presence of the annular pilot flame between the central jet stream and the co-flow stream. There is mixing between the central jet stream (containing Ethanol + Air) and the hot pilot stream (contains fully-burned products of combustion), between the pilot stream and the co-flow stream (Air), and between the central jet stream and the co-flow stream, all of which occur simultaneously. This produces more droplet dispersion with increasing downstream distance from the burner exit plane.

In Fig. 4.3, the instantaneous temperature field of the spray flame EtF3 also contains gray entities that represent the dispersed fuel droplets. These fuel droplets get convected downstream with the flow after exiting the central nozzle, and the size of the fuel droplets reduces gradually as a consequence of evaporation. The high temperature gas-phase surrounding the fuel droplets ignites the newly formed fuel vapors and promotes further combustion reaction. A steady reduction in droplet count with increasing distance from the burner exit in the downstream direction is evident, which is precisely due to the evaporation of droplets caused by the surrounding hot gas-phase. Once a droplet's diameter falls below 1 μm due to evaporation into gaseous Ethanol, it is omitted from the computation, and its remaining mass, momentum and energy are transferred to the gas-phase.

Next, the flow-field quantities computed from the DNS of the H3 flame are validated

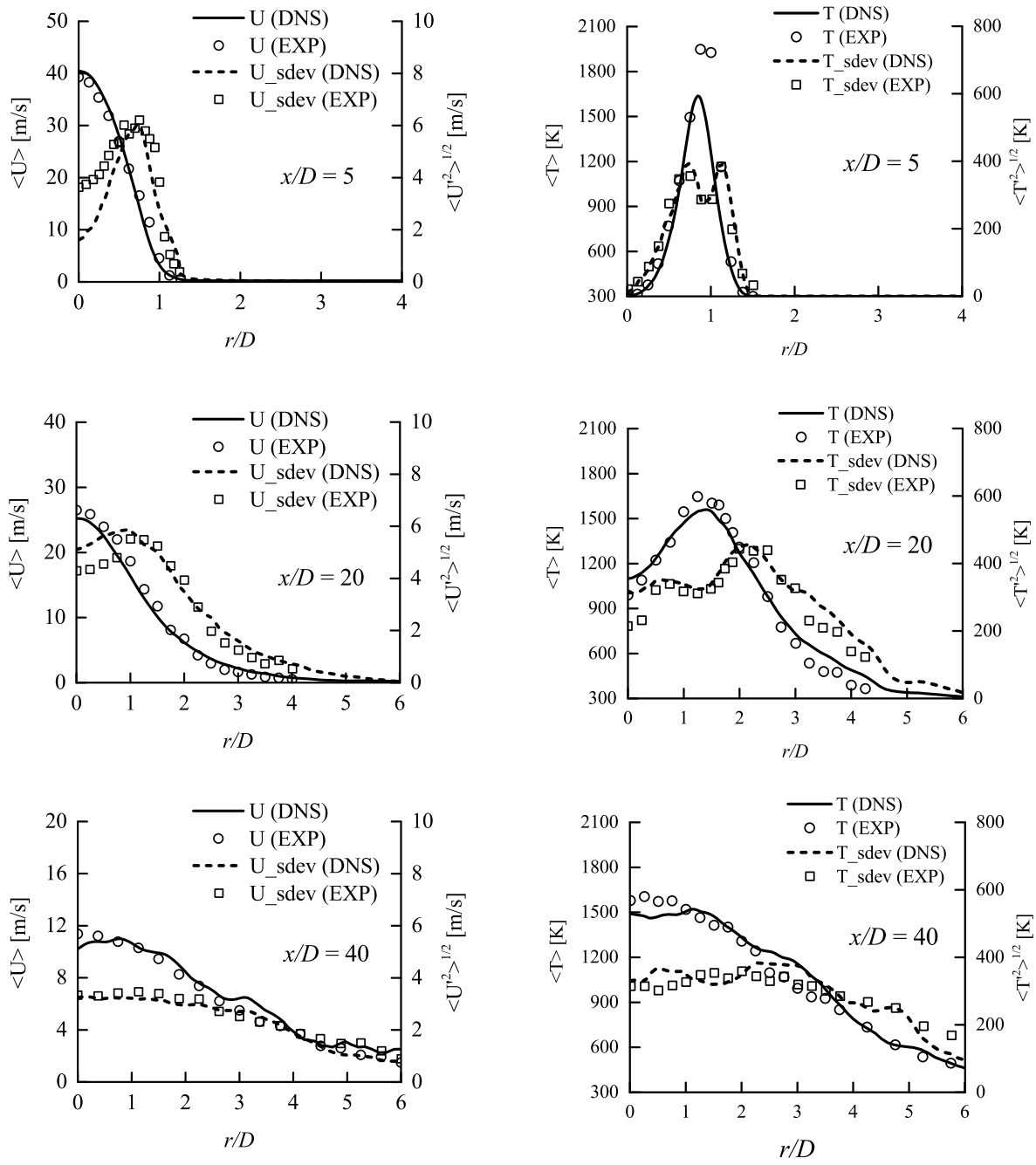

Figure 4.4: Computed and measured [4] radial profiles of the H3 flame at various streamwise locations. Left column: mean and standard deviation of axial velocity; Right column: mean and standard deviation of temperature. "EXP" stands for experimental data and "sdev" means standard deviation.

against experimental data [4] in the form of first and second order statistics. Computed radial profiles for mean and standard deviation of axial velocity and temperature are presented in Fig. 4.4. It should be noted that, the figures wherein any quantity expressed within triangular parentheses "<>" indicates the time averaging of that quantity. The DNS results show good agreement with measurements at all stream-wise locations for both the velocity and temperature statistics. With increasing downstream location from the nozzle exit, the radial profiles of the mean and standard deviations of both axial velocity and temperature become flatter, and their corresponding magnitudes reduce gradually. Therefore, the H3 flame's spreading is accurately reproduced as is apparent from the radial distributions of axial velocity and temperature in Fig. 4.4. In Fig. 4.5, the DNS results for the radial profiles of standard deviation of radial velocity show good conformity to experimental data at different stream-wise locations, while favorable agreement is also observed for the computed radial profiles of mean and standard deviation of mixture fraction Z for the H3 flame at different stream-wise locations, as illustrated in Fig. 4.6. Here, the mixture fraction is defined as

$$Z = \frac{Y_F - Y_O/s + Y_{O\infty}/s}{Y_{F\infty} + Y_{O\infty}/s} \tag{4.30}$$

where, Y_F is the mass fraction of fuel in the gas mixture, Y_O is the mass fraction of Oxygen in the gas mixture, $Y_{O\infty}$ is the Oxygen mass fraction in the oxidizer stream, $Y_{F\infty}$ is the fuel mass fraction in the fuel stream, and s is the stoichiometric mass ratio defined as $s = (Y_O/Y_F)_{st}$ where the subscript "st" indicates stoichiometric mixture condition. Under the stoichiometric mixture condition, the mixture fraction is defined as

$$Z_{st} = \frac{Y_{O\infty}/s}{Y_{F\infty} + Y_{O\infty}/s} \tag{4.31}$$

where, Z_{st} is called the stoichiometric mixture fraction. If $Z > Z_{st}$ the fuel is excess and the mixture is called fuel rich, whereas if $Z < Z_{st}$ the fuel is deficient and the mixture is called fuel lean.

Validation of the DNS computed flow-field statistical quantities against experimental

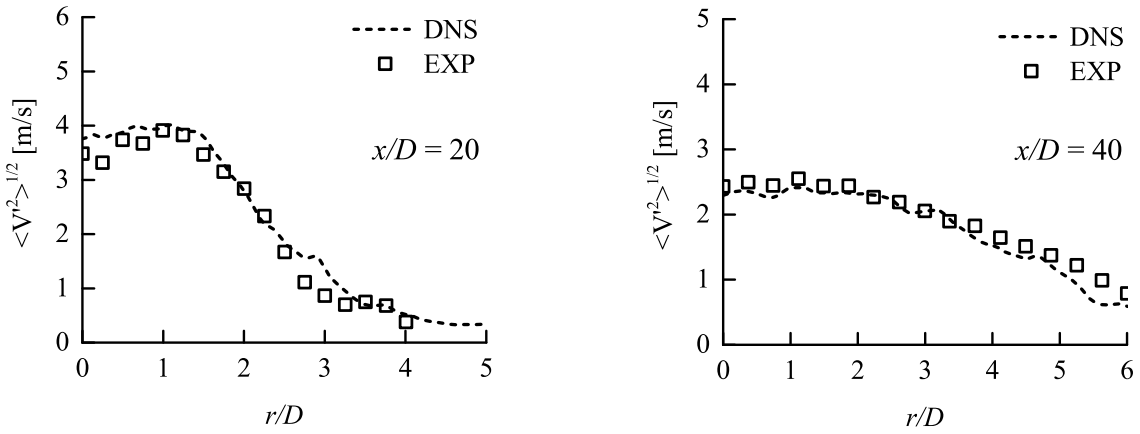

Figure 4.5: Computed and measured [4] radial profiles of standard deviation of radial velocity at different stream-wise locations for the H3 flame.

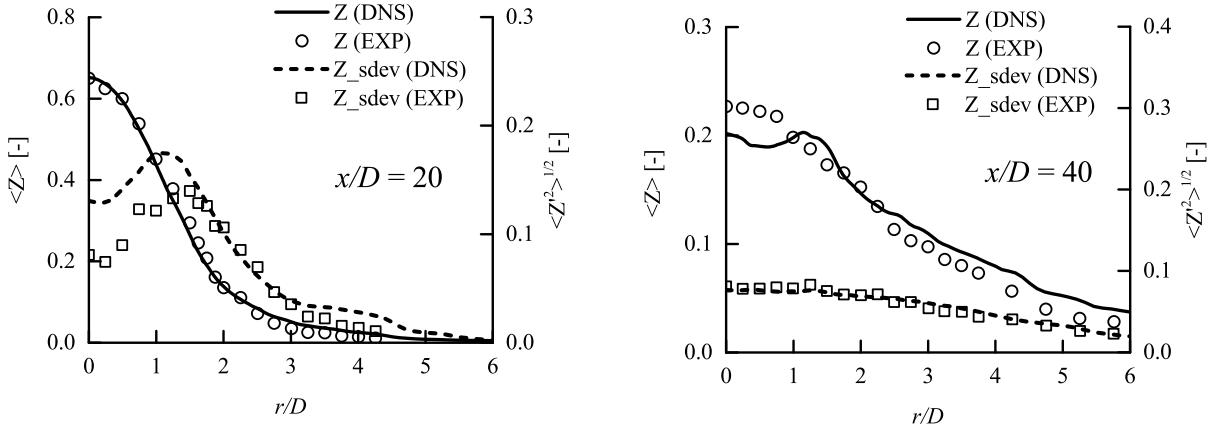

Figure 4.6: Radial profiles of mean and standard deviation of mixture fraction Z of the H3 flame compared with measurements [4] at different stream-wise locations.

measurements, for the turbulent spray flame EtF3 has already been discussed in Section 3.5.1 of Chapter 3. The overall good agreement of the DNS results with experiments, for the flow-field quantities of both the flames allows further use of the DNS for combustion noise investigations.

4.6.2 Combustion noise results

Based on the quality of the DNS results for both flames, the acoustic source term $q_{e,rf}$ required for the computations of the acoustic fields generated by the flames is evaluated using the DNS solution. The source term $q_{e,rf}$ is examined in terms of its spatial distribution and strength for both the flames. The instantaneous distributions of the source term $q_{e,rf}$ are illustrated in Fig. 4.7 for the non-premixed flame H3 (left) and the spray flame EtF3 (right). In both the flames, the strongest acoustic sources are primarily located in the regions influenced by the unsteady heat release of combustion reaction. And this is evident in Fig. 4.7, where the strongest acoustic sources in both flames are situated within the red lines, which represent the iso-surfaces of stoichiometric mixture fraction Z_{st} of the respective flames ($Z_{st} = 0.3$ for H3 flame and $Z_{st} = 0.1$ for EtF3 flame). For the H3 flame, the strongest sources are located in the region $0 \leq x \leq 160$ mm and beyond $x \geq 200$ mm the source strength is quite diminished. With increasing distance from the nozzle exit, the amount of fuel available for combustion decreases, therefore, the effect of the dominant source mechanism of combustion noise in $q_{e,rf}$ i.e., the unsteady heat release rate also decreases with increasing downstream distance.

In case of the spray flame EtF3, the instantaneous distribution of source term $q_{e,rf}$ shows that the acoustic sources extend over a larger axial region compared to the H3 flame. This is due to the fact that, unlike the gaseous non-premixed H3 flame, the spray flame EtF3 has fuel injected in the form of liquid droplets and the unburned droplets that get convected further downstream, provide the fuel necessary for additional heat release process. Hence, strong acoustic sources corresponding to the dominant source mechanism in $q_{e,rf}$ can be seen even up to $x = 280$ mm. Furthermore, the source term $q_{e,rf}$ is stronger in case of the spray flame EtF3 compared to the non-premixed

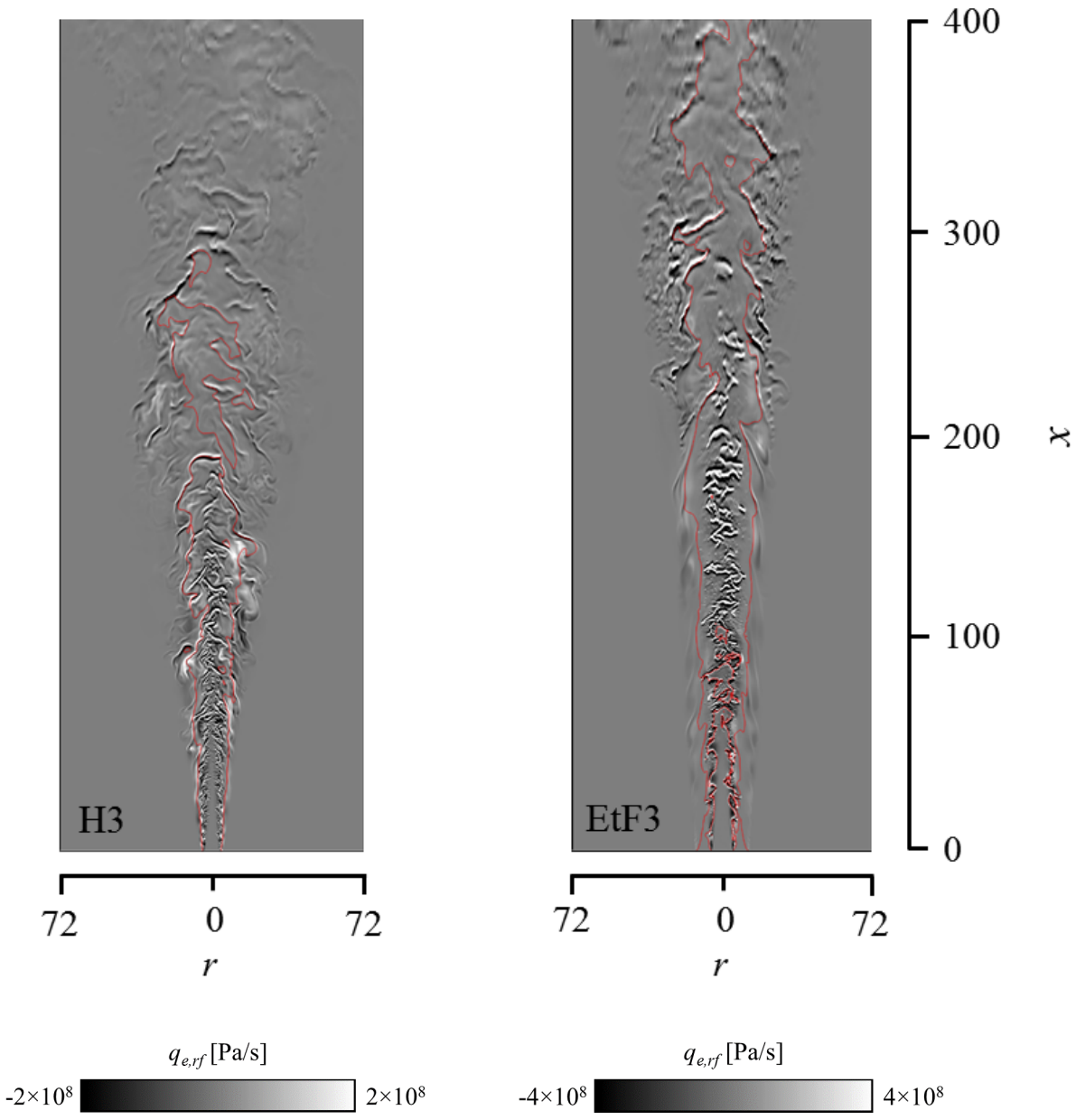

Figure 4.7: Instantaneous distributions of the acoustic source term $q_{e,rf}$ for the turbulent non-premixed flame H3 (left) and spray flame EtF3 (right). The red lines in each of the instantaneous $q_{e,rf}$ fields represent the iso-surfaces of stoichiometric mixture fraction Z_{st} of the respective flames. Lengths shown in the axial (x) and radial (r) directions are the same for both flames, with all dimensions being in mm.

flame H3. This is likely caused by the higher Reynolds number of the spray flame EtF3 ($Re = 19700$) compared to the H3 flame ($Re = 10000$), which causes stronger turbulent velocity fluctuations, that leads to stronger fluctuations in heat release rate and density in the spray flame EtF3. Moreover, in Fig. 4.7 it can be seen that, in both the flames some acoustic sources are also present outside the iso-surfaces of stoichiometric mixture fraction Z_{st}. Contrary to the acoustic sources confined within the iso-surface of Z_{st} (whose dominant source mechanism is the unsteady heat release rate), the acoustic sources on the outside are produced by various other source mechanisms included in the source term $q_{e,rf}$, which results in the unsteady transport of the density field. This results in some source contributions in the far downstream regions and outside the iso-surface of Z_{st}, even though heat release (chemical reaction) processes are not necessarily occurring in those regions.

Snapshots of the instantaneous perturbation pressure p' fields (in gray scale) of both the flames are illustrated in Fig. 4.8, which represent the acoustic fields generated by these flames. Also shown are the distributions of the acoustic source term $q_{e,rf}$ represented by the colored contours, and in case of the spray flame EtF3, the dispersed fuel droplets are depicted by the yellow entities. The spray flame EtF3 generates a stronger acoustic field (higher perturbation pressures) than the non-premixed flame H3, which is a direct consequence of the stronger acoustic sources present in the spray flame. Furthermore, in the spray flame EtF3, unburned fuel droplets that get convected downstream can be seen in the far downstream locations. These evaporating fuel droplets generate more gaseous Ethanol which subsequently undergoes combustion, resulting in unsteady heat release and hence, acoustic sources $q_{e,rf}$ in these far downstream locations. In both flames, noise generation occurs along a wide axial spread owing to the distributed acoustic sources in the axial direction. Overall, both flames behave like a cylindrical noise radiating source and at a fixed radial distance from each flame's axis, the noise radiation is not in phase along the axial direction. The acoustic sources and hence, the acoustic fields (sound pressure levels and frequencies) generated by the flames depend on a number of parameters, such as flow velocity, turbulence intensity, burner size and geometry,

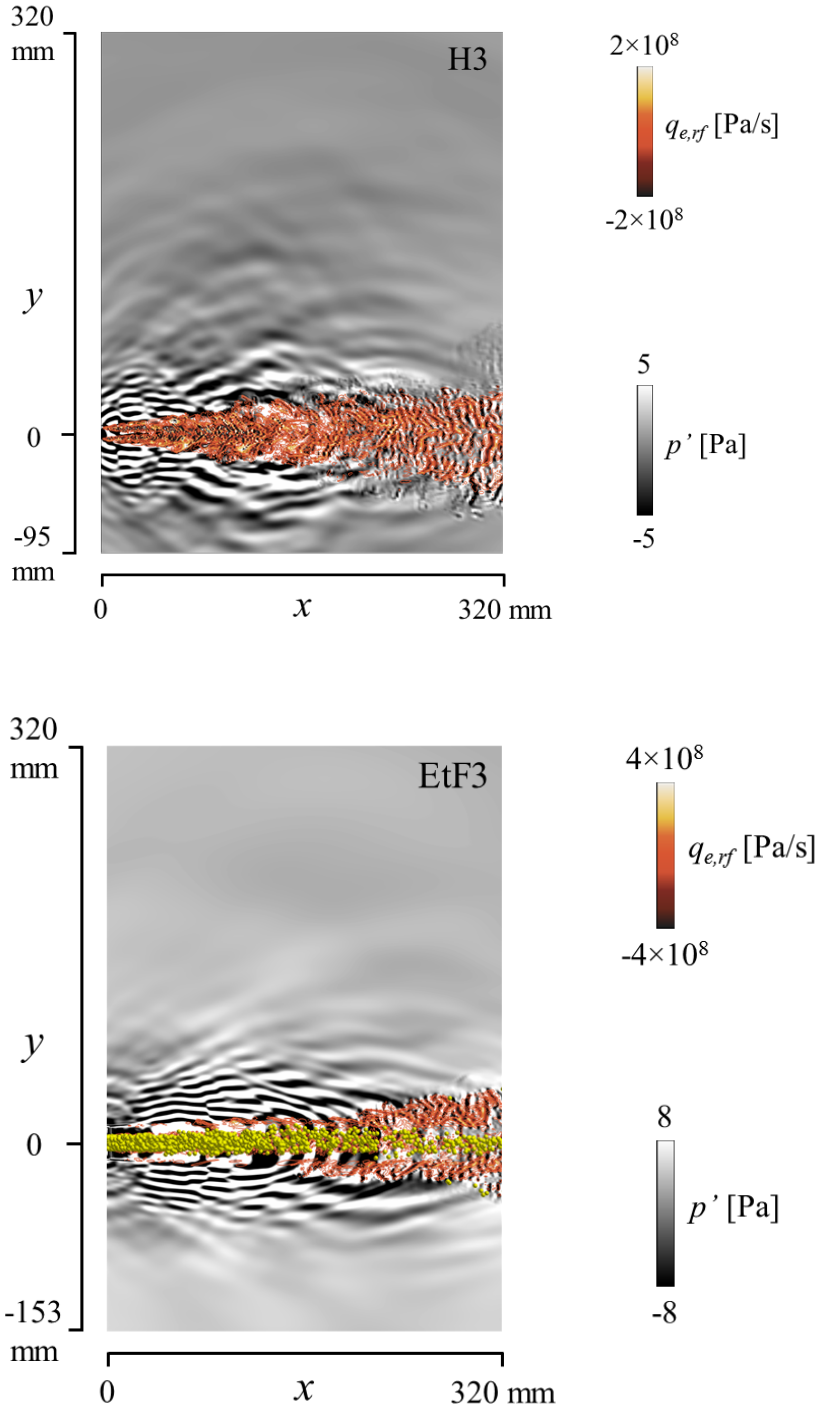

Figure 4.8: Snapshots of the instantaneous fields of perturbation pressure p' (gray scale) and acoustic source term $q_{e,rf}$ (colored contours), and distribution of dispersed fuel droplets (yellow entities, only for the spray flame EtF3 and droplet sizes are exaggerated) computed from the hybrid DNS/APE-RF approach for the turbulent non-premixed flame H3 (top) and spray flame EtF3 (bottom) in the central x-y planes of their respective CAA Cartesian grids.

fuel consumption rate, flame temperature and type of fuel. However, the shape of open flame combustion noise spectra is not affected by the above parameters and is nearly universal [39–41], and this is true for the spray flame also, as will be demonstrated later in this study.

First, the combustion noise results obtained from the DNS/APE-RF approach are validated against experimental data for the turbulent non-premixed flame H3. The sound intensity level spectra of the H3 flame, computed from the CAA simulation are compared with measurements in Fig. 4.9. The positions in the far-field where these spectra have been computed, are the same positions at which the microphones were used to measure the sound intensity spectra in the experiment conducted by Piscoya et al. [42]. Each position at which the spectra are computed, corresponds to a different radiation angle θ with the flame axis. Minor discrepancies in the computed sound intensities are attributed to the interpolation errors in the acoustic source term. This is because, the source term $q_{e,rf}$ which is computed on the DNS grid, has to be interpolated onto the CAA grid and the CAA mesh is not typically aligned with the DNS mesh at certain places within the overlapping source region, which might introduce errors in the CAA solution. However, the overall agreement between the computed and measured sound intensity spectra is mostly good at all positions for the H3 flame, in terms of the sound intensity levels, spectral content and shapes.

Based on this validation, the hybrid DNS/APE-RF approach is used to investigate the combustion generated acoustic field of the turbulent spray flame EtF3. Next, the sound pressure spectra of the spray flame EtF3 computed from the CAA solution, are compared to the combustion noise similarity spectrum suggested by Tam et al. [41] as shown in Fig. 4.10. In the experimental investigation conducted by Tam et al. [41], extensive measurements showed that combustion noise has a unique spectral shape. This spectral shape was demonstrated to be the same as the similarity spectrum for large scale turbulence noise of high-speed jets, discovered by Tam, Golebiowski and Seiner [43]. Moreover, this spectral shape of combustion noise was found remain unaltered with variation in the direction of noise radiation, including the spectral peak which exhibited

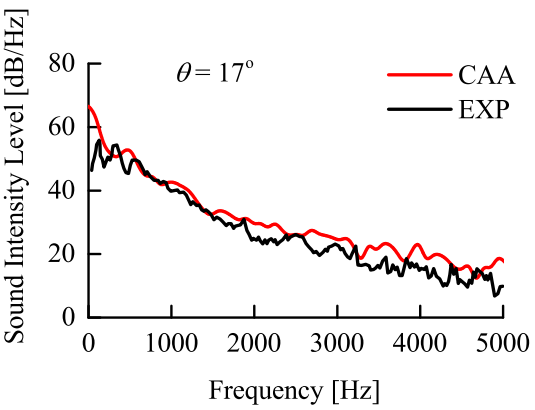

(a) $(x, y) = (640\text{ mm}, 200\text{ mm})$; $\theta = 17°$

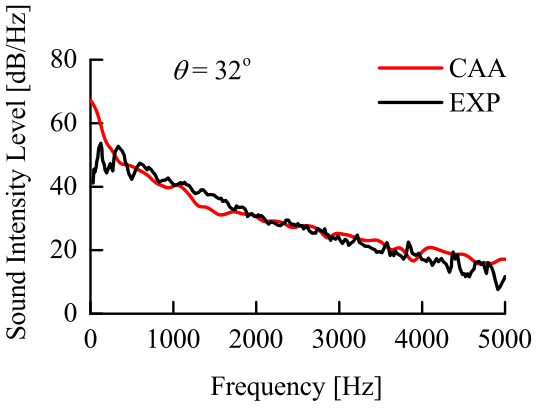

(b) $(x, y) = (640\text{ mm}, 400\text{ mm})$; $\theta = 32°$

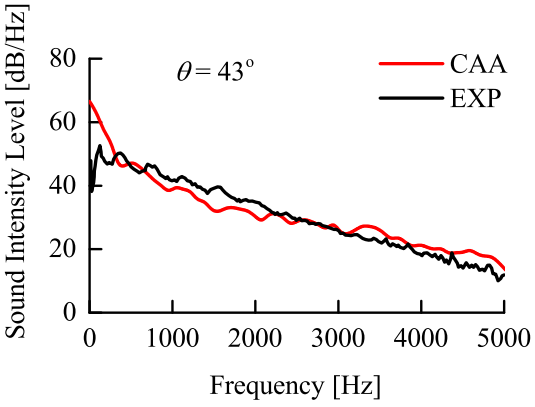

(c) $(x, y) = (544\text{ mm}, 504\text{ mm})$; $\theta = 43°$

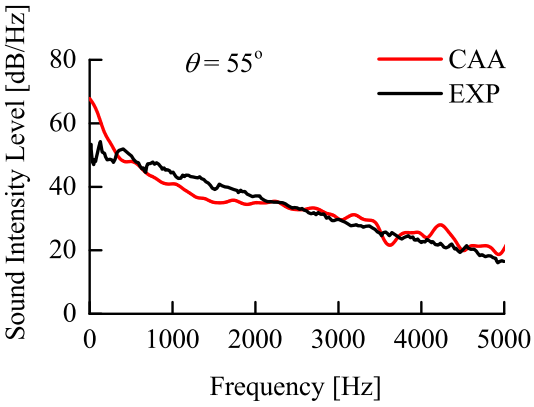

(d) $(x, y) = (344\text{ mm}, 504\text{ mm})$; $\theta = 55°$

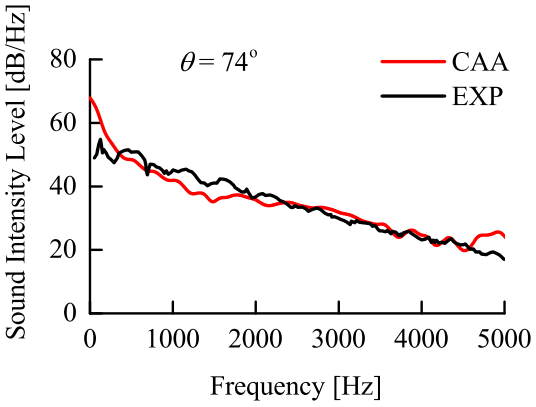

(e) $(x, y) = (144\text{ mm}, 504\text{ mm})$; $\theta = 74°$

Figure 4.9: Comparison of the sound intensity level spectra of the H3 flame computed at various positions in the central x-y plane of the CAA grid with measurements [42]. θ is the angle of the observer position with respect to the flame axis.

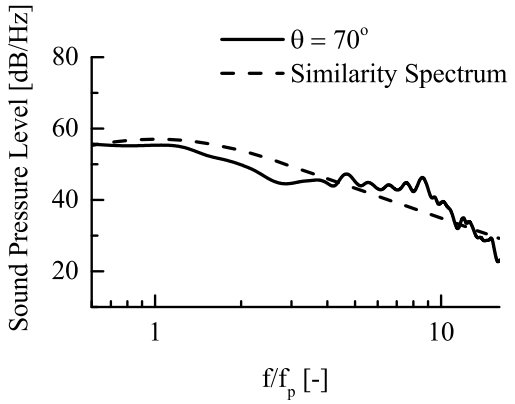

(a) $(x, y) = (144\text{ mm}, 400\text{ mm})$; $\theta = 70°$

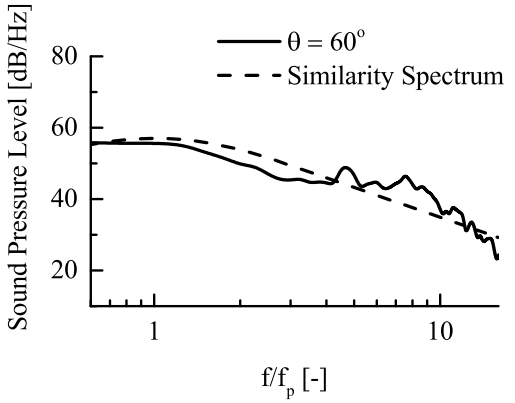

(b) $(x, y) = (240\text{ mm}, 400\text{ mm})$; $\theta = 60°$

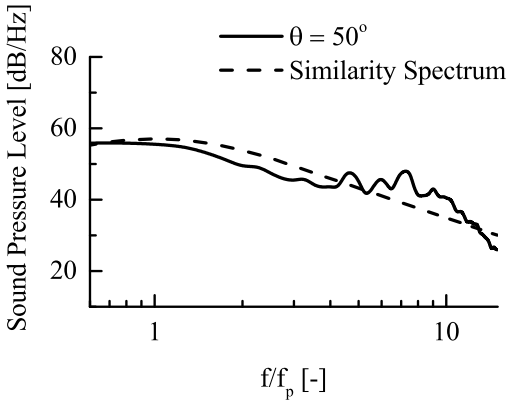

(c) $(x, y) = (336\text{ mm}, 400\text{ mm})$; $\theta = 50°$

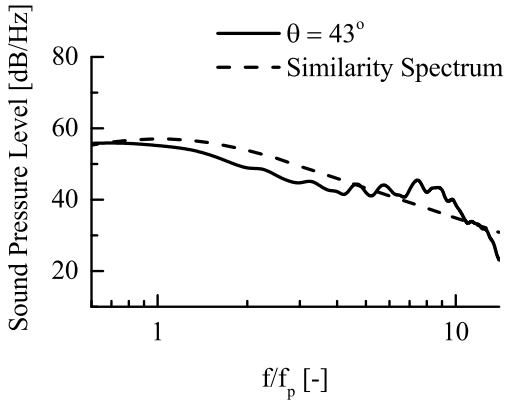

(d) $(x, y) = (432\text{ mm}, 400\text{ mm})$; $\theta = 43°$

Figure 4.10: Comparison between computed sound pressure spectra of the spray flame EtF3 and the combustion noise similarity spectrum proposed by Tam et al. [41] at various positions that correspond to different radiation angles θ with respect to the flame axis in the central x-y plane of the CAA grid.

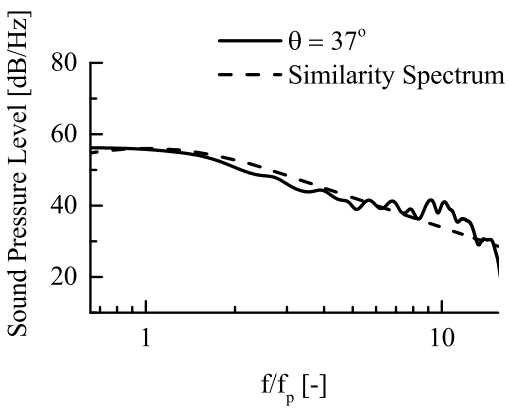

(e) $(x, y) = (528\text{ mm}, 400\text{ mm})$; $\theta = 37°$

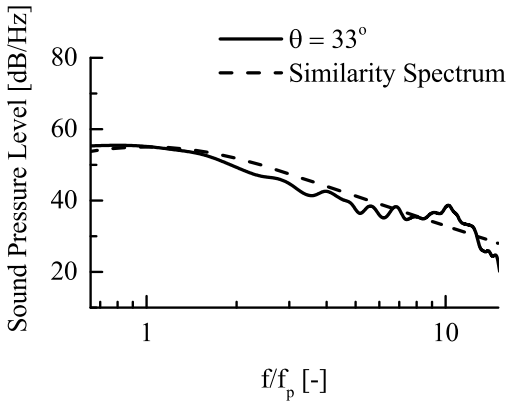

(f) $(x, y) = (624\text{ mm}, 400\text{ mm})$; $\theta = 33°$

Figure 4.10: Continued.

nearly uniform directivity [41]. The spectral shape's analytical formula is described in [41, 43].

In Fig. 4.10, the combustion noise similarity spectrum is represented by the dotted curve and has been displaced vertically for comparison with the computed sound pressure spectra. The abscissa in these plots represent the normalized frequency, where f is the spectral frequency and f_p is the frequency corresponding to the peak of the spectrum, known as peak frequency. The sound pressure spectra of combustion noise emitted by the open turbulent spray flame EtF3, obtained from the CAA simulation show good agreement with the combustion noise similarity spectrum proposed by Tam et al. [41]. Moreover, shapes of the computed noise spectra conform to that of the suggested similarity spectrum of open flame combustion noise, regardless of the radiation angle. The peak frequency of the spray flame's combustion noise spectra is found to be $f_p \approx 400$ Hz for $\theta \geq 43°$, but for the low radiation angles of $\theta < 43°$, the peak frequency is found to be $f_p \approx 320$ Hz. The drop in the value of peak frequency f_p for low radiation angles is caused by the acoustic refraction effects stemming from the temperature dependent mean sound speed gradients within the hot flame, which results in stronger refractions of the high-frequency noise emissions compared to the low-frequency noise emissions. Thus, the noise spectrum experiences a shift to low-frequencies at the far downstream

positions corresponding to low radiation angles to the flame axis. This refraction phenomenon is examined and explained for the spray flame Etf3 later. The sound pressure levels at the spectral peaks are also nearly the same, irrespective of the radiation angle. These combustion noise characteristics of the open turbulent spray flame EtF3 are therefore, similar to those of open turbulent non-premixed flames in general [15, 44], and to those reported in the experimental findings of Tam et al. [41] for combustion noise measurements.

The sound pressure spectra computed for the far-field positions at a constant distance of $y = 400$ mm from the flame axis and at increasing stream-wise distances from the nozzle exit are depicted in Fig. 4.11. These positions are, $(x, y) = (0, 400$ mm), (48 mm, 400 mm), (144 mm, 400 mm), (240 mm, 400 mm), (336 mm, 400 mm), (432 mm, 400 mm), (528 mm, 400 mm) and (624 mm, 400 mm), corresponding to radiation angles of $\theta = 90°$, 83°, 70°, 60°, 50°, 43°, 37° and 33°, respectively to the flame axis. The CAA computed noise spectra of the spray flame are broadband, and the sound pressure levels and spectral shapes are virtually similar at all radiation angles for the low-frequencies (i.e. for f $<$ 1000 Hz).

For the positions corresponding to radiation angles greater than 43°, i.e., $(x, y; \theta) =$ (0, 400 mm; 90°), (48 mm, 400 mm; 83°), (144 mm, 400 mm; 70°), (240 mm, 400 mm; 60°) and (336 mm, 400 mm; 50°), it is found that the spectral shapes and sound pressure levels are quite similar for the entire frequency range presented in Fig. 4.11(a). The reason for this is attributed to the extended distribution of the acoustic sources of the spray flame EtF3, in the axial direction as depicted in Fig. 4.7. Hence, a cone of silence (region in the acoustic field subjected to diminished noise irradiation) where the sound pressure levels of the high-frequency noise emissions undergo attenuation, is not observed for the positions corresponding to radiation angles greater than 43°.

Furthermore, for the same positions mentioned above, the sound pressure levels are nearly constant in the frequency range of 1000 Hz $<$ f $<$ 3000 Hz, forming a plateau in the frequency spectra, which is represented by the red dash-dotted horizontal line in Fig. 4.11(a). This characteristic is very similar to that observed in a previous experimental

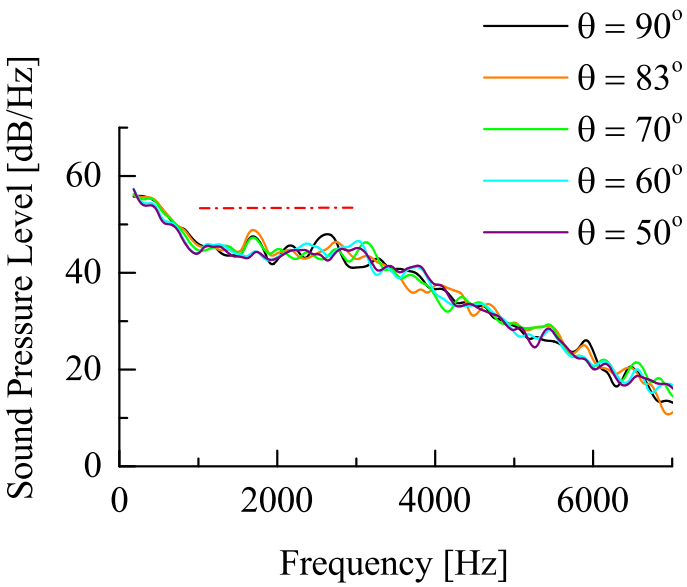

(a)

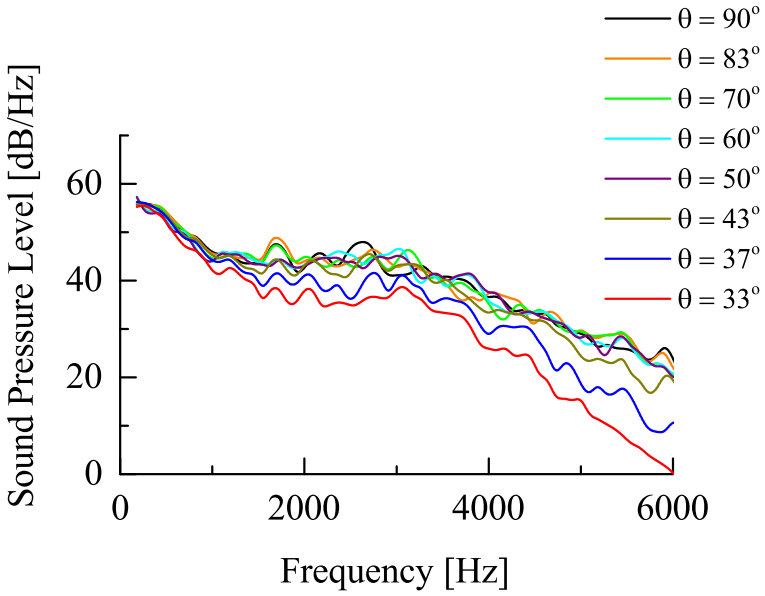

(b)

Figure 4.11: Sound pressure spectra computed at different stream-wise locations and at a constant distance of $y = 400$ mm from the flame axis in the central x-y plane of the CAA grid, corresponding to different radiation angles θ to the flame axis for the spray flame EtF3. The red dash-dotted horizontal line in (a) qualitatively indicates the constant sound pressure level plateau in the spectra computed for the positions corresponding to $\theta > 43°$, in the frequency range 1000 Hz $<$ f $<$ 3000 Hz.

study for turbulent non-premixed flames by Singh et al. [15], where a plateau of constant sound pressure level was observed in the noise spectra of DLR-A and DLR-B flames [3] in the frequency range 400 Hz $<$ f $<$ 2000 Hz. In the present study, the existence of such a plateau of nearly constant sound pressure level in the mid-frequency range (1000 Hz $<$ f $<$ 3000 Hz) for positions corresponding to $\theta > 43°$, could be attributed to the strong acoustic sources existing up to farther downstream locations in the EtF3 spray flame (see Fig. 4.7). Furthermore, for f $>$ 3000 Hz the sound pressure level decreases in an almost linear fashion for all the positions, and this characteristic is also similar to that of the sound pressure spectra of turbulent non-premixed flames [15].

However, in Fig. 4.11(b) it is found that, for the high-frequency noise emissions (f $>$ 1000 Hz), suppression of sound pressure levels with increasing downstream location from the nozzle exit (which corresponds to decreasing radiation angle to the flame axis), is apparent for the positions $(x, y; \theta)$ = (528 mm, 400 mm; 37°) and (624 mm, 400 mm; 33°). For the position $(x, y; \theta)$ = (432 mm, 400 mm; 43°), such reduction in sound pressure levels becomes appreciable for f $>$ 4000 Hz. The reduction in sound pressures of the high-frequency noise emissions is more pronounced for the downstream positions corresponding to $\theta < 43°$, which would create a relative cone of silence in these far downstream positions (at low radiation angles to the flame axis). This downstream attenuation of high-frequency noise emissions is caused by refraction effects due to temperature non-uniformities within the flame [45], and such weak directivity in the high-frequency noise emissions has been confirmed in previous investigations of turbulent non-premixed flames [15, 16]. Furthermore, the APE-RF system solved in the CAA simulation is capable of capturing such acoustic refraction effects of the high-frequency noise components, produced by gradients in mean sound speed within the turbulent flame [18].

The temperature non-uniformities existing in the flame lead to gradients in the speed of sound, which is illustrated by the distributions of mean speed of sound in the turbulent non-premixed flame H3 (left) and the turbulent spray flame EtF3 (right) in Fig. 4.12. When the high-frequency acoustic waves propagate in the flame downstream direction,

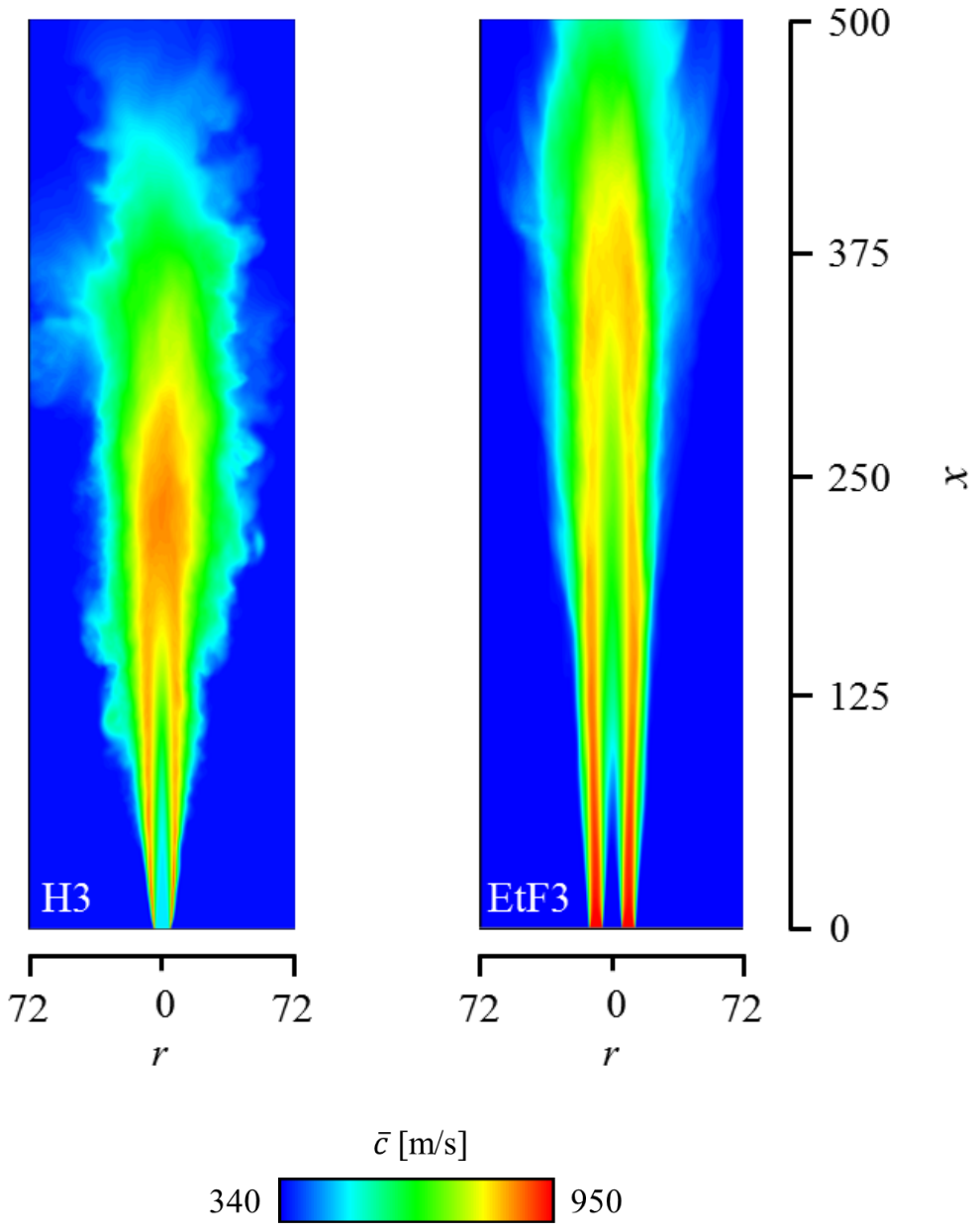

Figure 4.12: Distributions of the mean speed of sound for the turbulent non-premixed flame H3 (left) and spray flame EtF3 (right). Lengths shown in the axial (x) and radial (r) directions are the same for both flames, with all dimensions being in mm.

they get refracted away from the flame axis upon interacting with the mean sound speed gradients within the flame. Such acoustic refractions due to temperature dependent variations in the mean speed of sound, are mostly relevant in the flame downstream direction [46]. Furthermore, it is evident from Fig. 4.11(b) that the refraction effect becomes stronger with increasing frequency, i.e. the higher the noise emission frequency, the stronger the attenuation of its sound pressure level.

The frequency-specific noise directivity effects of the spray flame EtF3 are detailed in Fig. 4.13. For this exercise, the sound pressure levels corresponding to several different frequencies have been computed from the CAA solution, at various positions that lie on a circular arc of radius $R = 525$ mm in the central x-y plane of the CAA grid, and centered at the nozzle exit i.e. at $(x,y,z) = (0,0,0)$. Each position on the circular arc is at an angle to the flame axis ranging from 20° to 90°. The sound pressure levels at the low-frequencies (f $<$ 1000 Hz) in Fig. 4.13(a)-(c), are nearly the same for all radiation angles indicating a monopole behavior. This monopole character at the low-frequencies is attributed to the unsteady heat release rate, which also happens to be the dominant source mechanism of combustion noise in the source term $q_{e,rf}$. Moreover, the sound pressure levels are greater for the low-frequency noise emissions as compared to those of the higher frequency noise emissions (f $>$ 1000 Hz). In the higher-frequencies, the range of sound pressure levels can be seen to decrease with increasing frequency in Fig. 4.13(d)-(r). Furthermore, most of the acoustic energy of combustion noise generated by the spray flame EtF3 is situated within the low-frequencies, which confirms the low-frequency characteristic of the spray flame's combustion noise similar to that of low Mach number premixed [13, 14] and non-premixed flames [15, 16]. The noise directivity starts deviating from the monopole behavior in Fig. 4.13(e) for f = 1181.81 Hz. At further higher frequencies, such as in Fig. 4.13(f)-(r), the directivity of noise emissions starts exhibiting multipole-type character. This non-isotropic behavior of the high-frequency noise emissions is attributed to the source mechanisms other than the unsteady heat release in the source term $q_{e,rf}$, which contribute to the sound pressures at high-frequencies. Since, the high-frequency noise emissions are more susceptible to

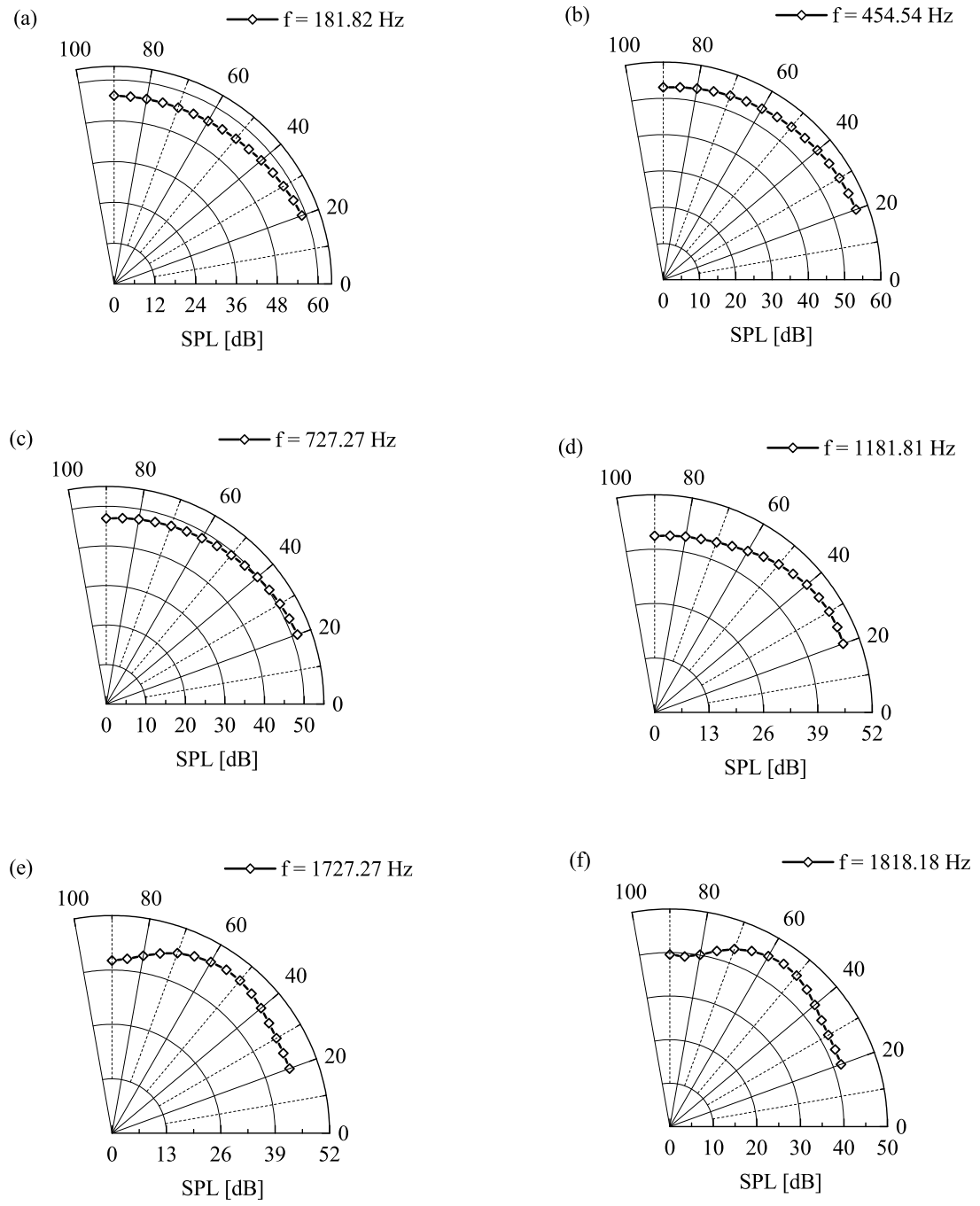

Figure 4.13: Frequency-specific Sound Pressure Level (SPL) computed at various positions on a circular arc of radius $R = 525$ mm in the central x-y plane of the CAA grid, the origin of which is located at the nozzle exit i.e. $(x,y,z) = (0,0,0)$. Each position on this circular arc is considered at an increment of 5 degrees starting from 20° up to 90° to the flame axis.

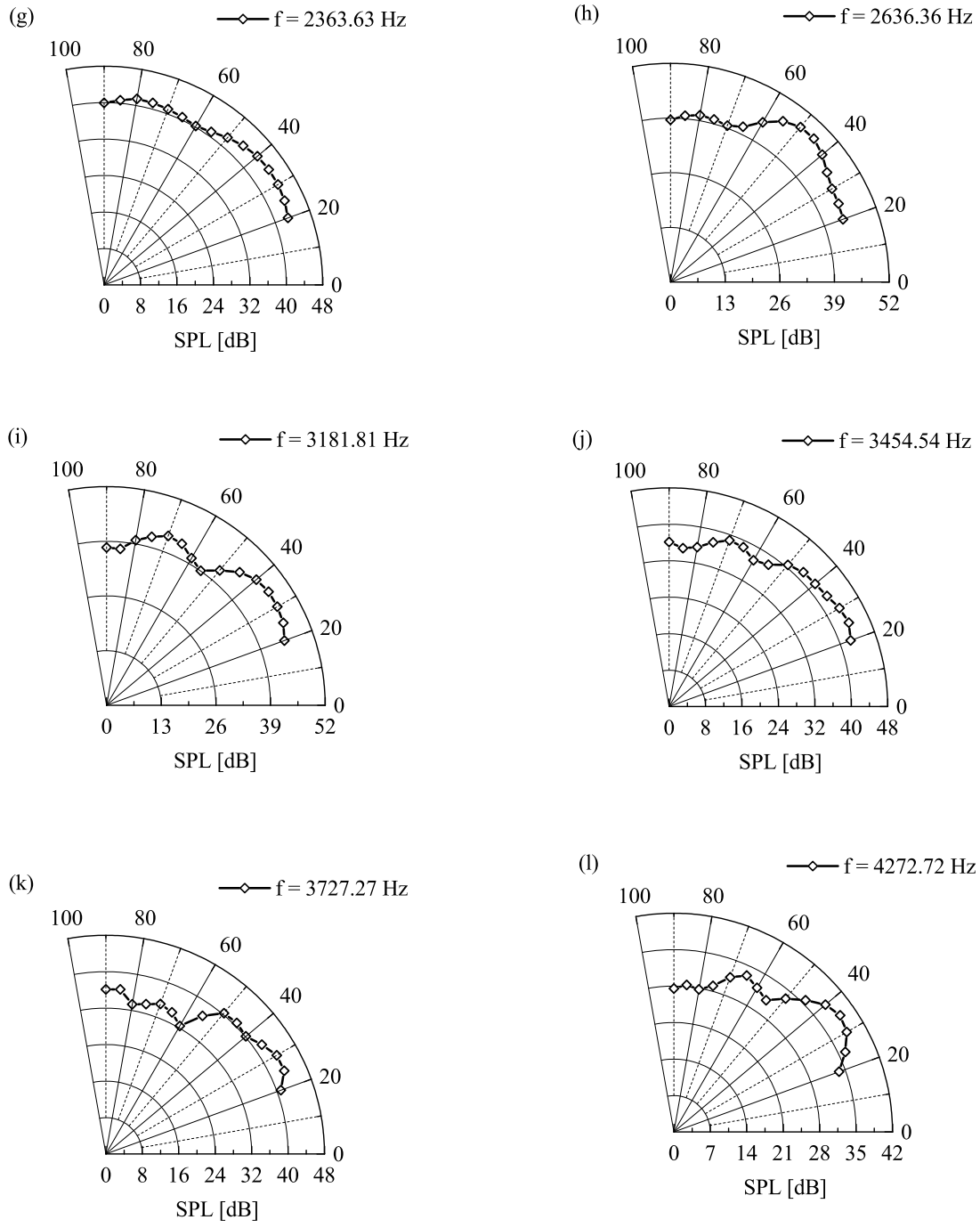

Figure 4.13: Continued.

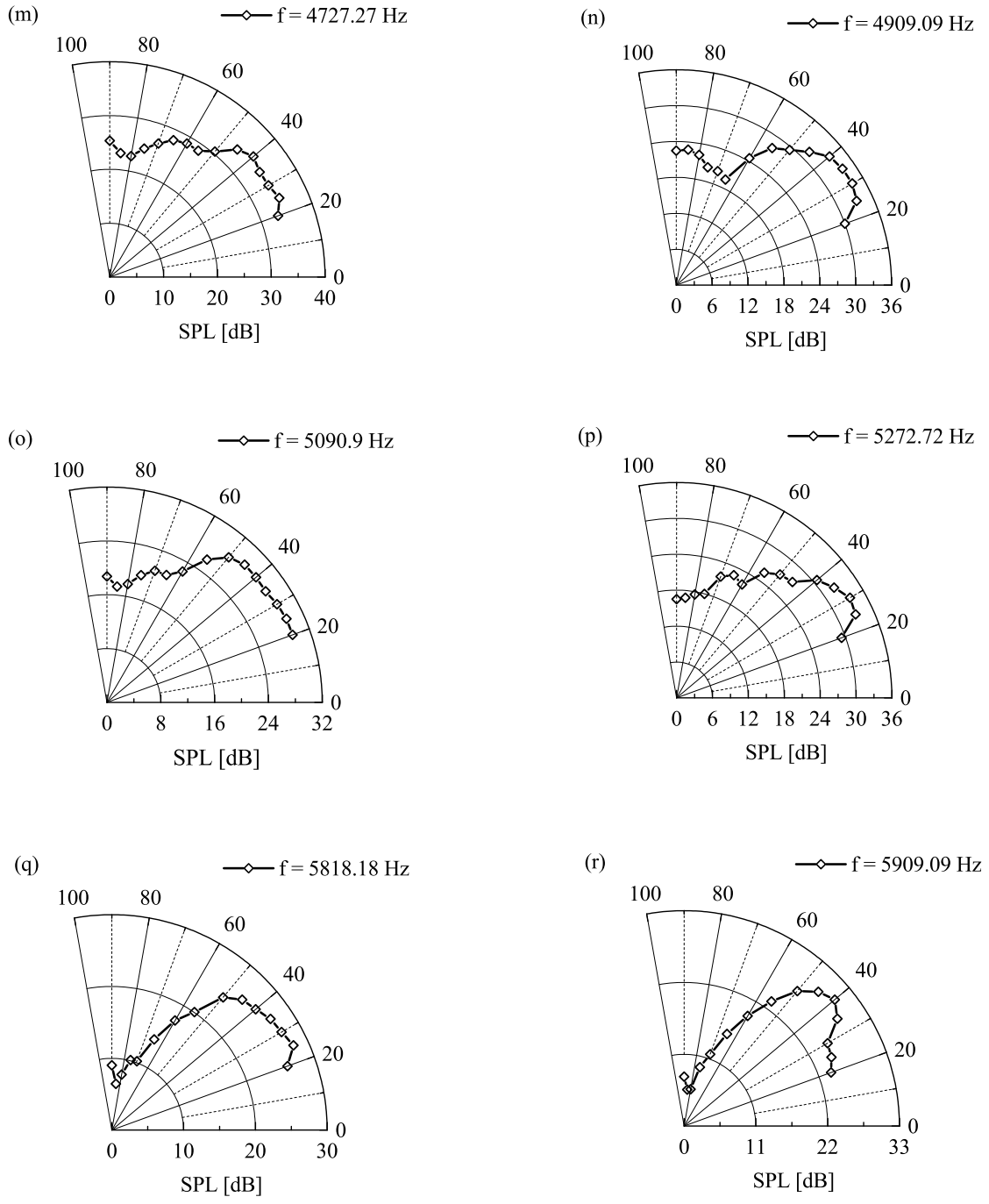

Figure 4.13: Continued.

acoustic refraction effects (caused by mean sound speed gradients within the flame) than the low-frequency noise emissions, departure from monopole/isotropic behavior for the noise directivity at high-frequencies is thus evident. Therefore, the higher the noise emission frequency, the stronger the directivity of sound pressure level (stronger deviation from isotropic character of sound pressure level).

4.7 Conclusions

The relatively new numerical framework of the hybrid CFD/CAA approach was applied to the turbulent spray flame EtF3 ($Re = 19700$, fuel = Ethanol) and the turbulent non-premixed flame H3 ($Re = 10000$, fuel = Hydrogen), to predict and analyze the radiation of combustion generated noise. In this two-step framework, the first step involves a DNS of the reacting flow-field of the turbulent flame (within which the sources exciting acoustic waves are present), while the second step involves a CAA simulation that is performed by solving the Acoustic Perturbation Equations extended for Reacting Flows (APE-RF), to capture the acoustic wave propagation all the way into the far-field.

In order to incorporate the additional effect of density variations caused by fuel droplet evaporation, the source term dominating the excitation of acoustic waves in combustion noise was reformulated for the spray flame EtF3. First, the hybrid approach was used to simulate the experimental open turbulent non-premixed Hydrogen flame H3. The results obtained from the DNS/APE-RF approach for the Hydrogen flame's flow-field statistical quantities, as well as the radiated sound intensities were extensively validated against experimental data. Next, the hybrid DNS/APE-RF approach was applied to the experimental open turbulent spray flame EtF3, for simulating its two-phase reactive flow-field, and its combustion generated acoustic field, with the objective of predicting and analyzing the noise radiation behavior.

The results obtained from the hybrid DNS/APE-RF approach for combustion noise spectra of the spray flame EtF3 in the far-field, revealed characteristics similar to those of turbulent non-premixed flames in general, such as, the broadband shape of the sound

pressure spectra of combustion noise generated by the spray flame, good conformity of the computed noise spectra to the combustion noise similarity spectrum of open flames [41] regardless of the direction of noise radiation, virtually same spectral content in the low-frequencies and a nearly constant sound pressure level plateau in the mid-frequencies for various radiation angles to the flame axis, and attenuation of the high-frequency noise radiated towards the far downstream positions (at low radiation angles to the flame axis) which was caused by acoustic refraction effects stemming from the sound speed gradients (which is in turn caused by the temperature non-uniformities) within the flame. Furthermore, combustion noise generated by the spray flame exhibited low-frequency frequency characteristic, implying that most of the acoustic energy was situated within the low-frequencies, similar to turbulent non-premixed flames. Therefore, the hybrid DNS/APE-RF approach developed in this study is capable of accurately capturing the characteristics of radiation of combustion generated noise up to the far-field.

References

[1] T. P. Bui, W. Schröder, and M. Meinke. Numerical analysis of the acoustic field of reacting flows via acoustic perturbation equations. *Comput. & Fluids*, 37:1157–1169, 2008.

[2] T. P. Bui, M. Ihme, W. Schröder, and H. Pitsch. Analysis of different sound source formulations to simulate combustion generated noise using a hybrid LES/APE-RF method. *Int. J. Aeroacoustics*, 8:95–124, 2009.

[3] R. Barlow. editor, Proceedings of the TNF workshops, Sandia National Laboratories, 1996-2004, Livermore, CA. *available at www.ca.sandia.gov/TNF.*

[4] D. G. Pfuderer, A. A. Neuber, G. Früchtel, E. P. Hassel, and J. Janicka. Turbulence modulation in jet diffusion flames: Modeling and experiments. *Combust. Flame*, 106:301–317, 1996.

[5] J. D. Gounder, A. Kourmatzis, and A. R. Masri. Turbulent piloted dilute spray flames: Flow fields and droplet dynamics. *Combust. Flame*, 159:3372–3397, 2012.

[6] N. M. Marinov, C. K. Westbrook, and W. J. Pitz. Detailed and global chemical kinetics model for hydrogen. San Francisco, CA, 1995. 8$^{\text{th}}$ International Symposium on Transport Properties.

[7] C. K. Westbrook and F. L. Dryer. Simplified reaction mechanisms for the oxidation of hydrocarbon fuels in flames. *Combust. Sci. Tech.*, 27:31–43, 1981.

[8] R. Ewert and W. Schröder. Acoustic perturbation equations based on flow decomposition via source filtering. *J. Comput. Physics*, 188:365–398, 2003.

[9] R. Ewert and W. Schröder. On the simulation of trailling edge noise with a hybrid LES/APE method. *J. Sound Vib.*, 270:509–524, 2004.

[10] D. G. Crighton, A. P. Dowling, J. E. Ffowcs Williams, M. Heckl, and F. G. Leppington. *Modern Methods in Analytical Acoustics*. Springer, 1992.

[11] T. P. Bui, W. Schröder, and M. Meinke. Acoustic perturbation equations for reacting flows to compute combustion noise. *Int. J. Aeroacoustics*, 6:335–355, 2007.

[12] W. Schröder and R. Ewert. *Some concepts of LES-CAA coupling, LES for Acoustics*. Cambridge University Press, 2005.

[13] T. J. B. Smith and J. K. Kilham. Noise generation by open turbulent flames. *J. Acoust. Soc. Am.*, 35:715–724, 1963.

[14] B. N. Shivashankara, W. C. Strahle, and J. C. Handley. Combustion noise radiation by open turbulent flames. *AIAA paper*, 1973-1025 (1973), 1973.

[15] K. K. Singh, S. H. Frankel, and J. P. Gore. Study of spectral noise emissions from standard turbulent nonpremixed flames. *AIAA Journal*, 42:931–936, 2004.

[16] M. Ihme and H. Pitsch. On the generation of direct combustion noise in turbulent non-premixed flames. *Int. J. Aeroacoust.*, 11:25–78, 2012.

[17] F. A. Williams. *Combustion Theory, The Fundamental Theory of Chemically Reacting Flow Systems*. Addison-Wesley, 1964.

[18] T. P. Bui and W. Schröder. *Combustion Noise: Theoretical and Numerical Analysis of Broadband Combustion Noise*. Springer, 2009.

[19] C. T. Crowe, M. P. Sharma, and D. E. Stock. The Particle-Source-In Cell (PSI-CELL) model for gas-droplet flows. *J. Fluids Eng.*, 99:325–332, 1977.

[20] K. Luo, O. Desjardins, and H. Pitsch. DNS of droplet evaporation and combustion in a swirling combustor. In *Annual Research Briefs*. Center for Turbulence Research, NASA Ames/Stanford University, 2008.

[21] K. Luo, H. Pitsch, M. G. Pai, and O. Desjardins. Direct numerical simulations and analysis of three-dimensional n-heptane spray flames in a model swirl combustor. *Proc. Combust. Inst.*, 33:2143–2152, 2011.

[22] T. Kitano, R. Kurose, and S. Komori. Effects of internal pressure and inlet velocity disturbances of air and fuel droplets on spray combustion field. *J. Therm. Sci. Technol.*, 8(1):269–280, 2013.

[23] T. Kitano, J. Nishio, R. Kurose, and S. Komori. Evaporation and combustion of multicomponent fuel droplets. *Fuel*, 136:219–225, 2014.

[24] T. Kitano, T. Tsuji, R. Kurose, and S. Komori. Effect of pressure oscillations on flashback characteristics in a turbulent channel flow. *Energy Fuels*, 29(10):6815–6822, 2015.

[25] T. Kitano, K. Kaneko, R. Kurose, and S. Komori. Large-eddy simulations of gas– and liquid–fueled combustion instabilities in back-step flows. *Combust. Flame*, 170:63–78, 2016.

[26] A. L. Pillai and R. Kurose. Numerical investigation of combustion noise in an open turbulent spray flame. *Applied Acoustics*, 133:16–27, 2018.

[27] V. Moureau, C. Bérat, and H. Pitsch. An efficient semi-implicit compressible solver for large-eddy simulations. *J. Comput. Physics*, 226(2):1256–1270, 2007.

[28] G.-S. Jiang and C.-W. Shu. Efficient implementation of weighted ENO schemes. *J. Comput. Physics*, 126:202–228, 1996.

[29] R. J. Kee, D.-L. Graham, J. Warnatz, M. E. Coltrin, and J. A. Miller. A fortran computer code package for the evaluation of gas-phase, multicomponent transport properties. SANDIA Report No. SAND86-8246, Sandia National Laboratories, Albuquerque NM, Livermore CA, 1986.

[30] R. J. Kee, F. M. Rupley, and J. A. Miller. Chemkin-II: A FORTRAN chemical kinetics package for the analysis of gas-phase chemical kinetics. SANDIA Report No. SAND89-8009B, Sandia National Laboratories, Albuquerque NM, Livermore CA, 1989.

[31] M. Klein, A. Sadiki, and J. Janicka. A digital filter based generation of inflow data for spatially developing direct numerical or large eddy simulations. *J. Comput. Physics*, 186:652–665, 2003.

[32] A. M. Kempf, S. Wysocki, and M. Pettit. An efficient, parallel low-storage implementation of Klein' s turbulence generator for LES and DNS. *Comput. Fluids*, 60:58–60, 2012.

[33] C. Bogey and C. Bailly. Three-dimensional non-reflective boundary conditions for acoustic simulations: Far field formulation and validation test cases. *Acta. Acust. united Ac.*, 88:463–471, 2002.

[34] C. A. Kennedy and M. H. Carpenter. Several new numerical methods for compressible shear-layer simulations. *Appl. Numer. Math.*, 14:397–433, 1994.

[35] C. K. W. Tam and H. Shen. Direct computation of nonlinear acoustic pulses using high order finite difference schemes. In: AIAA Paper 93-4325, 1993.

[36] C. K. W. Tam. Computational aeroacoustics: Issues and methods. *AIAA Journal*, 33(10):1788–1796, 1995.

[37] C. Bogey and C. Bailly. A family of low dispersive and low dissipative explicit schemes for flow and noise computations. *J. Comput. Physics*, 194:194–214, 2004.

[38] G. L. Brown and A. Roshko. On density effects and large structure in turbulent mixing layers. *J. Fluid. Mech.*, 64:775–816, 1974.

[39] S. Kotake and K. Takamoto. Combustion noise: Effects of the shape and size of burner nozzle. *J. Sound Vib.*, 112:345–354, 1987.

[40] S. Kotake and K. Takamoto. Combustion noise: Effects of velocity turbulence of unburned mixture. *J. Sound Vib.*, 139:9–20, 1990.

[41] C. K. W. Tam, N. N. Pastouchenko, J. Mendoza, and D. Brown. Combustion noise of auxiliary power units. *AIAA paper*, 2005-2829 (2005), 2005.

[42] R. Piscoya, H. Brick, M. Ochmann, and P. Költzsch. Equivalent source method and boundary element method for calculating combustion noise. *Acta Acust. united Ac.*, 94(4):514–527, 2008.

[43] C. K. W. Tam, M. Golebiowski, and J. M. Seiner. On the two components of turbulent mixing noise from supersonic jets. *AIAA paper*, 96-1716 (1996), 1996.

[44] B. Mühlbauer, R. Ewert, O. Kornow, and B. Noll. Broadband combustion noise simulation of open non-premixed turbulent jet flames. *Int. J. Aeroacoust.*, 11(1):1–24, 2012.

[45] W. C. Strahle. Some results in combustion generated noise. *J. Sound Vib.*, 23:113–125, 1972.

[46] M. Ihme, M. Kaltenbacher, and H. Pitsch. Numerical simulation of flow- and combustion-induced sound using a hybrid LES/CAA approach. 497–510. Proceedings of the Summer Program, Center for Turbulence Research, 2006.

Chapter 5

Conclusions

5.1 Summary and conclusions

In this work, the combustion noise generated by open turbulent non-premixed and spray flames have been predicted and investigated using different numerical strategies, namely DNS and hybrid DNS/APE-RF approach. The objective was to attain a better understanding of the combustion noise characteristics in turbulent flames, and to elucidate the underlying mechanism. All the flames investigated in the present work are experimentally investigated flames, therefore thorough validation of the numerical results against experimental measurements were also conducted. The important findings of the investigations carried out during the course of this doctoral program are summarized as follows.

In Chapter 2, DNS was used to analyze the direct combustion noise generated by two open turbulent non-premixed Hydrogen jet flames. The flames designated as H5 (Reynolds number Re = 6200) and H3 (Reynolds number Re = 10000) had the same Nitrogen-diluted Hydrogen fuel mixture (H_2/N_2 : 50/50 volume %), but different bulk jet exit velocities resulting in different Reynolds numbers for the two flames. Here, emphasis was placed on studying the effect of Reynolds number on the noise generation from both the turbulent non-premixed Hydrogen flames, and the mechanism influencing the combustion noise behavior due to variation in Reynolds number was clarified. DNS

predictions for flow-field statistical quantities of both flames were found to be in good agreement with experimental data. Comparison of the computed sound intensity level spectra with experimental data for the non-premixed Hydrogen flame H3 also showed favorable agreement. Analysis of the noise generated by the two flames revealed the following:

1. Strong influence of the monopole-type combustion noise sources on the sound pressure field was observed in both flames, which was inferred from the noise directivity in terms of sound pressure level spectra and OASPL at various emission angles to the flame axis, while the influence of the quadrupole-type turbulence noise sources was found to be negligible.

2. Higher turbulent velocity fluctuations and turbulence intensities were observed in the H3 flame ($Re = 10000$) compared to the H5 flame ($Re = 6200$), which caused greater fluctuations of heat release rate in the H3 flame.

3. Consequently, the combustion noise sources which arise from the heat release rate fluctuations were stronger in the H3 flame compared to the H5 flame. Hence, the combustion noise generated by the higher Re H3 flame was found to be louder than that of the lower Re H5 flame.

In Chapter 3, the combustion noise generated by an open turbulent spray flame with Ethanol as fuel (flame designation: EtF3) was investigated by means of DNS employing an Eulerian-Lagrangian framework with two-way coupling. In this investigation of a two-phase reacting flow, the carrier gas-phase's governing equations were solved in an Eulerian framework, while the evaporating liquid fuel droplets were individually tracked in a Lagrangian framework. A two-step global reaction model was used to describe the combustion reaction of gaseous Ethanol. The DNS predictions for flow field statistical quantities like droplet velocities and corresponding fluctuations, and gas-phase excess temperature showed an overall good agreement with experimental data. The turbulent spray flame exhibited combustion noise characteristics similar to those of turbulent non-premixed flames in general, in terms of spectral content and directivity, such as

1. The spectra of direct combustion noise generated by the spray flame was found to be broadband.

2. Noise directivity characteristics showed fairly similar spectral shapes and sound pressure levels at the low-frequencies for various emission angles to the flame axis, which suggested the dominance of distributed monopole combustion noise sources arising from unsteady heat release rate fluctuations.

3. At the high-frequencies, on the other hand, reduction of sound pressure levels of noise emissions with increasing distance from the nozzle exit (corresponding to decreasing emission angle to the flame axis) was observed. The reason for this weak directivity of the high-frequency noise emissions was attributed to the refraction effects arising from temperature-dependent gradients in the sound speed within the flame, and such refraction effects have been observed in the experimental studies for turbulent non-premixed flames in general.

4. Furthermore, the DNS computed sound pressure spectra of combustion noise from the open turbulent spray flame, were comparable to the similarity spectrum of open flame combustion noise regardless of the direction of emission.

In Chapter 4, the relatively new numerical framework of the hybrid CFD/CAA approach was applied to the turbulent spray flame (EtF3, $Re = 19700$) and the turbulent non-premixed flame (H3, $Re = 10000$), to predict and analyze the radiation of combustion generated noise. In this two-step framework, the first step involves a DNS of the reacting flow-field of the turbulent flame (within which the sources exciting acoustic waves are present), while the second step involves a CAA simulation that is performed by solving the Acoustic Perturbation Equations extended for Reacting Flows (APE-RF), to capture the acoustic wave propagation all the way into the far-field. In order to incorporate the additional effect of density variations caused by fuel droplet evaporation, the source term dominating the excitation of acoustic waves in combustion noise was reformulated for the spray flame EtF3. First, the hybrid approach was used to simulate the experimental open turbulent non-premixed Hydrogen flame H3, for which measured

flow-field statistics and combustion noise data are readily available. The results obtained from the DNS/APE-RF approach for the Hydrogen flame's flow-field statistical quantities, as well as the radiated sound intensities were extensively validated against experimental data. Next, the hybrid DNS/APE-RF approach was applied to the experimental open turbulent spray flame EtF3, for simulating its two-phase reactive flow-field, and its combustion generated acoustic field, with the objective of predicting and analyzing the noise radiation behavior. The results obtained from the hybrid DNS/APE-RF approach for combustion noise spectra of the spray flame (Case EtF3) in the far-field revealed the characteristics similar to those of turbulent non-premixed flames in general, such as

1. The broadband shape of the sound pressure spectra of combustion noise.

2. The computed noise spectra of the spray flame showed good conformity to the combustion noise similarity spectrum of open flames regardless of the direction of noise radiation.

3. Virtually same spectral content in the low-frequencies and a nearly constant sound pressure level plateau in the mid-frequencies for various radiation angles to the flame axis.

4. Attenuation of the high-frequency noise radiated towards the far downstream positions (at low radiation angles to the flame axis) which was caused by acoustic refraction effects stemming from the sound speed gradients (which is in turn caused by the temperature non-uniformities) within the flame.

5. Combustion noise generated by the spray flame exhibited low-frequency frequency characteristic, implying that most of the acoustic energy was situated within the low-frequencies, similar to turbulent non-premixed flames.

Therefore, the hybrid DNS/APE-RF approach developed in this study is capable of accurately capturing the characteristic of radiation of combustion generated noise up to the far-field.

5.2 Suggestions for possible future research

Some possible future extensions of the present work that could provide valuable information for the design of quieter, efficient and safer gas turbine engines are

1. Regarding the study in Chapter 2, DNS was performed to investigate the effect of Reynolds number on the combustion noise of two turbulent non-premixed Hydrogen flames. In this study, both Hydrogen flames had the same fuel composition (H_2/N_2 : 50/50 volume %) but different jet exit velocities resulting in different Reynolds numbers. However, the effect of changing the fuel composition itself was not studied. DNS for investigating the effect of varying the fuel composition (but with the same jet exit velocity) on combustion generated noise of turbulent non-premixed could also be performed. The predicted combustion noise characteristics could be compared with other experimental studies to confirm the behavior caused by varying fuel composition, and the underlying mechanism that causes such behavior could be examined.

2. Similarly, regarding the study in Chapter 3, the combustion noise generated by an open turbulent spray flame with Ethanol as fuel was investigated by means of DNS employing an Eulerian-Lagrangian framework with two-way coupling. This flame is one of the experimental flames belonging to the Sydney piloted flames series. There are other Ethanol flames in the Sydney piloted flame series, with varying fuel loading (but constant carrier mass flow rate) and varying carrier mass flow rates (but fixed fuel loading). Parametric studies using the same DNS procedure, based on varying the fuel loading and carrier mass flow rates could be conducted for these flames, to assess the effect of varying said parameters (fuel loading and carrier flow rates) on combustion noise characteristics and correlations between the acoustic power of the flames and above-mentioned parameters could be derived.

3. For the study in Chapter 4, the new numerical framework of the hybrid DNS/APE-RF approach was developed for predicting and analyzing the radiation of combustion generated noise up to the far-field and applied to the turbulent spray flame

EtF3 and the turbulent non-premixed flame H3. Parametric studies as mentioned above, could be performed for different spray flames using the DNS/APE-RF approach to investigate the effect of varying liquid fuel injection rate and varying carrier velocities, on the radiation of combustion noise in the far-field. The same analyses could also be applied for the Acetone spray flames in the Sydney piloted flame series, to study the effects on combustion noise for a different fuel altogether.

In context of the DNS/APE-RF approach, this hybrid numerical framework contains only one-way coupling, i.e. data obtained from the DNS of the turbulent flame's flow-field is used as input for the CAA simulation. However, by coupling back the acoustic field from the CAA into the DNS, a two-way coupling can be implemented and the present DNS/APE-RF could be extended for studying confined flame configurations, such as combustion occurring inside gas turbine combustors. Using an appropriate model, the feedback of flame-generated acoustics onto the turbulent flame itself can be obtained, and investigations on the generation of combustion instabilities inside gas turbine combustors can be conducted.